

Marvels and Pitfalls of the Langevin Algorithm in Noisy High-dimensional Inference

Stefano Sarao Mannelli^a, Giulio Biroli^b, Chiara Cammarota^c, Florent Krzakala^b,
Pierfrancesco Urbani^a, and Lenka Zdeborová^a

^aInstitut de physique théorique, Université Paris Saclay, CNRS, CEA, 91191 Gif-sur-Yvette, France

^bLaboratoire de Physique Statistique, CNRS & Université Pierre & Marie Curie & Ecole Normale Supérieure & PSL Université, 75005 Paris, France

^cDepartment of Mathematics, King's College London, Strand London WC2R 2LS, UK

Abstract

Gradient-descent-based algorithms and their stochastic versions have widespread applications in machine learning and statistical inference. In this work we perform an analytic study of the performances of the one most commonly considered in physics, the Langevin algorithm, in the context of noisy high-dimensional inference. We employ the Langevin algorithm to sample the posterior probability measure for the spiked matrix-tensor model. The typical behaviour of this algorithm is described by a system of integro-differential equations that we call the Langevin state evolution, whose solution is compared with the one of the state evolution of approximate message passing (AMP). Our results show that, remarkably, the algorithmic threshold of the Langevin algorithm is sub-optimal with respect to the one given by AMP. This phenomenon is due to the residual glassiness present in that region of parameters. We present also a simple heuristic expression of the transition line which appears to be in agreement with the numerical results.

Contents

1 Motivation	2
2 The spiked matrix-tensor model	3
3 Bayes-optimal estimation and message-passing	4
4 Langevin Algorithm and its Analysis	5
5 Behavior of the Langevin algorithm	7
6 Glassy nature of the Langevin-hard phase	8
7 Discussion and Perspectives	10
8 Acknowledgments	11
A Definition of the spiked matrix-tensor model	14
B Approximate Message Passing, state evolution and phase diagrams	15
B.1 Approximate Message Passing and Bethe free entropy	16
B.2 Averaged free entropy and its proof	18

B.3	State evolution of AMP and its analysis	24
B.4	Phase diagrams of spiked matrix-tensor model	26
C	Langevin Algorithm and its state evolution	28
C.1	Dynamical Mean-Field Equations	29
C.2	Integro-differential equations	31
D	Numerical solution of the LSE equations	32
D.1	Fixed time-grid $(2 + p)$ -spin	32
D.2	Dynamical time-grid $(2 + p)$ -spin	33
D.3	Numerical checks on the dynamical algorithm	39
D.4	Extrapolation procedure	41
D.5	Initial conditions	43
D.6	Annealing protocol	43
E	Glassy nature of the Langevin hard phase: the replica approach	44
E.1	Computation of the complexity through the replica method	47
E.2	Breakdown of the fluctuation-dissipation theorem in the Langevin hard phase	50
F	Free-energy Hessian, BBP transition and Langevin threshold	52

1 Motivation

Algorithms based on noisy variants of gradients descent [1, 2] stand at the roots of many modern applications of data science, and are being used in a wide range of high-dimensional non-convex optimization problems. The widespread use of stochastic gradient descent in deep learning [3] is certainly one of the most prominent examples. For such algorithms, the existing theoretical analysis mostly concentrate on convex functions, convex relaxations or on regimes where spurious local minima become irrelevant. For problems with complicated landscapes where, instead, useful convex relaxations are not known and spurious local minima cannot be ruled out, the theoretical understanding of the behaviour of gradient-descent-based algorithm remains poor and represents a major avenue of research.

The goal of this paper is to contribute to such an understanding in the context of statistical learning, and to transfer ideas and techniques developed for glassy dynamics [4] to the analysis of non-convex high-dimensional inference. In statistical learning, the minimization of a cost function is not the goal per se, but rather a way to uncover an unknown structure in the data. One common way to model and analyze this situation is to generate data with a hidden structure, and to see if the structure can be recovered. This is easily set up as a *teacher-student* scenario [5, 6]: *First* a teacher generates latent variables and uses them as input of a prescribed model to generate a synthetic dataset. *Then*, the student observes the dataset and tries to infer the values of the latent variables. The analysis of this setting has been carried out rigorously in a wide range of teacher-student models for high-dimensional inference and learning tasks as diverse as planted clique [7], generalized linear models such as compressed sensing or phase retrieval [8], factorization of matrices and tensors [9, 10] or simple models of neural networks [11]. In these works, the information theoretically optimal performances —the one obtained by an ideal Bayes-optimal estimator, not limited in time and memory— have been computed.

The main question is, of course, how *practical algorithms* —operating in polynomial time with respect to the problem size— compare to these ideal performances. The last decade brought remarkable progress into our understanding of the performances achievable computationally. In particular, many algorithms based on message passing [12, 6], spectral methods [13], and semidefinite programs (SDP) [14] were analyzed. Depending on the signal-to-noise ratio, these algorithms were shown to be very efficient in many of those task. Interestingly, all these algorithm fail to reach good performance in the same region of the parameter space, and this striking observation has led to the identification of a well-defined *hard phase*. This is a regime of parameters in which the

underlying statistical problem can be information-theoretically solved, but no efficient algorithms are known, rendering the problem essentially unsolvable for large instances. This stream of ideas is currently gaining momentum and impacting research in statistics, probability, and computer science.

The performance of the noisy-gradient descent algorithms — that are certainly the one currently most used in practice — remains an entirely open question. Do they allow to reach the same performances as message passing and SDPs? Can they enter the hard phase, do they stop to be efficient at the same moment as the other approaches, or are they worse? The ambition of the present paper is to address these questions by analyzing the performance of the Langevin algorithm in the high-dimensional limit of a spiked matrix-tensor model, defined in detail in the next section.

The spiked matrix-tensor model that we consider is both generic and relevant. Similar models have played a fundamental role in statistics and random matrix theory [15, 16]. Tensor factorization is also an important topic in machine learning [17, 18, 19, 20, 21], and is widely used in data analysis [22]. At variance with the pure spiked tensor case [17], this mixed matrix-tensor model has the advantage that the algorithmic threshold appears at the same scale as the information-theoretic one, similarly to what is observed in simple models of neural networks [8, 11]. We view the spiked matrix-tensor model as a prototype for non-convex high-dimensional landscape. The key virtue of the model is its tractability.

We focus on the *Langevin algorithm* for two main reasons: Firstly it is the gradient-based algorithm that is most widely studied in physics. Secondly, at large time (possibly growing exponentially with the system size) it is known to sample the associated Boltzmann measure thus evaluating the Bayes-optimal estimator for the inference problem. We evaluate performance of the algorithm at times that are large but not growing with the system size. We explicitly compare thus obtained performance to the one of the Bayes optimal estimator and to the best known efficient algorithm so-far — the approximate message passing algorithm [12, 6]. In particular, contrary to what has been anticipated in [23, 24], but as surmised in [25], we observe that the performance of the Langevin algorithm is hampered by the many spurious metastable states still present in the AMP-easy phase. In showing that, we illustrate and discuss a number of counterintuitive features of Langevin dynamics which culminate in a paradoxical result from the point of view of Bayesian inference.

The possibility to describe analytically the behavior of the Langevin algorithm in this model is enabled by the existence of the Crisanti-Horner-Sommers-Cugliandolo-Kurchan (CHSCK) equations in spin glass theory, describing the behavior of the Langevin dynamics in the so-called spherical p -spin model [26, 27], where the method can be rigorously justified [28]. These equations were a key development in the field of statistical physics of disordered systems that lead to detailed understanding and predictions about the slow dynamics of glasses [4]. In this paper, we bring these powerful methods and ideas into the realm of statistical learning.

2 The spiked matrix-tensor model

We now detail the spiked matrix-tensor problem: a *teacher* generates a N -dimensional vector x^* by choosing each of its components independently from a normal Gaussian distribution of zero mean and unit variance. In the large N limit this is equivalent to have a flat distribution over the N -dimensional hypersphere \mathcal{S}_{N-1} defined by $|x^*|^2 = N$. The teacher then generates a symmetric matrix Y_{ij} and a symmetric order- p tensor T_{i_1, \dots, i_p} as

$$\begin{aligned} Y_{ij} &= \frac{1}{\sqrt{N}} x_i^* x_j^* + \xi_{ij} \quad \forall i < j, \\ T_{i_1 \dots i_p} &= \frac{\sqrt{(p-1)!}}{N^{(p-1)/2}} x_{i_1}^* \dots x_{i_p}^* + \xi_{i_1 \dots i_p} \quad \forall i_1 < \dots < i_p, \end{aligned} \tag{1}$$

where ξ_{ij} and ξ_{i_1, \dots, i_p} are iid Gaussian components of a symmetric random matrix and tensor of zero mean and variance Δ_2 and Δ_p , respectively; ξ_{ij} and ξ_{i_1, \dots, i_p} correspond to noises corrupting the signal of the teacher. In the limit $\Delta_2 \rightarrow 0$, and $\Delta_p \rightarrow 0$, the above model reduces to the canonical spiked Wigner model [29], and spiked tensor model [17], respectively. The goal of the student is to infer the vector x^* from the knowledge of the matrix Y , of the tensor T , of the values Δ_2 and Δ_p , and the knowledge of the spherical prior. The scaling with

N as specified in Eq. (1) is chosen in such a way that the information-theoretically best achievable error varies between perfectly reconstructed spike x^* and random guess from the flat measure on \mathcal{S}_{N-1} . Here, and in the rest of the paper we denote $x \in \mathcal{S}_{N-1}$ the N -dimensional vector, and x_i with $i = 1, \dots, N$ its components.

This model belongs to the generic direction of study of Gaussian functions on the N -dimensional sphere, known as p -spin spherical spin glass models in the physics literature, and as isotropic models in the Gaussian process literature [30, 31, 32, 33, 34]. In statistics and machine learning, these models have appeared following the studies of spiked matrix and tensor models [16, 29, 17]. Analogous matrix-tensor models, where next to a order- p tensor one observes a matrix created from the same spike are studied e.g. in [22] in the context of topic modeling, or in [17]. From the optimization-theory point of view, this model is highly non-trivial being high-dimensional and non-convex. For the purpose of the present paper this model is chosen with the hypothesis that its energy landscape presents properties that will generalize to other non-convex high-dimensional problems. The following three ingredients are key to the analysis: (a) It is in the class of models for which the Langevin algorithm can be analyzed exactly in large N limit. (b) The different phase transitions, both algorithmic and information theoretic, discussed hereafter, all happen at $\Delta_2 = \mathcal{O}(1)$, $\Delta_p = \mathcal{O}(1)$. This means that when the problem becomes algorithmically tractable it is still in the noisy regime, where the optimal mean squared error is bounded away from zero. (c) The AMP algorithm is in this model conjectured to be optimal among polynomial algorithms. It is this second and third ingredient that are not present in the pure spiked tensor model [17], making it unsuitable for our present study. We note that the Langevin algorithm was recently analyzed for the pure spiked tensor model in [20] in a regime where the noise variance is very small $\Delta \sim N^{-p/2}$, but we also note that in that model algorithms such as tensor unfolding, semidefinite programming or improved message passing schemes work better, roughly up to $\Delta \sim N^{-p/4}$ [17, 18, 35],

3 Bayes-optimal estimation and message-passing

In this section we present the performance of the Bayes-optimal estimator and of the approximate message passing algorithm. This theory is based on a straightforward adaptation of analogous results known for the pure spiked matrix model [29, 36, 9] and for the pure spiked tensor model [17, 10].

The Bayes-optimal estimator \hat{x} is defined as the one that among all estimators minimizes the mean-squared error (MSE) with the spike x^* . Starting from the posterior probability distribution

$$P(x|Y, T) = \frac{1}{Z(Y, T)} \left[\prod_{i=1}^N e^{-x_i^2/2} \right] \prod_{i < j} e^{-\frac{1}{2\Delta_2} (Y_{ij} - \frac{x_i x_j}{\sqrt{N}})^2} \prod_{i_1 < \dots < i_p} e^{-\frac{1}{2\Delta_p} \left(T_{i_1 \dots i_p} - \frac{\sqrt{(p-1)!}}{N^{(p-1)/2}} x_{i_1} \dots x_{i_p} \right)^2}, \quad (2)$$

the Bayes-optimal estimator reads

$$\hat{x}_i = \mathbb{E}_{P(x|Y, T)}(x_i). \quad (3)$$

To simplify notation, and to make contact with the energy landscape and the statistical physics notations, it is convenient to introduce the energy cost function, or Hamiltonian, as

$$\begin{aligned} \mathcal{H}(x) = \mathcal{H}_2 + \mathcal{H}_p &= -\frac{1}{\Delta_2 \sqrt{N}} \sum_{i < j} Y_{ij} x_i x_j \\ &- \frac{\sqrt{(p-1)!}}{\Delta_p N^{(p-1)/2}} \sum_{i_1 < \dots < i_p} T_{i_1 \dots i_p} x_{i_1} \dots x_{i_p} \end{aligned} \quad (4)$$

so that keeping in mind that for $N \rightarrow \infty$ the spherical constraint is satisfied $|x|^2 = N$, the posterior is written as $P(x|Y, T) = \exp[-\mathcal{H}(x)]/\tilde{Z}(Y, T)$, where \tilde{Z} is the normalizing partition function.

With the use of the replica theory and its recent proofs from [9, 37, 10] one can establish rigorously that the mean squared error achieved by the Bayes-optimal estimator is given as $\text{MMSE} = 1 - m^*$ where $m^* \in \mathbb{R}$ is the global maximizer of the so-called free entropy of the problem

$$\Phi_{\text{RS}}(m) = \frac{1}{2} \log(1 - m) + \frac{m}{2} + \frac{m^2}{4\Delta_2} + \frac{m^p}{2p\Delta_p}. \quad (5)$$

This expression is derived, and proven, in the Appendix Sec. B.2.

We now turn to the approximate message-passing (AMP) [17, 10], that is the best algorithm known so far for this problem. AMP is an iterative algorithm inspired from the work of Thouless-Anderson and Palmer in statistical physics [38]. We explicit its form in the Appendix Sec. B.1. Most remarkably performance of AMP can be evaluated by tracking its evolution with the iteration time and it is given in terms of the (possibly local) maximum of the above free entropy that is reached as a fixed point of the following iterative process

$$m^{t+1} = 1 - \frac{1}{1 + m^t/\Delta_2 + (m^t)^{p-1}/\Delta_p} \quad (6)$$

with initial condition $m^{t=0} = \epsilon$ with $0 < \epsilon \ll 1$. Eq. (6) is called the *State Evolution* of AMP and its validity is proven for closely related models in [39]. We denote the corresponding fixed point m_{AMP} and the corresponding estimation error $\text{MSE}_{\text{AMP}} = 1 - m_{\text{AMP}}$.

The phase diagram presented in Fig. 1 summarizes this theory for the spiked 2+3-spin model. It is deduced by investigating the local maxima of the scalar function (5). Notably we observe that the phase diagram in terms of Δ_2 and Δ_p splits into three phases

- **Easy** in green for $\Delta_2 < 1$ and any Δ_p : The fixed point of the state evolution (6) is the global maximizer of the free entropy (5), and $m^* = m_{\text{AMP}} > 0$.
- **Hard** in orange for $\Delta_2 > 1$ and low $\Delta_p < \Delta_p^{\text{IT}}(\Delta_2)$: The fixed point of the state evolution (6) is not the global maximizer of the free entropy (5), and $m^* > m_{\text{AMP}} = 0$.
- **Impossible** in red for $\Delta_2 > 1$ and high $\Delta_p > \Delta_p^{\text{IT}}(\Delta_2)$: The fixed point of the state evolution (6) is the global maximizer of the free entropy (5), and $m^* = m_{\text{AMP}} = 0$.

For the $2 + p$ -spin model with $p > 3$ the phase diagram is slightly richer and is presented in the Appendix Sec. D.4.

4 Langevin Algorithm and its Analysis

We now turn to the core of the paper and the analysis of the Langevin algorithm. In statistics, the most commonly used way to compute the Bayes-optimal estimator (3) is to attempt to sample the posterior distribution (2) and use several independent samples to compute the expectation in (3). In order to do that one needs to set up a stochastic dynamics on x that has a stationary measure at long times given by the posterior measure (2). The Langevin algorithm is one of the possibilities (others include notably Monte Carlo Markov chain). The common bottleneck is that the time needed to achieve stationarity can be in general exponential in the system size. In which case the algorithm is practically useless. However, this is not always the case and there are regions in parameter space where one can expect that the relaxation to the posterior measure happens on tractable timescales. Therefore it is crucial to understand where this happens and what are the associated relaxation timescales.

The Langevin algorithm on the hypersphere with Hamiltonian given by Eq. (4) reads

$$\dot{x}_i(t) = -\mu(t)x_i(t) - \frac{\partial \mathcal{H}}{\partial x_i} + \eta_i(t), \quad (7)$$

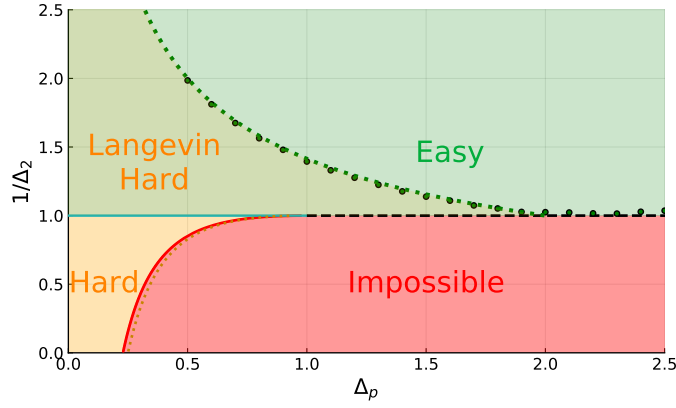


Figure 1: Phase diagram of the spiked $2 + 3$ -spin model (matrix plus order 3 tensor are observed). In the easy (green) region AMP achieves the optimal error smaller than random pick from the prior. In the impossible region (red) the optimal error is as bad as random pick from the prior, and AMP achieves it as well. In the hard region (orange) the optimal error is low, but AMP does not find an estimator better than random pick from the prior. In the case of Langevin algorithm the performance is strictly worse than that for AMP in the sense that the hard region increases up to line $1/\Delta_2^* = \max(1, \sqrt{\Delta_3/2})$, depicted in green dots. The green circles are obtained by numerical extrapolation of the Langevin state evolution equations.

where $\eta_i(t)$ is a zero mean noise term, with $\langle \eta_i(t)\eta_j(t') \rangle = 2\delta_{ij}\delta(t-t')$ where the average $\langle \cdot \rangle$ is with respect to the realizations of the noise. The Lagrange multiplier $\mu(t)$ is chosen in such a way that the dynamics remains on the hypersphere. In the large N -limit one finds $\mu(t) = 1 - 2\mathcal{H}_2(t) - p\mathcal{H}_p(t)$ where the $\mathcal{H}_2(t)$ is the 1st term from (4) evaluated at $x(t)$, and $\mathcal{H}_p(t)$ is the value of the 2nd term from (4).

The presented spiked matrix-tensor model falls into the particular class of spherical $2+p$ -spin glasses [40, 41] for which the performance of the Langevin algorithm can be tracked exactly in the large- N limit via a set of integro-partial differential equations [26, 27], beforehand dubbed CHSCK. We call this generalised version of the CHSCK equations *Langevin State Evolution* (LSE) equations in analogy with the state evolution of AMP.

In order to write the LSE equations, we defined three dynamical correlation functions

$$C_N(t, t') \equiv \frac{1}{N} \sum_{i=1}^N x_i(t)x_i(t'), \quad (8)$$

$$\bar{C}_N(t) \equiv \frac{1}{N} \sum_{i=1}^N x_i(t)x_i^*, \quad (9)$$

$$R_N(t, t') \equiv \frac{1}{N} \sum_{i=1}^N \partial x_i(t)/\partial h_i(t')|_{h_i=0}, \quad (10)$$

where h_i is a pointwise external field applied at time t' to the Hamiltonian as $\mathcal{H} + \sum_i h_i x_i$. We note that the correlation functions defined above depend on the realization of the thermal history (i.e. of the noise $\eta(t)$) and on the disorder (here the matrix Y and tensor T). However, in the large- N limit they all concentrate around their averages. We thus define $C(t, t') = \lim_{N \rightarrow \infty} \mathbb{E}_{Y, T} \langle C_N(t, t') \rangle_\eta$ and analogously for $\bar{C}(t)$ and $R(t, t')$. Standard field theoretical methods [42] or dynamical cavity method arguments [43] can then be used to obtain a closed set of integro-differential equations for the averaged dynamical correlation functions, describing the average *global* evolution of the system under the Langevin algorithm. The resulting LSE equations are (see the Appendix for a complete derivation)

$$\begin{aligned} \frac{\partial}{\partial t} C(t, t') &= 2R(t', t) - \mu(t)C(t, t') + Q'(\bar{C}(t))\bar{C}(t') + \int_0^t dt'' R(t, t'')Q''(C(t, t''))C(t', t'') + \int_0^{t'} dt'' R(t', t'')Q'(C(t, t'')), \\ \frac{\partial}{\partial t} R(t, t') &= \delta(t-t') - \mu(t)R(t, t') + \int_{t'}^t dt'' R(t, t'')Q''(C(t, t''))R(t'', t'), \\ \frac{\partial}{\partial t} \bar{C}(t) &= -\mu(t)\bar{C}(t) + Q'(\bar{C}(t)) + \int_0^t dt'' R(t, t'')\bar{C}(t'')Q''(C(t, t'')), \end{aligned} \quad (11)$$

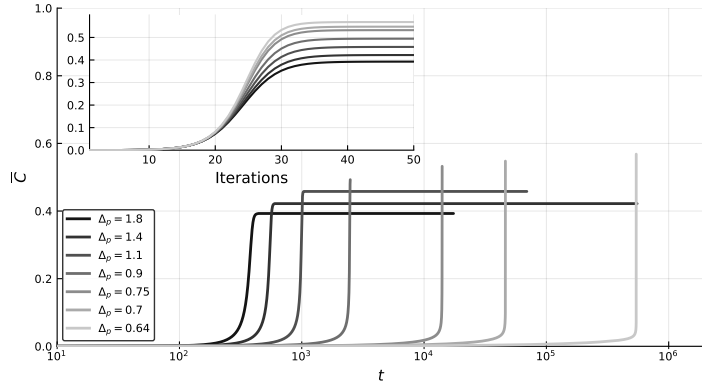


Figure 2: Evolution of the correlation with the signal $\bar{C}(t)$ starting from $\bar{C}(t = 0) = 10^{-4}$ in the Langevin algorithm at fixed noise on the matrix ($\Delta_2 = 0.7$) and different noises on the tensor (Δ_p). As we decrease Δ_p the time required to jump to the solution appears to diverge. Inset: the behavior of $\bar{C}(t)$ as a function of the iteration time for the AMP algorithm for the same values of Δ_p and the same initialization.

where we have defined $Q(x) = x^2/(2\Delta_2) + x^p/(p\Delta_p)$. The Lagrange multiplier, $\mu(t)$, is fixed by the spherical constraint, through the condition $C(t, t) = 1 \forall t$. Furthermore causality implies that $R(t, t') = 0$ if $t < t'$. Finally the Ito convention on the stochastic equation (7) gives $\forall t \lim_{t' \rightarrow t^-} R(t, t') = 1$.

5 Behavior of the Langevin algorithm

In order to assess the performances of the Langevin algorithm and compare it with AMP, we notice that the correlation function $\bar{C}(t)$ is directly related to accuracy of the algorithm. We solve the differential equations (11) numerically along the lines of [44, 45], for a detailed procedure see the Appendix Sec. C.1, codes available online at [46]. In Fig. 2 we plot the correlation with the spike $\bar{C}(t)$ as a function of the running time t for $p = 3$, fixed $\Delta_2 = 0.7$ and several values of Δ_p , we use as initial condition $\bar{C}(t = 0) = 10^{-4}$. In the inset of the plot we compare it to the same quantity obtained from the state evolution of the AMP algorithm, with the same initial condition. For the Langevin algorithm in Fig. 2 we see a pattern that is striking. One would expect that as the noise Δ_p decreases the inference problem is getting easier, the correlation with the signal is larger and is reached sooner in the iteration. This is, after all, exactly what we observe for the AMP algorithm in the inset of Fig. 2. Also for the Langevin algorithm the plateau reached for large times t becomes higher (better accuracy) as the noise Δ_p is reduced. Furthermore the height of the plateau coincides with that reached by AMP, thus testifying the algorithm reached equilibrium. However, contrary to AMP, the relaxation time for the Langevin algorithm increases dramatically when diminishing Δ_p (notice the log scale on x-axes of Fig. 2, as compared to the linear scale of the inset).

We define τ as the time it takes for the correlation to reach a value $\bar{C}_{\text{plateau}}/2$. We then plot the value of this equilibration time in the insets of Fig. 3 as a function of the noise Δ_2 having fixed Δ_p . The data are consistent with a divergence of τ at a certain finite value of Δ_2^* . We found that the divergence points are affected by the initial condition of the dynamics $\bar{C}(t = 0)$, this aspect is discussed in the Appendix Sec. D.5. In the analysis of the phase diagram we initialize the dynamics to $\bar{C}(t = 0) = 10^{-40}$ (smaller values have not led to noticeable changes in Δ_2^*). We calculate the divergence time and we fit the data with a power law $\tau(\Delta) = \left| \frac{1}{\Delta} - \frac{1}{\Delta_*} \right|^{-\gamma}$ and we obtain in the particular case of fixed $\Delta_p = 1.0$ that $\gamma = 2.24$ and $\Delta_* = 0.72$. We are not able to strictly prove that the divergence of the relaxation time truly occurs, but at least our results imply that for $\Delta_2 > \Delta_2^*$ the Langevin algorithm (7) is not a practical solver for the spiked mixed matrix-tensor problem. We will call the region $\Delta_2^* < \Delta_2 < 1$ where the AMP algorithm works optimally without problems yet Langevin algorithm does not, the *Langevin-hard region*. Δ_2^* is then plotted in Fig. 1 with green points and delimits the Langevin-hard region that extends considerably into the region where the AMP algorithm works optimally in

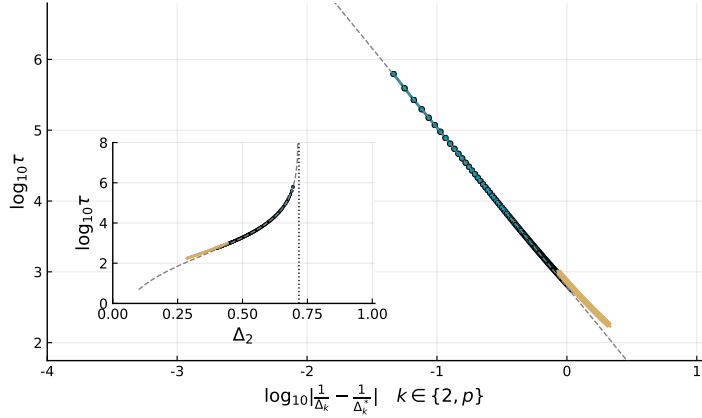


Figure 3: Extrapolation of the Langevin relaxation time. The inset presents the relaxation time for fixed $\Delta_p = 1$. The main pannel then presents a fit using a power law consistent with a divergence at $\Delta_2^* \approx 0.72$. The circles are obtained with numerical solution of LSE that uses the dynamical grid while crosses are obtained using a fixed-grid, initial condition was $\bar{C}(t=0) = 10^{-40}$ (details in the Appendix).

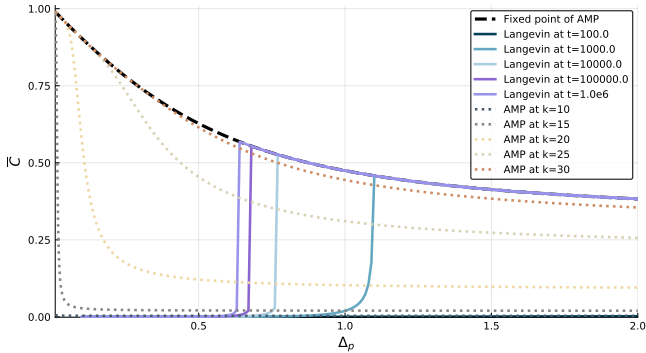


Figure 4: Correlation with the signal of AMP and Langevin at the k th iteration (at time t) for fixed $\Delta_2 = 0.7$ where both the evolutions start with initial overlap 10^{-4} .

a small number of iterations. Our main conclusion is thus that the Langevin algorithm designed to sample the posterior measure works efficiently in a considerably smaller region of parameters than the AMP as quantified in Fig. 1.

Fig. 4 presents another way to depict the observed data, the correlation $\bar{C}(t)$ reached after time t is plotted as a function of the tensor noise variance Δ_p . The results of AMP are depicted with dotted lines and, as one would expect, decrease monotonically as the noise Δ_p increases. The equilibrium value (black dashed) is reached within few dozens of iterations. On the contrary, the correlation reached by the Langevin algorithm after time t is non-monotonic and close to zero for small values of noise Δ_p signaling again a rapidly growing relaxation time when Δ_p is decreased.

6 Glassy nature of the Langevin-hard phase

The behaviour of the Langevin dynamics as presented in the last section might seem counter-intuitive at first sight, because one would expect any problem to get simpler when noise Δ_p is decreased. In the present model instead, as Δ_p is decreased, the tensor part of the cost function (4) becomes more important. This brings as a consequence that the landscape becomes rougher and causes the failure of the Langevin algorithm.

In the presence of the hard (for AMP) phase, it was recently argued in [25] that sampling-based algorithms are indeed to be expected to be worse than the approximate message passing ones. This is due to residual

glassiness that extends beyond the hard phase. We repeated the analysis of [25] in the present model (details in the Appendix Sec. E) and conclude that while this explanation provides the correct physical picture, the transition line obtained in this way does not agree quantitatively with the numerical extrapolation of the relaxation times we have obtained numerically in the previous section, at least on the timescales on which we were able to solve the LSE equations.

In order to obtain a theoretical estimate that quantitatively agrees with the observed behaviour of the LSE, we found the following argument. We first notice that the Langevin dynamics initialized at very small overlap $\bar{C}(t=0)$ remains for a long time at small values of the correlation with the signal. We assume that during this time the dynamics behaves as it would in the mixed $2+p$ -spin model without the spike. The model without the spike has been studied extensively in physics literature, precisely with the aim to understand the dynamical properties of glasses [27, 47, 4]. One of the important results of those studies is that the randomly initialized dynamics converges asymptotically to the so-called *threshold states*. Indeed in Fig. 5 this aspect can be observed in the evolution of the energy. It soon approaches a value that can be evaluated [27, 47, 4] and corresponds to threshold state energy E^{th} (horizontal lines)

$$E^{\text{th}} = -Q(1) - \left[\frac{1}{(1-q^{\text{th}})Q'(q^{\text{th}})} - \frac{1}{q^{\text{th}}} \right] Q(q^{\text{th}}). \quad (12)$$

In the above equation q^{th} represents the correlation, a.k.a. overlap, of two configurations randomly picked from the same threshold state, which can be also evaluated as the solution of

$$\frac{1}{1-q^{\text{th}}} = \sqrt{(p-1) \frac{(q^{\text{th}})^{p-2}}{\Delta_p} + \frac{1}{\Delta_2}}. \quad (13)$$

The derivation of these expressions can be found in Appendix E.1 and in Appendix F. Supported by the numerical results of Fig. 5, we make an approximation that already on the observed time-scales the algorithm converges to the threshold states ¹. The presence of the signal decides whether the algorithm develops a correlation with the signal. To understand how it occurs it should be noticed that threshold states are defined by their marginality. This means that the critical points of corresponding free energy functional that are below the threshold states are typically local minima, while those above are saddles with extensively many negative directions. The threshold states have just a few very flat directions. More precisely, the free-energy Hessian at a threshold state is statistically equivalent to a random matrix belonging to the Gaussian Orthogonal Ensemble. The corresponding eigenvalue spectrum is a shifted Wigner semi-circle having a support with a left edge touching zero [49]. In order to obtain an analytical prediction for the Langevin dynamics threshold, one has to find out how the presence of the spike destabilises the threshold states. This can be achieved by noticing that the effect of the spike is to add to the GOE matrix a rank-one perturbation in the direction of the signal. When the strength of the perturbation exceeds a certain critical value, a BBP (Baik, Ben Arous, Peché) transition takes place [50, 15]: a negative eigenvalue pops out from the Wigner semi-circle, and correspondingly a downward descent direction toward the spike emerges and makes the threshold states unstable. The derivation of the Langevin threshold and the connection with the BBP transition is worked out in detail in Appendix F.

In the following, we present a complementary argument that interestingly also makes a direct link with AMP state evolution. We again assume that Langevin dynamics approaches the threshold states. This time we use AMP to determine whether it will remain there or not. If the initial correlation is $0 < m^{t=0} \ll 1$ its evolution follows

$$m^{t+1} = (1-q^{\text{th}}) \left[\frac{(m^t)^{p-1}}{\Delta_p} + \frac{m^t}{\Delta_2} \right]. \quad (14)$$

This equation is obtained from the state evolution of the AMP algorithm where the overlap is fixed to q^{th} , as detailed in the Appendix B.3.

¹This is just an approximation because the relaxation to the threshold state is power law and only asymptotic. Therefore our assumption is expected to provide a coarse grained description of the short time dynamics. Whether it provides an exact description of what happens on long timescales remains an open problem.

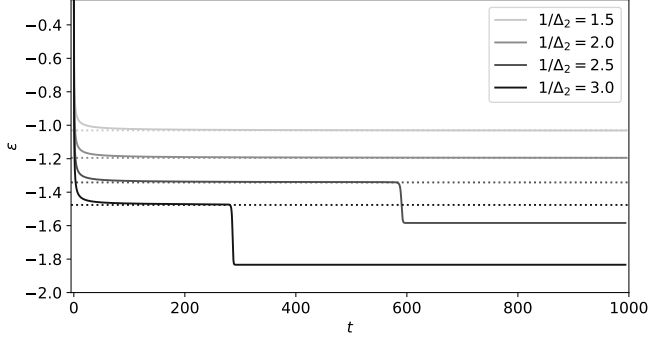


Figure 5: Dynamical evolution of the energy starting from a configuration with overlap 10^{-40} at $\Delta_p = 1.0$ and for various Δ_2 . The system first tends to the threshold energy, Eq. (12) horizontal lines, and then for sufficiently small Δ_2 finds the direction toward the signal.

The stability condition that decides whether an infinitesimal correlation will grow or decrease under (14) reads $q^{\text{th}} = 1 - \Delta_2$. Using (13), this then leads to a conjecture for the threshold of the Langevin algorithm that is the larger value of Δ_2^* between $\Delta_2^* = 1$ and the roots of

$$\Delta_p = (p-1)(\Delta_2)^2(1 - \Delta_2^*)^{p-3}. \quad (15)$$

This is the threshold depicted in Fig. 1 for $p = 3$ in green dotted line. We note a very good agreement with the data points obtained with extrapolation of the relaxation time from numerical solution of the LSE equations.

7 Discussion and Perspectives

Motivated by the general aim to shed light on behaviour and performance of noisy-gradient descent algorithms that are the currently widely used in machine learning, we investigate analytically the performance of the Langevin algorithm in the noisy high-dimensional limit of a spiked matrix-tensor model. We compare it to the performance of the approximate message passing algorithm. While both these algorithms are designed with the aim to sample the posterior measure of the model, we show that the Langevin algorithm fails to find correlation with the signal in a considerable part of the AMP-easy region. Neither of the two algorithm enters the so-called hard phase. Our analysis is based on the Langevin State Evolution equations, generalization of the dynamical theory for mean field spin glasses, that describe the evolution of the algorithm in the large size limit.

The Langevin algorithm performs worse than the AMP due to the underlying glass transition in the corresponding region of parameters. Relying on result from spin glass theory, we present a simple heuristic expression of the Langevin-threshold (15) line which appears to be in agreement with the value obtained from numerical solution of the LSE equations.

We note that so far, in our study of the spiked matrix-tensor model with Langevin dynamics, we only accessed the cost function (4) and its derivatives. We did not allow ourselves to split the cost function in the tensor-related \mathcal{H}_p and the matrix-related \mathcal{H}_2 parts. If we did then there is a simple way to overcome the Langevin-hard regime by first considering only the matrix measurements and then slowly turning on the tensor, in a similar way as temperature is tuned in simulated annealing. We study this procedure in the Appendix D.6. It is interesting to underline that this finding is somewhat paradoxical from the point of view of Bayesian inference. In the setting of this paper we know perfectly the model that generated the data and all its parameters, yet we see that for the Langevin algorithm it is computationally advantageous to mismatch the parameters and perform the annealing in the tensor part in order to reach faster convergence to equilibrium. This is particularly striking given that for AMP it has been proven in [7] that mismatching the parameters can never improve the performance.

We stress that the above annealing procedure is a particularity of the present model and will not generalize to a broad range of inference problems, because it is not clear in general how to split the cost function into simple to optimize yet informative part and the rest. A formidably interesting direction for future work consists instead in investigating whether the performance of the Langevin algorithm can be improved in a manner that only accesses the cost function or its derivatives.

While we studied here the spiked matrix-tensor model, we expect that our findings, based on the existence of an underlying glass transition, will hold more universally. We expect them to apply to other local sampling dynamics, e.g. to Monte Carlo Markov chains, and to a broader range of models, e.g. simple models of neural networks. An interesting extension of this work would be to investigate algorithms closer to stochastic gradient descent and models closer to current neural network architectures.

8 Acknowledgments

We thank G. Folena, A. Crisanti and G. Ben Arous for precious discussions. We thank K. Miyazaki for sharing his code for the numerical integration of CHSCK equations. We acknowledge funding from the ERC under the European Union’s Horizon 2020 Research and Innovation Programme Grant Agreement 714608-SMiLe; from the French National Research Agency (ANR) grant PAIL; from "Investissements d’Avenir" LabEx PALM (ANR-10-LABX-0039-PALM) (SaMURai and StatPhysDisSys); and from the Simons Foundation (#454935, Giulio Biroli).

References

- [1] L. Bottou, in *Proceedings of COMPSTAT’2010* (Springer, 2010) pp. 177–186.
- [2] M. Welling and Y. W. Teh, in *Proceedings of the 28th International Conference on Machine Learning (ICML-11)* (2011) pp. 681–688.
- [3] Y. LeCun, Y. Bengio, and G. Hinton, *Nature* **521**, 436 (2015).
- [4] J.-P. Bouchaud, L. F. Cugliandolo, J. Kurchan, and M. Mézard, Spin glasses and random fields , 161 (1998).
- [5] H. S. Seung, H. Sompolinsky, and N. Tishby, *Phys. Rev. A* **45**, 6056 (1992).
- [6] L. Zdeborová and F. Krzakala, *Advances in Physics* **65**, 453 (2016), <http://dx.doi.org/10.1080/00018732.2016.1211393> .
- [7] Y. Deshpande and A. Montanari, *Foundations of Computational Mathematics* **15**, 1069 (2015).
- [8] J. Barbier, F. Krzakala, N. Macris, L. Miolane, and L. Zdeborová, *Proceedings of the National Academy of Sciences* **116**, 5451 (2019).
- [9] J. Barbier, M. Dia, N. Macris, F. Krzakala, T. Lesieur, and L. Zdeborová, in *Advances in Neural Information Processing Systems 29* (2016) p. 424–432.
- [10] T. Lesieur, L. Miolane, M. Lelarge, F. Krzakala, and L. Zdeborová, in *Information Theory (ISIT), 2017 IEEE International Symposium on* (IEEE, 2017) pp. 511–515.
- [11] B. Aubin, A. Maillard, J. Barbier, F. Krzakala, N. Macris, and L. Zdeborová, in *Advances in Neural Information Processing Systems* (2018).
- [12] D. L. Donoho, A. Maleki, and A. Montanari, *Proceedings of the National Academy of Sciences* **106**, 18914 (2009).

[13] F. Krzakala, C. Moore, E. Mossel, J. Neeman, A. Sly, L. Zdeborová, and P. Zhang, *Proceedings of the National Academy of Science* **110**, 20935 (2013), [arXiv:1306.5550](https://arxiv.org/abs/1306.5550) .

[14] S. B. Hopkins and D. Steurer, arXiv preprint arXiv:1710.00264 (2017).

[15] J. Baik, G. Ben Arous, S. Péché, *et al.*, *The Annals of Probability* **33**, 1643 (2005).

[16] I. M. Johnstone and A. Y. Lu, *Journal of the American Statistical Association* **104**, 682 (2009).

[17] E. Richard and A. Montanari, in *Advances in Neural Information Processing Systems* (2014) pp. 2897–2905.

[18] S. B. Hopkins, J. Shi, and D. Steurer, in *Conference on Learning Theory* (2015) pp. 956–1006.

[19] R. Ge and T. Ma, in *Advances in Neural Information Processing Systems* (2017) pp. 3653–3663.

[20] G. Ben Arous, R. Gheissari, and A. Jagannath, arXiv preprint arXiv:1808.00921 (2018).

[21] V. Ros, G. Ben Arous, G. Biroli, and C. Cammarota, *Physical Review X* **9**, 011003 (2019).

[22] A. Anandkumar, R. Ge, D. Hsu, S. M. Kakade, and M. Telgarsky, *The Journal of Machine Learning Research* **15**, 2773 (2014).

[23] F. Krzakala and L. Zdeborová, *Physical review letters* **102**, 238701 (2009).

[24] A. Decelle, F. Krzakala, C. Moore, and L. Zdeborová, *Physical Review E* **84**, 066106 (2011).

[25] F. Antenucci, S. Franz, P. Urbani, and L. Zdeborová, *Physical Review X* **9**, 011020 (2019).

[26] A. Crisanti, H. Horner, and H.-J. Sommers, *Zeitschrift für Physik B Condensed Matter* **92**, 257 (1993).

[27] L. F. Cugliandolo and J. Kurchan, *Physical Review Letters* **71**, 173 (1993).

[28] G. Ben Arous, A. Dembo, and A. Guionnet, *Probability theory and related fields* **136**, 619 (2006).

[29] Y. Deshpande and A. Montanari, in *Information Theory (ISIT), 2014 IEEE International Symposium on* (IEEE, 2014) pp. 2197–2201.

[30] D. J. Gross and M. Mézard, *Nuclear Physics B* **240**, 431 (1984).

[31] Y. V. Fyodorov, *Physical review letters* **92**, 240601 (2004).

[32] A. Auffinger, G. Ben Arous, and J. Černý, *Communications on Pure and Applied Mathematics* **66**, 165 (2013).

[33] L. Sagun, V. U. Guney, G. Ben Arous, and Y. LeCun, arXiv preprint arXiv:1412.6615 (2014).

[34] G. Ben Arous, S. Mei, A. Montanari, and M. Nica, arXiv preprint arXiv:1711.05424 (2017).

[35] A. S. Wein, A. E. Alaoui, and C. Moore, arXiv preprint arXiv:1904.03858 (2019).

[36] T. Lesieur, F. Krzakala, and L. Zdeborová, *Journal of Statistical Mechanics: Theory and Experiment* **2017**, 073403 (2017).

[37] M. Lelarge and L. Miolane, *Probability Theory and Related Fields* , 1 (2016).

[38] D. J. Thouless, P. W. Anderson, and R. G. Palmer, *Philosophical Magazine* **35**, 593–601 (1977).

[39] A. Javanmard and A. Montanari, *Information and Inference: A Journal of the IMA* **2**, 115 (2013).

[40] A. Crisanti and L. Leuzzi, *Physical review letters* **93**, 217203 (2004).

[41] A. Crisanti and L. Leuzzi, Physical Review B **73**, 014412 (2006).

[42] P. C. Martin, E. Siggia, and H. Rose, Physical Review A **8**, 423 (1973).

[43] M. Mézard, G. Parisi, and M.-A. Virasoro, *Spin glass theory and beyond*. (World Scientific Publishing, 1987).

[44] B. Kim and A. Latz, EPL (Europhysics Letters) **53**, 660 (2001).

[45] L. Berthier, G. Biroli, J.-P. Bouchaud, W. Kob, K. Miyazaki, and D. Reichman, The Journal of chemical physics **126**, 184503 (2007).

[46] S. Sarao Mannelli, G. Biroli, C. Cammarota, F. Krzakala, P. Urbani, and L. Zdeborová, “Langevin state evolution integrators,” (2018), available at: https://github.com/sphinxteam/spiked_matrix-tensor.

[47] L. Cugliandolo and J. Kurchan, Philosophical Magazine B **71**, 501 (1995).

[48] This is just an approximation because the relaxation to the threshold state is power law and only asymptotic. Therefore our assumption is expected to provide a coarse grained description of the short time dynamics. Whether it provides an exact description of what happens on long timescales remains an open problem.

[49] A. Bray and M. Moore, Journal of Physics C: Solid State Physics **12**, L441 (1979).

[50] S. F. Edwards and R. C. Jones, Journal of Physics A: Mathematical and General **9**, 1595 (1976).

[51] A. Crisanti and L. Leuzzi, Nuclear Physics B **870**, 176 (2013).

[52] M. Mézard and A. Montanari, *Information, physics, and computation* (Oxford University Press, 2009).

[53] S. Boucheron, G. Lugosi, and O. Bousquet, in *Advanced Lectures on Machine Learning* (Springer, 2004) pp. 208–240.

[54] S. B. Korada and N. Macris, Journal of Statistical Physics **136**, 205 (2009).

[55] F. Krzakala, J. Xu, and L. Zdeborová, in *2016 IEEE Information Theory Workshop (ITW)* (2016) pp. 71–75.

[56] M. Aizenman, R. Sims, and S. L. Starr, Physical Review B **68**, 214403 (2003).

[57] J. Barbier and N. Macris, Probability Theory and Related Fields, 1 (2018).

[58] A. E. Alaoui and F. Krzakala, in *2018 IEEE International Symposium on Information Theory (ISIT)* (2018) pp. 1874–1878.

[59] J.-C. Mourrat, arXiv preprint arXiv:1811.01432 (2018).

[60] D. Guo, S. Shamai, and S. Verdú, IEEE Transactions on Information Theory **51**, 1261 (2005).

[61] H.-O. Georgii, *Gibbs measures and phase transitions*, Vol. 9 (Walter de Gruyter, 2011).

[62] N. Macris, IEEE Transactions on Information Theory **53**, 664 (2007).

[63] A. Montanari, European Transactions on Telecommunications **19**, 385 (2008).

[64] A. Coja-Oghlan, F. Krzakala, W. Perkins, and L. Zdeborova, in *Proceedings of the 49th Annual ACM SIGACT Symposium on Theory of Computing (STOC)* (2017) pp. 146–157.

[65] H. Nishimori, *Statistical physics of spin glasses and information processing: an introduction*, Vol. 111 (Clarendon Press, 2001).

[66] F. Guerra and F. L. Toninelli, Communications in Mathematical Physics **230**, 71 (2002).

[67] F. Ricci-Tersenghi, G. Semerjian, and L. Zdeborová, “Typology of phase transitions in bayesian inference problems,” Preprint:arXiv:1806.11013.

[68] L. F. Cugliandolo, in *Slow Relaxations and nonequilibrium dynamics in condensed matter* (Springer, 2003) pp. 367–521.

[69] T. Castellani and A. Cavagna, Journal of Statistical Mechanics: Theory and Experiment **2005**, P05012 (2005).

[70] E. Agoritsas, G. Biroli, P. Urbani, and F. Zamponi, Journal of Physics A: Mathematical and Theoretical **51**, 085002 (2018).

[71] L. Berthier, G. Biroli, J.-P. Bouchaud, W. Kob, K. Miyazaki, and D. R. Reichman, The Journal of chemical physics **126**, 184504 (2007).

[72] R. Monasson, Physical review letters **75**, 2847 (1995).

[73] F. Zamponi, arXiv preprint arXiv:1008.4844 (2010).

[74] A. Crisanti and H.-J. Sommers, Zeitschrift für Physik B Condensed Matter **87**, 341 (1992).

[75] L. Cugliandolo and J. Kurchan, Journal of Physics A: Mathematical and General **27**, 5749 (1994).

[76] L. F. Cugliandolo and J. Kurchan, Progress of Theoretical Physics Supplement **126**, 407 (1997).

[77] D. Thouless, P. Anderson, and R. Palmer, Phil. Mag **35**, 593.

[78] W.-K. Chen and D. Panchenko, Communications in Mathematical Physics **362**, 219 (2018).

[79] A. Crisanti and H.-J. Sommers, Journal de Physique I **5**, 805 (1995).

A Definition of the spiked matrix-tensor model

We consider a teacher-student setting in which the teacher constructs a matrix and a tensor from a randomly sampled signal and the student is asked to recover the signal from the observation of the matrix and tensor provided by the teacher [6].

The signal, x^* is an N -dimensional vector whose entries are real i.i.d. random variables sampled from the normal distribution (i.e. the prior is $P_X \sim \mathcal{N}(0, 1)$). The teacher generates from the signal a symmetric matrix and a symmetric tensor of order p . Those two objects are then transmitted through two noisy channels with variances Δ_2 and Δ_p , so that at the end one has two noisy observations given by

$$Y_{ij} = \frac{x_i^* x_j^*}{\sqrt{N}} + \xi_{ij}, \quad (16)$$

$$T_{i_1, \dots, i_p} = \frac{\sqrt{(p-1)!}}{N^{(p-1)/2}} x_{i_1}^* \dots x_{i_p}^* + \xi_{i_1, \dots, i_p}, \quad (17)$$

where, for $i < j$ and $i_1 < \dots < i_p$, ξ_{ij} and ξ_{i_1, \dots, i_p} are i.i.d. random variables distributed according to $\xi_{ij} \sim \mathcal{N}(0, \Delta_2)$ and $\xi_{i_1, \dots, i_p} \sim \mathcal{N}(0, \Delta_p)$. The ξ_{ij} and ξ_{i_1, \dots, i_p} are symmetric random matrix and tensor, respectively. Given Y_{ij} and T_{i_1, \dots, i_p} the inference task is to reconstruct the signal x^* .

In order to solve this problem we consider the Bayesian approach. This starts from the assumption that both the matrix and tensor have been produced from a process of the same kind of the one described by Eq. (16-17). Furthermore we assume to know the statistical properties of the channel, namely the two variances Δ_2 and Δ_p , and the prior on x . Given this, the posterior probability distribution over the signal is obtained through the Bayes formula

$$P(X|Y, T) = \frac{P(Y, T|X)P(X)}{P(Y, T)}, \quad (18)$$

where

$$\begin{aligned} P(Y, T|X) &= \prod_{i < j} P_Y \left(Y_{ij} \middle| \frac{x_i x_j}{\sqrt{N}} \right) \prod_{i_1 < \dots < i_p} P_T \left(T_{i_1 \dots i_p} \middle| \frac{\sqrt{(p-1)!}}{N^{(p-1)/2}} x_{i_1} \dots x_{i_p} \right) = \\ &\propto \prod_{i < j} e^{-\frac{1}{2\Delta_2} \left(Y_{ij} - \frac{x_i x_j}{\sqrt{N}} \right)^2} \prod_{i_1 < \dots < i_p} e^{-\frac{1}{2\Delta_p} \left(T_{i_1 \dots i_p} - \frac{\sqrt{(p-1)!}}{N^{(p-1)/2}} x_{i_1} \dots x_{i_p} \right)^2}. \end{aligned} \quad (19)$$

Therefore we have

$$P(X|Y, T) = \frac{1}{Z(Y, T)} \prod_i e^{-\frac{1}{2} x_i^2} \prod_{i < j} e^{-\frac{1}{2\Delta_2} \left(Y_{ij} - \frac{x_i x_j}{\sqrt{N}} \right)^2} \prod_{i_1 < \dots < i_p} e^{-\frac{1}{2\Delta_p} \left(T_{i_1 \dots i_p} - \frac{\sqrt{(p-1)!}}{N^{(p-1)/2}} x_{i_1} \dots x_{i_p} \right)^2}, \quad (20)$$

where $Z(Y, T)$ is a normalization constant.

Plugging Eqs. (16-17) into Eq. (20) allows to rewrite the posterior measure in the form of a *Boltzmann distribution* of the mixed $2 + p$ -spin Hamiltonian [40, 41, 51]

$$\begin{aligned} \mathcal{H} &= -\frac{1}{\Delta_2 \sqrt{N}} \sum_{i < j} \xi_{ij} x_i x_j - \frac{\sqrt{(p-1)!}}{\Delta_p N^{\frac{p-1}{2}}} \sum_{i_1 < \dots < i_p} \xi_{i_1 \dots i_p} x_{i_1} \dots x_{i_p} - \frac{N}{2\Delta_2} \left(\frac{1}{N} \sum_i x_i x_i^* \right)^2 + \\ &\quad - \frac{N}{p\Delta_p} \left(\frac{1}{N} \sum_i x_i x_i^* \right)^p - \frac{1}{2} \sum_{i=1}^N x_i^2 + \text{const.} \end{aligned} \quad (21)$$

so that

$$P(X|Y, T) = \frac{1}{\tilde{Z}(Y, T)} e^{-\mathcal{H}}. \quad (22)$$

In the following we will refer to $\tilde{Z}(Y, T)$ as the *partition function*. We note here that in the large N limit, using a Gaussian prior on the variables x_i is equivalent to consider a flat measure over the N -dimensional hypersphere $\sum_{i=1}^N x_i^2 = N$. This choice will be used when we will describe the Langevin algorithm and in this case the last term in the Hamiltonian will become an irrelevant constant.

B Approximate Message Passing, state evolution and phase diagrams

Approximate Message Passing (AMP) is a powerful iterative algorithms to compute the local *magnetizations* $\langle x_i \rangle$ given the observed matrix and tensor. It is rooted in the cavity method of statistical physics of disordered systems [38, 43] and it has been recently developed in the context of statistical inference [12], where in the Bayes optimal case it has been conjectured to be optimal among all local iterative algorithms. Among the properties that make AMP extremely useful is the fact that its performances can be analyzed in the thermodynamic limit. Indeed in such limit, its dynamical evolution is described by the so called State Evolution (SE) equations [12]. In this section we derive the AMP equations and their SE description for the spiked matrix-tensor model and solve them to obtain the phase diagram of the model as a function of the variances Δ_2 and Δ_p of the two noisy channels.

B.1 Approximate Message Passing and Bethe free entropy

AMP can be obtained as a relaxed Gaussian closure of the Belief Propagation (BP) algorithm. The derivation that we present follows the same lines of [10, 36]. The posterior probability can be represented as a factor graph where all the variables are represented by circles and are linked to squares representing the interactions [52].

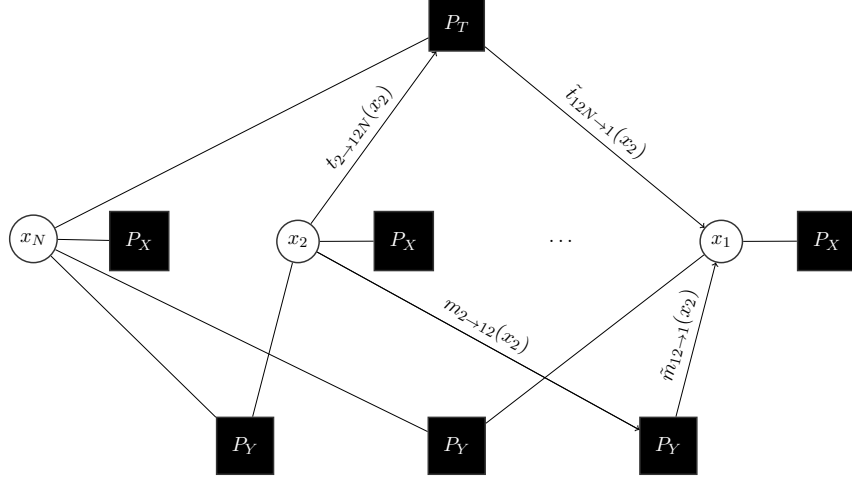


Figure 6: The factor graph representation of the posterior measure of the matrix-tensor factorization model. The variable nodes represented with white circles are the components of the signal while black squares are factor nodes that denote interactions between the variable nodes that appear in the interaction terms of the Boltzmann distribution in Eqs. (21-22). There are three types of factor nodes: P_X is the prior that depends on a single variable, P_Y that is the probability of observing a matrix element Y_{ij} given the values of the variables x_i and x_j , and finally P_T that is the probability of observing a tensor element T_{i_1, \dots, i_p} . The posterior, apart from the normalization factor, is simply given by the product of all the factor nodes.

This representation is very convenient to write down the BP equations. In the BP algorithm we iteratively update until convergence a set of variables, which are beliefs of the (cavity) magnetization of the nodes. The intuitive underlying reasoning behind how BP works is the following. Given the current state of the variable nodes, take a factor node and exclude one node among its neighbors. The remaining neighbors through the factor node express a belief on the state of the excluded node. This belief is mathematically described by a probability distribution called *message*, $\tilde{m}_{ij \rightarrow i}^t(x_i)$ and $\tilde{t}_{i_2 \dots i_p \rightarrow i}^t(x_i)$ depending on which factor node is selected. At the same time, another belief on the state of the excluded node is given by the rest of the network but the factor node previously taken into account, $m_{i \rightarrow ij}(x_i)$ and $t_{i \rightarrow i_2 \dots i_p}(x_i)$ respectively. All these *messages* travel in the factor graph carrying partial information on the real magnetization of the single nodes, and they are iterated until convergence. The iterative scheme is described by the following equations

$$\tilde{m}_{ij \rightarrow i}^t(x_i) \propto \int dx_j m_{j \rightarrow ij}^t(x_j) P_Y \left(Y_{ij} \middle| \frac{x_i x_j}{\sqrt{N}} \right), \quad (23)$$

$$m_{i \rightarrow ij}^{t+1}(x_i) \propto P_X(x_i) \prod_{l \neq j} \tilde{m}_{il \rightarrow i}^t(x_i) \prod_{i_2 < \dots < i_p} \tilde{t}_{i_2 \dots i_p \rightarrow i}^t(x_i), \quad (24)$$

$$\tilde{t}_{i_2 \dots i_p \rightarrow i}^t(x_i) \propto \int \prod_{l=2 \dots p} \left(dx_l t_{il \rightarrow i_2 \dots i_p}^t(x_l) \right) P_T \left(T_{i_2 \dots i_p} \middle| \frac{\sqrt{(p-1)!}}{N^{(p-1)/2}} x_i x_{i_2} \dots x_{i_p} \right), \quad (25)$$

$$t_{i \rightarrow i_2 \dots i_p}^{t+1}(x_i) \propto P_X(x_i) \prod_l \tilde{m}_{il \rightarrow i}^t(x_i) \prod_{k_2 < \dots < k_p \neq i_2 \dots i_p} \tilde{t}_{ik_2 \dots k_p \rightarrow i}^t(x_i) \quad (26)$$

and we have omitted the normalization constants that guarantee that the messages are probability distributions. When the messages have converged to a fixed point, the estimation of the local magnetizations can be obtained

through the computation of the real marginal probability distribution of the variables given by

$$\mu_i(x_i) = \int \left[\prod_{j(\neq i)} dx_j \right] P(X|Y, T) = P_X(x_i) \prod_l \tilde{m}_{il \rightarrow i}^t(x_i) \prod_{i_2 < \dots < i_p} \tilde{t}_{ii_2 \dots i_p \rightarrow i}^t(x_i). \quad (27)$$

We note that the computational cost to produce an iteration of BP scales as $O(N^p)$. Furthermore Eqs. (23-26) are iterative equations for continuous functions and therefore are extremely hard to solve when dealing with continuous variables. The advantage of AMP is to reduce drastically the computational complexity of the algorithm by closing the equations on a Gaussian ansatz for the messages. This is justified in the present context since the factor graph is fully connected and therefore each iteration step of the algorithm involves sums of a large number of independent random variables that give rise to Gaussian distributions. Gaussian random variables are characterized by their mean and covariance that are readily obtained for $N \gg 1$ expanding the factor nodes for small $\omega_{ij} = x_i x_j / \sqrt{N}$ and $\omega_{i_1 \dots i_p} = \sqrt{(p-1)!} x_1 \dots x_p / N^{\frac{p-1}{2}}$.

Once the BP equations are relaxed on Gaussian messages, the final step to obtain the AMP algorithm is the so-called TAPification procedure [36, 38], which exploits the fact that the procedure of removing one node or one factor produces only a weak perturbation to the real marginals and therefore can be described in terms of the real marginals of the variable nodes themselves. By applying this scheme we obtain the AMP equations, which are described by a set of auxiliary variables $A^{(k)}$ and $B_i^{(k)}$ and by the mean $\langle x_i \rangle$ and variance $\sigma_i = \langle x_i^2 \rangle$ of the marginals of variable nodes. The AMP iterative equations are

$$B_i^{(2),t} = \frac{1}{\Delta_2 \sqrt{N}} \sum_k Y_{ki} \hat{x}_k^t - \frac{1}{\Delta_2} \left(\frac{1}{N} \sum_k \sigma_k^t \right) \hat{x}_i^{t-1}; \quad (28)$$

$$A^{(2),t} = \frac{1}{\Delta_2 N} \sum_k \left(\hat{x}_k^t \right)^2; \quad (29)$$

$$B_i^{(p),t} = \frac{\sqrt{(p-1)!}}{\Delta_p N^{(p-1)/2}} \sum_{k_2 \dots k_p} T_{ik_2 \dots k_p} \left(\hat{x}_{k_2}^t \dots \hat{x}_{k_p}^t \right) - \frac{p-1}{\Delta_p} \left[\left(\frac{1}{N} \sum_k \sigma_k^t \right) \left[\frac{1}{N} \sum_k \hat{x}_k^t \hat{x}_k^{t-1} \right]^{p-2} \right] \hat{x}_i^{t-1}; \quad (30)$$

$$A^{(p),t} = \frac{1}{\Delta_p} \left[\frac{1}{N} \sum_k \left(\hat{x}_k^t \right)^2 \right]^{p-1}; \quad (31)$$

$$\hat{x}_i^{t+1} = f(A^{(2)} + A^{(p)}, B_i^{(2)} + B_i^{(p)}); \quad (32)$$

$$\sigma_i^{t+1} = \frac{\partial}{\partial B} f(A, B) \Big|_{A=A^{(2)}+A^{(p)}, B=B_i^{(2)}+B_i^{(p)}}, \quad (33)$$

$$f(A, B) \equiv \int dx \frac{1}{Z(A, B)} x P_X(x) e^{Bx - \frac{1}{2} Ax^2} = \frac{B}{1+A}. \quad (34)$$

It can be shown that these equations can be obtained as saddle point equations from the so called Bethe free entropy defined as $\Phi_{\text{Bethe}} = \log Z^{\text{Bethe}}(Y, T)/N$ where Z^{Bethe} is the Bethe approximation to the partition function which is defined as the normalization of the posterior measure. The expression of the Bethe free entropy per variable can be computed in a standard way (see [52]) and it is given by

$$\Phi_{\text{Bethe}} = \frac{1}{N} \left(\sum_i \log Z_i + \sum_{i \leq j} \log Z_{ij} + \sum_{i_1 \leq \dots \leq i_p} \log Z_{i_1 \dots i_p} - \sum_{i(ij)} \log Z_{i,ij} - \sum_{i(ii_2 \dots i_p)} \log Z_{i(ii_2 \dots i_p)} \right), \quad (35)$$

where

$$Z_i = \int dx_i P_X(x_i) \prod_j \tilde{m}_{ij \rightarrow i}(x_i) \prod_{(i_2 \dots i_p)} \tilde{t}_{ii_2 \dots i_p \rightarrow i}(x_i),$$

$$\begin{aligned}
Z_{ij} &= \int \prod_{j(\neq i)} [dx_j m_{j \rightarrow ij}(x_j)] \prod_{i < j} e^{-\frac{1}{2\Delta_2} \left(Y_{ij} - \frac{x_i x_j}{\sqrt{N}} \right)^2}, \\
Z_{i_1 \dots i_p} &= \int \prod_{l=1}^p [dx_{i_l} t_{i_l \rightarrow i_1 \dots i_p}(x_{i_l})] \prod_{i_1 < \dots < i_p} e^{-\frac{1}{2\Delta_p} \left(T_{i_1 \dots i_p} - \frac{\sqrt{(p-1)!}}{N^{(p-1)/2}} x_{i_1} \dots x_{i_p} \right)^2}, \\
Z_{i(ij)} &= \int dx_i m_{i \rightarrow ij}(x) \tilde{m}_{ij \rightarrow i}(x_i), \\
Z_{i(ii_2 \dots i_p)} &= \int dx_i t_{i \rightarrow ii_2 \dots i_p}(x) \tilde{t}_{ii_2 \dots i_p \rightarrow i}(x_i)
\end{aligned}$$

are a set of normalization factors. Using the Gaussian approximation for the messages and employing the same TAPyfication procedure used to get the AMP equations we obtain the Bethe free entropy density as

$$\begin{aligned}
\Phi_{\text{Bethe}} &= \frac{1}{N} \sum_i \log \mathcal{Z}(A^{(p)} + A^{(2)}, B_i^{(p)} + B_i^{(2)}) + \frac{p-1}{p} \frac{1}{N} \sum_i \left[-B_i^{(p)} \hat{x}_i + A_i^{(p)} \frac{\hat{x}_i^2 + \sigma_i}{2} \right] + \\
&+ \frac{p-1}{2p\Delta_p} \left(\frac{\sum_i \hat{x}_i^2}{N} \right)^{p-1} \left(\frac{\sum_i \sigma_i}{N} \right) + \frac{1}{2N} \sum_i \left[-B_i^{(2)} \hat{x}_i + A_i^{(2)} \frac{\hat{x}_i^2 + \sigma_i}{2} \right] + \frac{1}{4\Delta_2} \left(\frac{\sum_i \hat{x}_i^2}{N} \right) \left(\frac{\sum_i \sigma_i}{N} \right),
\end{aligned} \tag{36}$$

where we used the variables defined in eqs. (28-31) for sake of compactness and $\mathcal{Z}(A, B)$ is defined as

$$\mathcal{Z}(A, B) = \int dx P_X(x) e^{Bx - \frac{Ax^2}{2}} = \frac{1}{\sqrt{A+1}} e^{\frac{B^2}{2(A+1)}}. \tag{37}$$

B.2 Averaged free entropy and its proof

Eq. (36) represents the Bethe free entropy for a single realization of the factor nodes in the large size limit. Here we wish to discuss the actual, exact, value of this free entropy, that is:

$$f_N(Y, T) = \frac{\log Z(Y, T)}{N}$$

This is a random variable, since it depends a priori on the planted signal and the noise in the tensor and matrices. However one expects that, since free entropy is an intensive quantity, we expect from the statistical physics intuition that it should be self averaging and concentrate around its mean value in the large N limit [43]. In fact, this is easily proven. First, since the spherical model has a rotational symmetry, one may assume the planted assignment could be any vector on the hyper-sphere, and we might as well suppose it is the uniform one $x_i^* = 1 \forall i$: the true source of fluctuation comes from the noise Y and T . These can be controlled by noticing that the free entropy is a Lipschitz function of the Gaussian random variable Y and T . Indeed:

$$\partial_{Y_{ij}} f_N(Y, T) = \frac{1}{\Delta_2 N \sqrt{N}} \langle x_i x_j \rangle$$

so that the free energy f_N is Lipschitz with respect to Y with constant

$$L = \frac{1}{\Delta_2 N \sqrt{N}} \sqrt{\sum_{i < j} \langle x_i x_j \rangle^2} \leq \frac{1}{\Delta_2 N \sqrt{N}} \sqrt{\frac{1}{2} \sum_{i,j} \langle x_i x_j \rangle^2} = \frac{1}{\Delta_2 N \sqrt{N}} \sqrt{\frac{1}{2} \sum_{i,j} \langle x_i \tilde{x}_i x_j \tilde{x}_j \rangle}$$

where \tilde{x} represent a copy (or replica) of the system. In this case

$$L \leq \frac{1}{\Delta_2 N \sqrt{N}} \sqrt{N^2 \langle \left(\frac{\sum_i x_i \tilde{x}_i}{N} \right)^2 \rangle} = \frac{\sqrt{\langle q^2 \rangle}}{\Delta_2 \sqrt{N}}$$

where q is the overlap between the two replica x and \tilde{x} , that is bounded by one on the sphere, so $L \leq \frac{1}{\Delta_2 \sqrt{N}}$. Therefore, by Gaussian concentration of Lipschitz functions (the Tsirelson-Ibragimov-Sudakov inequality [53]), we have for some constant K :

$$\Pr [|f_N - \mathbb{E}_Y f_N| \geq t] \leq 2e^{-Nt^2/K} \quad (38)$$

and it particular any fluctuation larger than $O(1/\sqrt{N})$ is (exponentially) rare. A similar computaton shows that f_N also concentrates with respect to the tensor T . This shows that in the large size limit, we can consider the averaged free entropy:

$$\mathcal{F}_N \equiv \frac{1}{N} \mathbb{E} [\log Z_N]$$

With our (non-rigorous) statistical physics tools, this can be obtained by averaging Eq. (36) over the disorder, see for instance [36], and this yields an expression for the free energy called the replica symmetric (RS) formula:

$$\Phi_{\text{RS}} = \lim_{N \rightarrow \infty} \mathbb{E}_{Y,T} \frac{\log Z(Y, T)}{N}. \quad (39)$$

We now state precisely the form of Φ_{RS} and prove the validity of Eq. (39). The RS free entropy for any prior distribution P_X reads as

$$\Phi_{\text{RS}} \equiv \max_m \tilde{\Phi}_{\text{RS}}(m) \quad \text{where}$$

$$\tilde{\Phi}_{\text{RS}}(m) = \mathbb{E}_{W,x^*} \left[\log \left[\mathcal{Z} \left(\frac{m}{\Delta_2} + \frac{m^{p-1}}{\Delta_p}, \left(\frac{m}{\Delta_2} + \frac{m^{p-1}}{\Delta_p} \right) x^* + \sqrt{\frac{m}{\Delta_2} + \frac{m^{p-1}}{\Delta_p}} W \right) \right] \right] - \frac{1}{4\Delta_2} m^2 - \frac{p-1}{2p\Delta_p} m^p, \quad (40)$$

where W is a Gaussian random variable of zero mean and unit variance and x^* is a random variables taken from the prior P_X . We remind that the function $\mathcal{Z}(A, B)$ is defined via Eq. (37).

For Gaussian prior P_X , which is the one of interest here, we obtain

$$\tilde{\Phi}_{\text{RS}}(m) = -\frac{1}{2} \log \left(\frac{m}{\Delta_2} + \frac{m^{p-1}}{\Delta_p} + 1 \right) + \frac{1}{2} \left(\frac{m}{\Delta_2} + \frac{m^{p-1}}{\Delta_p} \right) - \frac{1}{4\Delta_2} m^2 - \frac{p-1}{2p\Delta_p} m^p. \quad (41)$$

The expression given in the main text is slightly different but can be obtained as follow. First notice that the extremization condition for $\tilde{\Phi}_{\text{RS}}(m)$ reads

$$m = 1 - \frac{1}{1 + \frac{m}{\Delta_2} + \frac{m^{p-1}}{\Delta_p}} \quad (42)$$

and by plugging this expression in Eq. (41) we recover the more compact expression $\Phi_{\text{RS}}(m)$ showed in the main text:

$$\Phi_{\text{RS}}(m) = \frac{1}{2} \log (1 - m) + \frac{m}{2} + \frac{m^2}{4\Delta_2} + \frac{m^p}{2p\Delta_p}. \quad (43)$$

The two expressions $\Phi_{\text{RS}}(m)$ and $\tilde{\Phi}_{\text{RS}}(m)$ are thus equal for each value of m that satisfy Eq. (42). The parameter m can be interpreted as the average correlation between the true and the estimated signal

$$m = \frac{1}{N} \sum_{i=1}^N x_i^* \hat{x}_i. \quad (44)$$

The average minimal mean squared error (MMSE) can be obtained from the maximizer m of the average Bethe free entropy as

$$\text{MMSE} \equiv \frac{1}{N} \sum_{i=1}^N \overline{(x_i^* - \hat{x}_i)^2} = 1 - m^*, \quad \text{where } m^* = \text{argmax} \tilde{\Phi}_{\text{RS}}(m). \quad (45)$$

where the overbar stands for the average over the signal x^* and the noise of the two Gaussian channels.

The validity of Eq. (40) can be proven rigorously for every prior having a bounded second moment. The proof we shall present is a straightforward generalization of the one presented in [10] for the pure tensor case, and in [37] for the matrix case, and it is based on two main ingredients. The first one is the Guerra interpolation method applied on the Nishimori line [54, 55, 37], in which we construct an interpolating Hamiltonian that depends on a parameter $t \in [0; 1]$ that is used to move from the original Hamiltonian of Eq. (21), to the one corresponding to a scalar denoising problem whose free entropy is given by the first term in Eq. (40). The second ingredient is the Aizenman-Sims-Starr method [56] which is the mathematical version of the cavity method (note that other techniques could also be employed to obtain the same results, see [9, 57, 58, 59]). The theorem we want to prove is:

Theorem 1 (Replica-Symmetric formula for the free energy). *Let P_X be a probability distribution over \mathbb{R} , with finite second moment Σ_X . Then, for all $\Delta_2 > 0$ and $\Delta_p > 0$*

$$\mathcal{F}_N \equiv \frac{1}{N} \mathbb{E} [\log Z_N] \xrightarrow[N \rightarrow \infty]{\longrightarrow} \sup_{m \geq 0} \tilde{\Phi}_{\text{RS}}(m) \equiv \Phi_{\text{RS}}(\Delta_2, \Delta_p). \quad (46)$$

For almost every $\Delta_2 > 0$ and $\Delta_p > 0$, $\tilde{\Phi}_{\text{RS}}$ admits a unique maximizer m over $\mathbb{R}_+ \times \mathbb{R}_+$ and

$$\begin{aligned} \text{T-MMSE}_N &\xrightarrow[N \rightarrow \infty]{\longrightarrow} \Sigma_X^p - (m^*)^p, \\ \text{M-MMSE}_N &\xrightarrow[N \rightarrow \infty]{\longrightarrow} \Sigma_X^2 - (m^*)^2. \end{aligned}$$

Here, we have defined the tensor-MMSE T-MMSE _{N} by the error in reconstructing the tensor:

$$\text{T-MMSE}_N(\Delta_2, \Delta_p) = \inf_{\hat{\theta}} \left\{ \frac{p!}{N^p} \sum_{i_1 < \dots < i_p} \left(x_{i_1}^0 \dots x_{i_p}^0 - \hat{\theta}(Y)_{i_1 \dots i_p} \right)^2 \right\},$$

and the matrix-MMSE M-MMSE _{N} by the error in reconstructing the matrix:

$$\text{M-MMSE}_N(\Delta_2, \Delta_p) = \inf_{\hat{\theta}} \left\{ \frac{2}{N^2} \sum_{i < j} \left(x_i^0 x_j^0 - \hat{\theta}(Y)_{i,j} \right)^2 \right\},$$

where in both cases the infimum is taken over all measurable functions $\hat{\theta}$ of the observations Y .

The result concerning the MMSE is a simple application of the I-MMSE theorem [60], that relates the derivative of the free energy with respect to the noise variances and the MMSE. The details of the arguments are the same than in the matrix ($p = 2$) case ([37], corollary 17) and the tensor one ([10], theorem 2). Indeed, as discussed in [37, 10], these M-MMSE and T-MMSE results implies the vector MMSE result of Eq. (45) when p is odd, and thus in particular for the $p = 3$ case discussed in the main text.

Sketch of proof In this section we give a detailed sketch of the proof theorem 1. Following the techniques used in many recent works [54, 55, 9, 37, 10, 57, 58, 8], we shall make few technical remarks:

- We will consider only priors with bounded support, $\text{supp}(P_X) = S \subset [-K; K]$. This allows to switch integrals and derivatives without worries. This condition can then be relaxed to unbounded distributions with bounded second moment using the same techniques as the ones that we are going to present, and the proof is therefore valid in this case. This is detailed for instance in [37] sec. 6.2.2.
- Another key ingredient is the introduction of a small perturbation in the model that takes the form of a small amount of side information. This kind of techniques are frequently used in statistical physics, where a small “magnetic field” forces the Gibbs measure to be in a single pure state [61]. It has also

been used in the context of coding theory [62] for the same reason. In the context of Bayesian inference, we follow the generic scheme proposed by Montanari in [63] (see also [64]) and add a small additional source of information that allows the system to be in a single pure state so that the overlap concentrates on a single value. This source depends on Bernoulli random variables $L_i \stackrel{\text{i.i.d.}}{\sim} \text{Bern}(\epsilon)$, $i \in [N]$; if $L_i = 1$, the channel, call it A , transmits the correct information. We can then consider the posterior of this new problem, $P(X|A, Y, T)$, and focus on the associated free energy density $F_{N,\epsilon}$ defined as the expected value of the average of the logarithm of normalization constant divided by the number of spins. Then we can immediately prove that for all $N \geq 1$ and $\epsilon, \epsilon' \in [0; 1]$ it follows: $|F_{N,\epsilon} - F_{N,\epsilon'}| \leq \left(\frac{K^{2p}}{\Delta_p} + \frac{K^4}{\Delta_2} \right) |\epsilon - \epsilon'|$. This allows (see for instance [10]) to obtain the concentration of the posterior distribution around the replica parameter ($q = \frac{1}{N} \langle x^{(1)} \cdot x^{(2)} \rangle$)

$$\mathbb{E} \left\langle \left(\frac{x^{(1)} \cdot x^{(2)}}{N} - q \right)^2 \right\rangle \xrightarrow{N \rightarrow \infty} 0; \quad (47)$$

$$\mathbb{E} \left\langle \left(\frac{x^* \cdot x}{N} - q \right)^2 \right\rangle \xrightarrow{N \rightarrow \infty} 0, \quad (48)$$

where $x, x^{(1)}, x^{(2)}$ are sampled from the posterior distribution and the averages $\langle \cdot \rangle$ and $\mathbb{E}[\cdot]$ are respectively the average over the posterior measure and the remaining random variables.

- Finally, a fundamental property of inference problems which is a direct consequence of the Bayes theorem, and of the fact that we are in the Bayes optimal setting where we know the statistical properties of the signal, namely the prior, and the statistical properties of the channels, namely Δ_2 and Δ_p , is the so-called Nishimori symmetry [65, 6]: Let (X, Y) be a couple of random variables on a polish space. Let $k \geq 1$ and let $X^{(1)}, \dots, X^{(k)}$ be k i.i.d. samples (given Y) from the distribution $P(X = \cdot | Y)$, independently of every other random variables. Let us denote $\langle \cdot \rangle$ the expectation with respect to $P(X = \cdot | Y)$ and \mathbb{E} the expectation with respect to (X, Y) . Then, for all continuous bounded function f

$$\mathbb{E} \langle f(Y, X^{(1)}, \dots, X^{(k)}) \rangle = \mathbb{E} \langle f(Y, X^{(1)}, \dots, X^{(k-1)}, X) \rangle.$$

While the consequences of this identity are important, the proof is rather simple: It is equivalent to sample the couple (X, Y) according to its joint distribution or to sample first Y according to its marginal distribution and then to sample X conditionally to Y from its conditional distribution $P(X = \cdot | Y)$. Thus the $(k+1)$ -tuple $(Y, X^{(1)}, \dots, X^{(k)})$ is equal in law to $(Y, X^{(1)}, \dots, X^{(k-1)}, X)$.

The proof of Theorem 1 is obtained by using the Guerra interpolation technique to prove a lower bound for the free entropy and then by applying the Aizenman-Sims-Star scheme to get a matching upper bound.

Lower bound: Guerra interpolation We now move to the core of the proof. The first part combines the Guerra interpolation method [66] developed for matrices in [55] and tensors in [10].

Consider the interpolating Hamiltonian depending of $t \in [0, 1]$

$$\begin{aligned} \mathcal{H}_{N,t} = & - \sum_{i < j} \left[\frac{\sqrt{t}}{\Delta_2 \sqrt{N}} Y_{ij} x_i x_j + \frac{t}{2\Delta_2 N} (x_i x_j)^2 \right] + \\ & - \sum_{i_1 < \dots < i_p} \left[\frac{\sqrt{t(p-1)!}}{\Delta_p N^{\frac{p-1}{2}}} T_{i_1 \dots i_p} x_{i_1} \dots x_{i_p} + \frac{t(p-1)!}{2\Delta_p N^{p-1}} (x_{i_1} \dots x_{i_p})^2 \right] + \\ & - \sum_j \left[\sqrt{1-t} \sqrt{\frac{m^{p-1}}{\Delta_p} + \frac{m}{\Delta_2}} W_j x_j + (1-t) \left(\frac{m^{p-1}}{\Delta_p} + \frac{m}{\Delta_2} \right) x_j^* x_j + \frac{1-t}{2} \left(\frac{m^{p-1}}{\Delta_p} + \frac{m}{\Delta_2} \right) x_j^2 \right], \end{aligned} \quad (49)$$

where we have for $t = 1$ the regular Hamiltonian and for $t = 0$ the first term of Eq. (40) where W_j are i.i.d. canonical Gaussian variables. More importantly, for all $t \in [0, 1]$ we can show that the Hamiltonian above can be seen as the one emerging for an appropriate inference problem, so that the Nishimori property is kept valid for generic $t \in [0, 1]$ [55].

Given the interpolating Hamiltonian we can write the corresponding Gibbs measure,

$$P(x|W, Y, T) = \frac{1}{Z_{N,t}} P_X(x) e^{H_{N,t}(x)}, \quad (50)$$

and the interpolating free entropy

$$\psi_N(t) \doteq \frac{1}{N} \mathbb{E} [\log Z_{N,t}], \quad (51)$$

whose boundaries are $\psi_N(1) = \frac{1}{N} \mathcal{F}_N$ (our target) and $\psi_N(0) = \frac{1}{N} \tilde{\Phi}_{\text{RS}} + \frac{1}{4\Delta_2} m^2 + \frac{p-1}{2p\Delta_p} m^p$. We then use the fundamental theorem of calculus to write

$$\mathcal{F}_N = \psi_N(1) = \psi_N(0) + \underbrace{\frac{1}{N} \mathbb{E} \int_0^1 \left(-\frac{\partial \log Z_{N,t}}{\partial t} \right) dt}_{\doteq \mathcal{R}}. \quad (52)$$

We work with the second term and use Stein's lemma which, given a well behaving function g , provides the useful relation for a canonical Gaussian variable Z : $\mathbb{E}_Z[Zg(Z)] = \mathbb{E}_Z[g'(Z)]$. This yields

$$\begin{aligned} \mathcal{R} &= -\mathbb{E} \int_0^1 \left[\frac{1}{Z_{N,t}} \int dx^N \frac{\partial \mathcal{H}_{N,t}(x)}{\partial t} P_X(x) e^{\mathcal{H}_{N,t}(x)} \right] dt = -\mathbb{E} \int_0^1 \left\langle \frac{\partial \mathcal{H}_{N,t}(x)}{\partial t} \right\rangle dt \\ &= -\mathbb{E} \int_0^1 \left\langle \sum_{i < j} \frac{1}{\Delta_2 N} (x_i^* x_i x_j^* x_j) + \sum_{i_1 < \dots < i_p} \frac{(p-1)!}{\Delta_2 N^{p-1}} (x_{i_1}^* x_{i_1} \dots x_{i_p}^* x_{i_p}) - \sum_i \left(\frac{m}{2\Delta_2} + \frac{m^{p-1}}{2\Delta_p} \right) x_i^* x_i \right\rangle dt \\ &= \mathbb{E} \int_0^1 \left[\frac{1}{4\Delta_2} \left\langle \left(\frac{x \cdot x^*}{N} \right)^2 - 2m \left(\frac{x \cdot x^*}{N} \right) \right\rangle + \frac{1}{2p\Delta_p} \left\langle \left(\frac{x \cdot x^*}{N} \right)^p - pm^{p-1} \left(\frac{x \cdot x^*}{N} \right) \right\rangle \right] dt. \end{aligned}$$

where we have used the Nishimori property to replace terms such as $\langle x \rangle^2$ by $\langle x x^* \rangle$. At this point, we can write

$$\begin{aligned} \mathcal{R} &= \mathbb{E} \int_0^1 \left[\frac{1}{4\Delta_2} \left\langle \left(\frac{x \cdot x^*}{N} \right)^2 - 2m \left(\frac{x \cdot x^*}{N} \right) \right\rangle \right] dt + \mathbb{E} \int_0^1 \left[\frac{1}{2p\Delta_p} \left\langle \left(\frac{x \cdot x^*}{N} \right)^p - pm^{p-1} \left(\frac{x \cdot x^*}{N} \right) \right\rangle \right] dt \\ &= -\frac{m^2}{4\Delta_2} + \frac{1}{4\Delta_2} \mathbb{E} \int_0^1 \frac{1}{4\Delta_2} \left\langle \left(\frac{x \cdot x^*}{N} - m \right)^2 \right\rangle dt + \frac{1}{2p\Delta_p} \mathbb{E} \int_0^1 \left\langle \left(\frac{x \cdot x^*}{N} \right)^p - pm^{p-1} \left(\frac{x \cdot x^*}{N} \right) \right\rangle dt. \end{aligned} \quad (53)$$

The first integral is clearly positive. The second one, however, seems harder to estimate. We may, however, use a simple convexity argument on the function $f(x) = x^k$. Indeed observe that $\forall a, b \geq 0$ and $p \geq 1$: $a^p - pb^{p-1}a \geq (1-p)b^p$. We would like to use this property but there is the subtlety that we need $x \cdot x^*$ to be non-negative. To bypass this problem we can add again a small perturbation that forces $x \cdot x^*$ to concentrate around a non-negative value, without affecting the “interpolating free entropy” $\psi_N(t)$ in the $N \rightarrow \infty$ limit. This is, again, the argument used in [10] and originally in [54]. In this way we can write

$$\begin{aligned} \mathcal{R} &\geq -\frac{m^2}{4\Delta_2} + \mathbb{E} \int_0^1 \left[\frac{1}{4\Delta_2} \left\langle \left(\frac{x \cdot x^*}{N} \right)^2 - 2m \left(\frac{x \cdot x^*}{N} \right) \right\rangle \right] dt + \frac{(1-p)m^p}{4\Delta_2} \\ &\geq -\frac{m^2}{4\Delta_2} - \frac{(p-1)m^p}{4\Delta_2}. \end{aligned} \quad (54)$$

This concludes the proof and yields the lower bound:

$$\mathcal{F}_N \geq \psi_N(0) - \frac{1}{4\Delta_2}m^2 - \frac{p-1}{2p\Delta_p}m^p = \frac{1}{N}\tilde{\Phi}_{\text{RS}}(m), \quad (55)$$

so that for all $m \geq 0$

$$\liminf_{N \rightarrow \infty} \mathcal{F}_N = \liminf_{N \rightarrow \infty} \psi_N(1) = \liminf_{N \rightarrow \infty} \left[\psi_N(0) + \int_0^1 \psi'_N(t) dt \right] \geq \tilde{\Phi}_{\text{RS}}(m).$$

Upper bound: Aizenman-Sims-Starr scheme. The matching upper bound is obtained using the Aizenman-Sims-Starr scheme [56]. This is a particularly effective tool that has been already used for these problems, see for example [37, 64, 10]. The method goes as follows. Consider the original system with N variables, \mathcal{H}_N and add a new variable x_0 so that we get an Hamiltonian \mathcal{H}_{N+1} . Define the Gibbs measures of the two systems, the first with N variables and the second with $N+1$ variables, and consider the two relative free entropies. Call $A_N = \mathbb{E}[\log \mathcal{Z}_{N+1}] - \mathbb{E}[\log \mathcal{Z}_N]$ their difference. First, we notice that we have $\limsup_N \mathcal{F}_N \leq \limsup_N A_N$ because

$$\mathcal{F}_N = \mathbb{E} \frac{1}{N} \log Z_N = \frac{1}{N} \mathbb{E} \log \left(\frac{Z_N}{Z_{N-1}} \frac{Z_{N-1}}{Z_{N-2}} \cdots \frac{Z_1}{Z_0} \right) = \frac{1}{N} \sum_i A_i \leq \sup_i A_i.$$

Moreover, we can separate the contribution of the additional variable in the Hamiltonian \mathcal{H}_{N+1} so that $\mathcal{H}_{N+1} = \tilde{\mathcal{H}}_N + x_0 z(x) + x_0^2 s(x)$, with $x = (x_1, \dots, x_N)$, and

$$\begin{aligned} z(x) &= \frac{1}{\sqrt{\Delta_2(N+1)}} \sum_{i=1}^N Z_{0i} x_i + \frac{\sqrt{(p-1)!}}{\sqrt{\Delta_p(N+1)^{(p-1)/2}}} \sum_{1 \leq i_1 < \dots < i_{p-1} \leq N} Z_{0i_1 \dots i_{p-1}} x_{i_1} \dots x_{i_{p-1}} + \\ &+ \frac{1}{\Delta_2(N+1)} \sum_{i=1}^N x_0^* x_i^* x_i + \frac{(p-1)!}{\Delta_p(N+1)^{p-1}} \sum_{1 \leq i_1 < \dots < i_{p-1} \leq N} x_0^* x_{i_1}^* x_{i_1} \dots x_{i_{p-1}}^* x_{i_{p-1}} \\ s(x) &= -\frac{1}{2\Delta_2(N+1)} \sum_{i=1}^N x_i^2 - \frac{(p-1)!}{2\Delta_p(N+1)^{p-1}} \sum_{1 \leq i_1 < \dots < i_{p-1} \leq N} (x_{i_1} \dots x_{i_{p-1}})^2 \end{aligned}$$

and \mathcal{H}_{N+1} is the same expression as Eq. (21) where the N in the denominators are replaced by $N+1$. We rewrite also $\mathcal{H}_N(x)$ as a perturbation of $\tilde{\mathcal{H}}_N$: $\mathcal{H}_N(x) = \tilde{\mathcal{H}}_N(x) + y(x) + O(1)$ with

$$\begin{aligned} y(x) &= \frac{1}{\sqrt{\Delta_2 N}} \sum_{i < j} V_{ij} x_i x_j + \sqrt{p-1} \frac{\sqrt{(p-1)!}}{\sqrt{\Delta_p} N^{p/2}} \sum_{i_1 < \dots < i_p} V_{i_1 \dots i_p} x_{i_1} \dots x_{i_p} + \\ &+ \frac{1}{N^2} \sum_{i < j} \left[x_i^* x_i x_j^* x_j - \frac{1}{2} (x_i x_j)^2 \right] + (p-1)! \frac{p-1}{N^p} \sum_{i_1 < \dots < i_p} \left[x_{i_1}^* x_{i_1} \dots x_{i_p}^* x_{i_p} - \frac{1}{2} (x_{i_1} \dots x_{i_p})^2 \right], \end{aligned}$$

where the Z s and the V s are standard Gaussian random variables.

Finally we can observe the partition functions Z_N can be interpreted as ensemble averages with respect to $\tilde{\mathcal{H}}_N$. Thus $A_N = \mathbb{E} \log \left\langle \int P_X(x_0) e^{x_0 z(x) + x_0^2 s(x)} dx_0 \right\rangle_{\tilde{\mathcal{H}}_N} - \mathbb{E} \log \left\langle e^{y(x)} \right\rangle_{\tilde{\mathcal{H}}_N}$. Now, using the Nishimori property and the concentration of the overlap around a non-negative value —that we denote $m(Y, T)$ since it depends explicitly on the disorder— it yields (see [37], see section 4.3 for details) (40) in the thermodynamic limit, with $m(Y, T)$ instead of m . From this, we can now obtain the upper bound that concludes the proof:

$$\limsup_N \mathcal{F}_N \leq \limsup_N A_N \leq \limsup_N \mathbb{E}_{Y, T} \tilde{\Phi}_{\text{RS}}[m(Y, T)] \leq \limsup_N \sup_m \Phi_{\text{RS}}(m) \leq \tilde{\Phi}_{\text{RS}}. \quad (56)$$

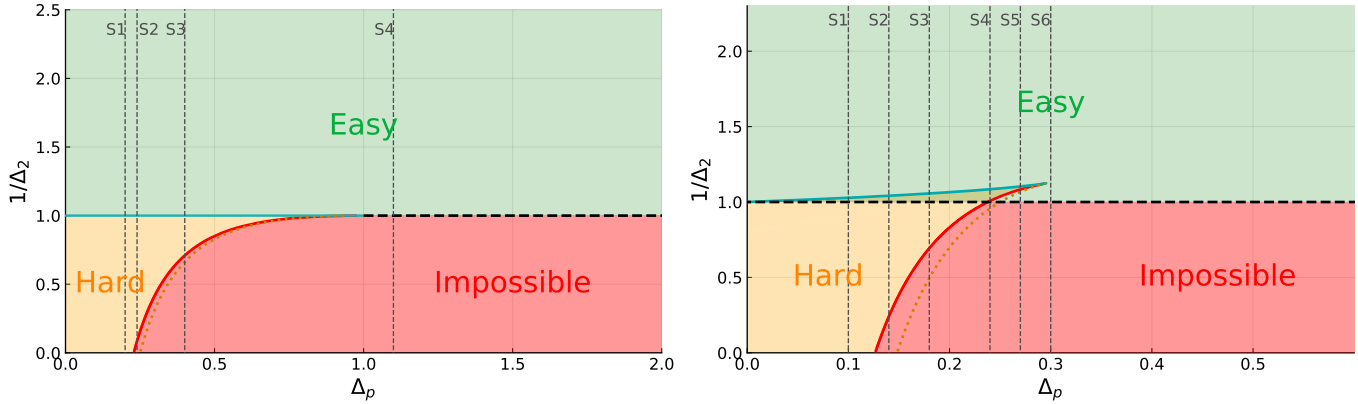


Figure 7: *On the left:* Phase diagram of the spiked matrix-tensor model for $p = 3$. The phase diagram identifies four regions: easy (green), impossible (red), and hard (orange). The lines correspond to different phase transitions namely the stability threshold (dashed black), the information theoretic threshold (solid red), the algorithmic threshold (solid cyan), and the dynamical threshold (dotted orange). The vertical cuts represent the section along which the magnetization is plotted in Fig. 9. *On the right:* Phase diagram of the spiked matrix-tensor model for $p = 4$. The main difference with respect to case $p = 3$, is that the algorithmic spinodal (solid cyan) is strictly above the stability threshold (dashed black). The hybrid-hard phase appears between these two lines (combined green and orange color). The vertical cuts represent the section along which the magnetization is plotted in Fig. 10.

B.3 State evolution of AMP and its analysis

The dynamical evolution of the AMP algorithm in the large N limit is described by the so-called State Evolution (SE) equations. The derivation of these equations can be straightforwardly done using the same techniques as developed in [36]. They can be written in terms of two dynamical order parameters namely $m^t = \sum_i \hat{x}_i^t x_i^*/N$, which encodes for the alignment of the current estimation \hat{x}_i^t of the components of the signal with the signal itself at time t and $q^t = \sum_i \hat{x}_i^t \hat{x}_i^t/N$. Keeping the spherical constraint in mind we obtain the following SE equations

$$\frac{m^{t+1}}{1 - q^{t+1}} = \frac{m^t}{\Delta_2} + \frac{(m^t)^{p-1}}{\Delta_p} , \quad (57)$$

$$\frac{q^{t+1}}{(1 - q^{t+1})^2} = \left[\frac{m^t}{\Delta_2} + \frac{(m^t)^{p-1}}{\Delta_p} \right]^2 + \left[\frac{q^t}{\Delta_2} + \frac{(q^t)^{p-1}}{\Delta_p} \right] . \quad (58)$$

Note that eq. (57) at fixed values of q describes the evolution of the parameter m , this is why we use in the main text to derive the Langevin threshold eq. (15). Finally, using the Nishimori symmetry it can be shown that $m^t = q^t$ at all times, see e.g. [6], and therefore the evolution of the algorithm is characterized by a single order parameter m^t whose dynamical evolution is given by

$$m^{t+1} = 1 - \frac{1}{1 + \frac{m^t}{\Delta_2} + \frac{(m^t)^{p-1}}{\Delta_p}} . \quad (59)$$

Note that AMP satisfies the Nishimori property at all times while this condition is violated on the run by the Langevin dynamics. In that case the Nishimori symmetry is recovered only when equilibrium is reached and therefore it is violated when the Langevin algorithm gets trapped in the glass phase, see below. If we initialize the configuration of the estimator \hat{x} at random, the initial value of m will be equal to zero on average. However, finite size fluctuations produce by chance a small bias towards the signal and therefore we consider the initialization to be $m^{t=0} = \epsilon$ being ϵ an arbitrarily small positive number. We will call m_{AMP} the fixed

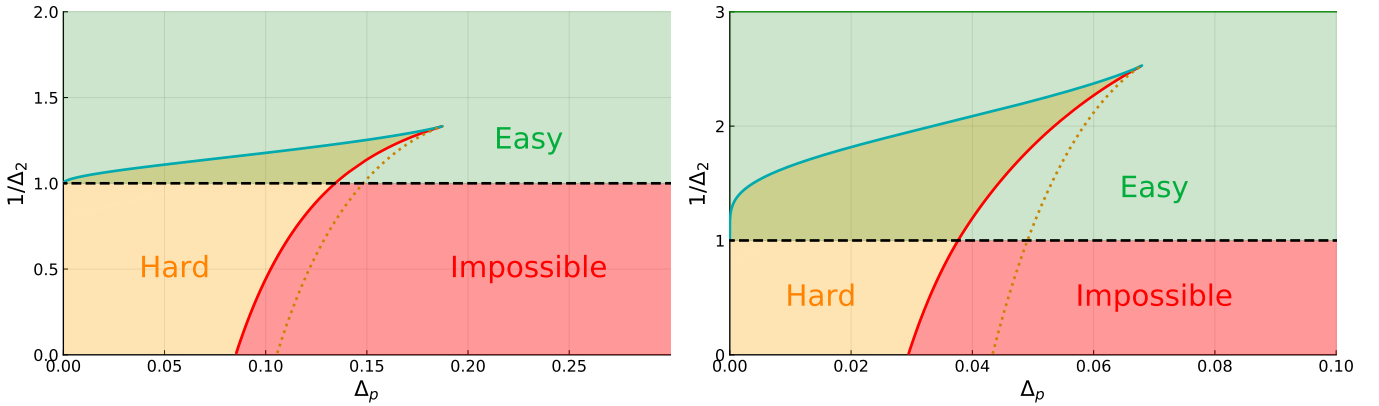


Figure 8: *On the left*: Phase diagram of the spiked matrix-tensor model for $p = 5$. *On the right*: Phase diagram of the spiked matrix-tensor model for $p = 10$. In both cases we observe qualitatively the same scenario found in the right panel of Fig. 7.

point of Eq. (59) reached from this infinitesimal initialization. The mean-square-error (MSE) reached by AMP after convergence is then given by $\text{MSE}_{\text{AMP}} = 1 - m_{\text{AMP}}$.

We underline that Eq. (59) can be proven rigorously following [39, 17]. Finally we note that the fixed point of the SE satisfies the very same Eq. (42) that gives the replica free entropy. In the rest of this section we will study the fixed points of Eq. (59). This will allow too determine the phase diagram of the spiked matrix-tensor model.

We start by observing that $m = 0$ is a fixed point of Eq. (59). However, in order to understand whether it is a possible attractor of the AMP dynamics we need to understand its local stability. This can be obtained perturbatively by expanding Eq. (59) around $m = 0$

$$m^{t+1} = \frac{m^t}{\Delta_2} + \left(\frac{m^t}{\Delta_2} \right)^2 - \frac{(m^t)^{p-1}}{\Delta_p} + O \left((m^t)^3 \right). \quad (60)$$

It is clear that the non-informative fixed point $m = 0$ is stable as long as $\Delta_2 > 1$. We will call $\Delta_2 = 1$ the *stability threshold*.

When $p = 3$ the SE equations are particularly simple and the fixed points are written explicitly as

$$m_0 = 0; \quad m_{\pm} = \frac{1}{2} \left[1 - \frac{\Delta_3}{\Delta_2} \pm \sqrt{\left(1 + \frac{\Delta_3}{\Delta_2} \right)^2 - 4\Delta_3} \right]. \quad (61)$$

In the regime where $\Delta_2 > 1$, m_0 and m_+ are stable while m_- in unstable. When Δ_2 becomes smaller than one, m_+ becomes the only non-negative stable solution and therefore $\Delta_2 = 1$ is also known as the *algorithmic spinodal* since it corresponds to the point where the AMP algorithm converges to the informative fixed point. The informative solution m_+ exists as long as $\Delta_2 \leq \Delta_2^{\text{dyn}}$, where we have defined the *dynamical spinodal* by

$$\Delta_2^{\text{dyn}} = \frac{\Delta_3}{2\sqrt{\Delta_3 - 1}}. \quad (62)$$

For a generic p we cannot determine the values of the informative fixed points explicitly but we can easily study Eq. (59) numerically to get the full phase diagram.

Furthermore we can obtain the spinodal transition lines as follows. The key observation is that the two spinodals are critical points of the equation $\Delta_p(m; \Delta_2)$ where Δ_2 is fixed, or analogously $\Delta_2(m; \Delta_p)$ where Δ_p is fixed (to have a pictorial representation of the idea you can see Fig. 10). We call $x = m/\Delta_2 + m^{p-1}/\Delta_p$, and

$f_{\text{SE}}(x) \equiv 1 - \frac{1}{1+x}$, then

$$\Delta_p \equiv \Delta_p(x; \Delta_2) = \frac{(f_{\text{SE}}(x))^{p-1}}{x - \frac{f_{\text{SE}}(x)}{\Delta_2}}. \quad (63)$$

Then the stationary points are implicitly defined by

$$0 = \frac{d \log \Delta_p}{dm} = \frac{\partial \log \Delta_p}{\partial x} (1+x)^2 \propto (p-1) \frac{f'_{\text{SE}}(x)}{f_{\text{SE}}(x)} - \frac{1 - \frac{f'_{\text{SE}}(x)}{\Delta_2}}{x - \frac{f'_{\text{SE}}(x)}{\Delta_2}} = \frac{\frac{2-p}{\Delta_2} + (1+x)(p-x-2)}{x(1+x) \left[x + 1 - \frac{1}{\Delta_p} \right]},$$

giving

$$x_{\pm}(\Delta_2) = \frac{1}{2} \left[p - 3 \pm \sqrt{(p-1)^2 - \frac{4}{\Delta_2}(p-2)} \right]. \quad (64)$$

Finally $\Delta_p(x_{\pm}(\Delta_2); \Delta_2)$ describes the two spinodals. We can also derive the tri-critical point, when the two spinodals meet, which is given by the zero discriminant condition on (64)

$$\left(\Delta_p^{\text{tri}}; 1/\Delta_2^{\text{tri}} \right) = \left(\frac{4(p-2) \left(\frac{p-3}{p-1} \right)^{p-1}}{(p-3)^2}; \frac{(p-1)^2}{4(p-2)} \right). \quad (65)$$

B.4 Phase diagrams of spiked matrix-tensor model

In this section we present the phase diagrams for the spiked matrix-tensor model as a function of the two noise levels Δ_2 and Δ_p and for several values of p . These phase diagrams are plotted in Figs. 7 and 8. Generically we can have four regions:

- **Easy phase** (green), where the MSE obtained through AMP coincides with the MMSE which is better than random sampling of the prior.
- **Impossible phase** (red), where the MMSE and MSE of AMP coincide and are equal to 1 (meaning that $m^* = m_{\text{AMP}} = 0$).
- **Hard phase** (orange), where the MMSE is smaller than the MSE obtained from AMP and $m^* > m_{\text{AMP}} \geq 0$.
- **Hybrid-hard phase** [67] (mix of green and orange), is a part of the hard phase where the AMP performance is strictly better than random sampling from the prior, but still the MSE obtained this way does not match the MMSE, i.e. $m^* > m_{\text{AMP}} > 0$. The hybrid-hard phase can be found for $p \geq 4$.

All these phases are separated by the following transition lines:

- The **stability threshold** (dashed black line) at $\Delta_2 = 1$ for all p . This corresponds to the point where the uninformative fixed point $m = 0$ loses its local stability.
- The **information theoretic threshold** (solid red line). Here $m^* > 0$ and the MMSE jumps to a value strictly smaller than one.
- The **algorithmic threshold** (solid cyan line). This is where the fixed point of AMP jumps to the $\text{MMSE} < 1$. For $p = 3$ this line coincides with a segment of the stability threshold while for $p \geq 4$ it is strictly above.
- The **dynamic threshold** (dotted orange line). Here the most informative fixed point (the one with largest m_{AMP}) disappears.

In Figs. 9, and 10 we plot the evolution of the magnetization m , as found through the fixed points of the SE equation, for several fixed values of Δ_p and $p = 3$ and $p = 4$, respectively. The values of Δ_p are identified by the vertical cuts in the phase diagrams of Fig. 7.

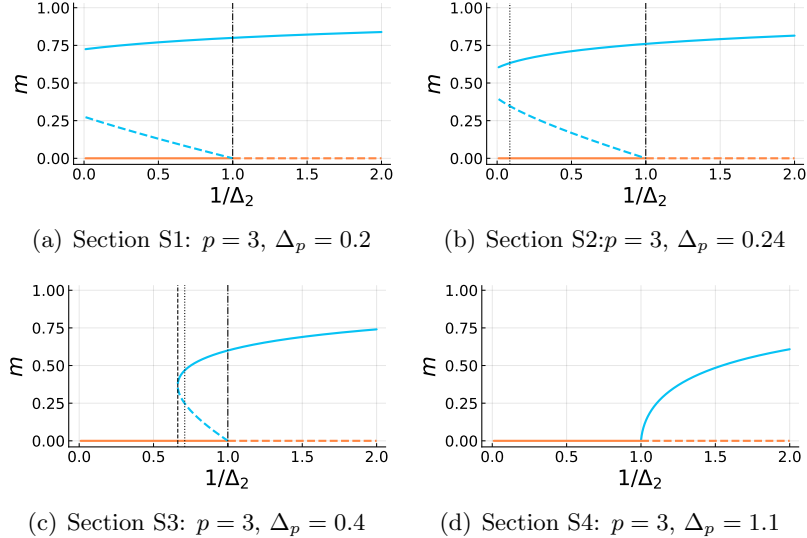


Figure 9: Fixed points of Eq. (59) as a function of Δ_2 for $p = 3$ and several fixed values of Δ_p . The values of Δ_p correspond to the vertical cuts in the left panel of Fig. 7. Solid lines are stable fixed point, dashed lines are unstable fixed points. The blue line represent informative fixed points with positive overlap with the signal while the orange line represent a uninformative fixed points with no overlap with the signal. Starting from high Δ_2 an informative fixed point appears at the dynamical threshold (vertical dashed line) but is energetically disfavored until the information theoretic threshold (vertical dotted line) and finally it becomes the only stable solution crossing the algorithmic threshold (vertical dotted-dashed line). When the transition is continuous the three vertical threshold lines merge and we have a single second order phase transition, which here occurs at $\Delta_p \geq 1$.

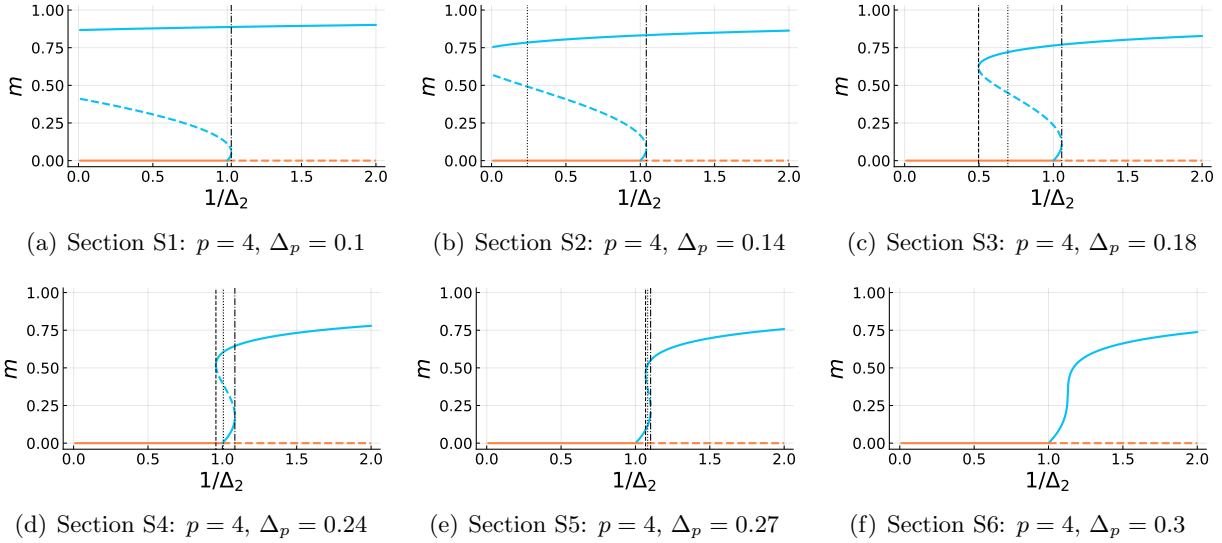


Figure 10: Fixed points Eq. (59) as a function of Δ_2 for $p = 4$ and several fixed values of Δ_p . The values of Δ_p correspond to the vertical cuts of the right panel of Fig. 7. The situation is qualitatively similar to Fig. 9, the difference being only the presence of the hybrid-hard phase. We can observe that when the transition is discontinuous, figure from (a) to (e), for $1/\Delta_2 > 1.0$ the uninformative solution becomes unstable and continuously goes to a stable-informative solution which is not the optimal one.

C Langevin Algorithm and its state evolution

The main goal of our analysis is to compare AMP with the performance of the Langevin dynamics. The advantage of the spiked matrix-tensor model is that in this case the Langevin dynamics can be studied in the large N limit through integro-differential equations for the correlation function, $C(t, t') = \lim_{N \rightarrow \infty} \sum_i \langle x_i(t) x_i(t') \rangle / N$, the response function $R(t, t') = \lim_{N \rightarrow \infty} \frac{1}{N} \sum_i \frac{d \langle x_i(t) \rangle}{d \eta_i(t')}$ and the magnetization $\bar{C}(t) = \lim_{N \rightarrow \infty} \sum_i \langle x_i(t) x_i^* \rangle / N$.

To obtain these equations we use the techniques developed in the context of mean-field spin glass systems [43, 68]. We call $\eta_i(t)$ a time dependent noise and we indicate with $\langle \cdot \rangle$ the average with respect to it. The noise is Gaussian and characterized by $\langle \eta_i(t) \rangle = 0$ for all t and $i = 1, \dots, N$ and $\langle \eta_i(t) \eta_j(t') \rangle = 2\delta_{ij}\delta(t - t')$. As before we will denote by $\mathbb{E}[\dots]$ the average with respect to the realization of disorder that in this case goes back to the specific realization of the signal.

Before proceeding, it is useful to introduce a set of auxiliary variables that will help in the following. For $k \in \{2, p\}$ we define $r_k \equiv r_k(t) = 2 / (k T_k(t) \Delta_k)$, $f_k(x) = x^k / 2$ and $m(t) \doteq \frac{1}{N} \sum_i x_i(t) x_i^*$, and the random variable $\tilde{\xi}_{i_1 \dots i_k} \equiv \frac{1}{\Delta_k} \xi_{i_1 \dots i_k} \sim \mathcal{N}(0, 1/\Delta_k)$. The time dependence in T_k , will be used in the tensor-annealing protocol that will be used to avoid part of the Langevin hard phase. We introduce a time dependent Hamiltonian

$$\begin{aligned} \mathcal{H}(t) = & -\frac{1}{T_2(t)\sqrt{N}} \sum_{i < j} \tilde{\xi}_{ij} x_i(t) x_j(t) - \frac{\sqrt{(p-1)!}}{T_p(t) N^{\frac{p-1}{2}}} \sum_{i_1 < \dots < i_p} \tilde{\xi}_{i_1 \dots i_p} x_{i_1}(t) \dots x_{i_p}(t) \\ & - N r_2(t) f_2(m(t)) - N r_p(t) f_p(m(t)), \end{aligned}$$

and the associated Langevin dynamics

$$\begin{aligned} \dot{x}_i(t) = & -\mu(t) x_i(t) - \frac{\partial \mathcal{H}}{\partial x_i}(t) - \eta_i(t) = -\mu(t) x_i(t) - \frac{1}{T_2(t)\sqrt{N}} \sum_{j \neq i} \tilde{\xi}_{ij} x_j(t) + \\ & + r_2(t) f'_2(m(t)) - \frac{\sqrt{(p-1)!}}{T_p(t) N^{\frac{p-1}{2}}} \sum_{(i, i_1, \dots, i_{p-1}) \setminus i} \tilde{\xi}_{i i_1 \dots i_{p-1}} x_{i_1}(t) \dots x_{i_{p-1}}(t) + r_p(t) f'_p(m(t)) - \eta_i(t), \end{aligned} \quad (66)$$

with μ a Langrange multiplier that enforces the spherical constraint $\sum_{i=1}^N x_i^2(t) = N$. If $T_k(t) = 1$ for all $k = 2, p$, the stationary equilibrium distribution for the Langevin dynamics is given by the posterior measure. Using Ito's lemma one finds

$$\frac{1}{N} \frac{d}{dt} \sum_i x_i^2(t) = \frac{2}{N} \sum_i x_i(t) \dot{x}_i(t) + 2.$$

Since the spherical constraint imposes the left-hand-side to be zero, one obtains a condition on the right-hand-side. By plugging the expression (66) in it, one gets that in the large N limit

$$\mu(t) = 1 - 2\mathcal{H}_2(t) - p\mathcal{H}_p(t) \quad (67)$$

where

$$\mathcal{H}_k = -\frac{\sqrt{(k-1)!}}{T_k(t)N^{\frac{k-1}{2}}} \sum_{i_1 < \dots < i_k} \tilde{\xi}_{i_1 \dots i_k} x_{i_1}(t) \dots x_{i_k}(t) - N r_k(t) f_k(m(t)) \quad k = 2, p \quad (68)$$

are the parts of the Hamiltonian defined in Eq. (C) relative to the matrix ($k = 2$) and to the tensor ($k = p$).

Note that we have not specified any initial condition for the variables $x_i(t = 0)$. Therefore, since we always employ the spherical constraint, the initial condition for the dynamics is a point on the N dimensional hypersphere $|x|^2 = N$ extracted with the flat measure.

In order to analyze the Langevin dynamics in the large N limit, we will use the dynamical cavity method [43, 69, 70]. We will consider a system of N variables, with $N \gg 1$, and add a new one. This new variable will be considered as a small perturbation to the original system but at the same time will be treated self consistently.

C.1 Dynamical Mean-Field Equations

In the following we will drop the time dependence for simplicity restoring it only when it is needed. Given the system with N variables $i = 1 \dots N$, we add a new one, say $i = 0$, and define $\tilde{m} = \frac{1}{N+1} \sum_{i=0}^N x_i x_i^* \simeq \frac{1}{N} \sum_{i=0}^N x_i x_i^*$ (henceforth we use the symbol \simeq to denote two quantities that are equal up to terms that vanish in the large- N limit). The Langevin equation associated to the new variable is

$$\dot{x}_0 = -\mu x_0 - \frac{1}{T_2(t)\sqrt{N}} \sum_{j(\neq 0)} \tilde{\xi}_{0j} x_j + r_2 f'_2(\tilde{m}) - \frac{\sqrt{(p-1)!}}{T_p(t)N^{\frac{p-1}{2}}} \sum_{(0, i_1, \dots, i_{p-1}) \setminus 0} \tilde{\xi}_{0i_1 \dots i_{p-1}} x_{i_1} \dots x_{i_{p-1}} + r_p f'_p(\tilde{m}) - \eta_0, \quad (69)$$

where we used that $N \simeq N + 1$ for $N \gg 1$. We will consider the contribution of the new variable on the others in perturbation theory. In the dynamical equations for the variables $i = 1, \dots, N$ we can isolate the variable $i = 0$ and write

$$\begin{aligned} \dot{x}_i = & -\mu x_i - \frac{1}{T_2(t)\sqrt{N}} \sum_{j(\neq i, 0)} \tilde{\xi}_{ij} x_j + r_2 f'_2(m) - \frac{\sqrt{(p-1)!}}{T_p(t)N^{\frac{p-1}{2}}} \sum_{(i, i_1, \dots, i_{p-1}) \setminus i, 0} \tilde{\xi}_{ii_1 \dots i_{p-1}} x_{i_1} \dots x_{i_{p-1}} \\ & + r_p f'_p(m) - \eta_i + H_i, \end{aligned} \quad (70)$$

with

$$H_i(t) = (r_2 f''_2(m) + r_p f''_p(m)) \frac{1}{N} x_0 - \frac{1}{T_2(t)\sqrt{N}} \tilde{\xi}_{0i} x_0 - \frac{\sqrt{(p-1)!}}{T_p(t)N^{\frac{p-1}{2}}} \sum_{(i, 0, i_1, \dots, i_{p-2}) \setminus i, 0} \tilde{\xi}_{i0i_1 \dots i_{p-2}} x_0 x_{i_1} \dots x_{i_{p-2}}. \quad (71)$$

Consider the unperturbed variables $x_i^0 = x_i|_{H_i=0}$. At leading order in N we can write

$$x_i \simeq x_i^0 + \int_{t_o}^t dt' \frac{\delta x_i(t)}{\delta H_i(t')} \Big|_{H_i=0} H_i(t'). \quad (72)$$

In the dynamical equation for the variable 0 we can identify a piece associated to the unperturbed variables x_i^0 . This term can be thought of collectively as a stochastic term $\Xi(t)$

$$\begin{aligned} \dot{x}_0 = & -\mu x_0 - \overbrace{\frac{1}{T_2(t)\sqrt{N}} \sum_{j(\neq 0)} \tilde{\xi}_{0j} x_j^0 - \frac{\sqrt{(p-1)!}}{T_p(t)N^{\frac{p-1}{2}}} \sum_{(0,i_1,\dots,i_{p-1})\setminus 0} \tilde{\xi}_{0i_1\dots i_{p-1}} x_{i_1}^0 \dots x_{i_{p-1}}^0 - \eta_0}^{\doteq \Xi(t)} + \\ & + r_2 f'_2(m) + r_p f'_p(m) + \left(r_2 f''_2(m) + r_p f''_p(m) \right) \frac{1}{N} x_0 - \frac{1}{T_2(t)\sqrt{N}} \sum_{j(\neq 0)} \tilde{\xi}_{0j} \int_{t_o}^t dt' \frac{\delta x_j(t)}{\delta H_j(t')} \Big|_{H_j=0} H_j(t') + \quad (73) \\ & - \left[\frac{\sqrt{(p-1)!}}{T_p(t)N^{\frac{p-1}{2}}} \sum_{(0,i_1,\dots,i_{p-1})\setminus 0} \tilde{\xi}_{0i_1\dots i_{p-1}} \int_{t_o}^t dt' \frac{\delta x_{i_1}(t)}{\delta H_{i_1}(t')} \Big|_{H_{i_1}=0} H_{i_1}(t') x_{i_2}^0 \dots x_{i_{p-1}}^0 + \text{permutations} \right]. \end{aligned}$$

Indeed $\Xi(t)$ encodes the effect of a kind of bath made by of the unperturbed variables $i = 1, \dots, N$ to the new one. We can show that at leading order in N , $\Xi(t)$ is a Gaussian noise with zero mean and variance given by

$$\begin{aligned} \mathbb{E}\langle \Xi(t) \Xi(t') \rangle = & 2\delta(t-t') - \mathbb{E} \left[\frac{1}{T_2(t)T_2(t')N} \sum_{j(\neq 0)} \sum_{l(\neq 0)} \tilde{\xi}_{0j} \tilde{\xi}_{0l} x_j^0(t) x_l^0(t') \right] + \\ & - \mathbb{E} \left[\frac{(p-1)!}{T_p(t)T_p(t')N^{p-1}} \sum_{(0,i_1,\dots,i_{p-1})\setminus 0} \sum_{(0,j_1,\dots,j_{p-1})\setminus 0} \tilde{\xi}_{0i_1\dots i_{p-1}} \tilde{\xi}_{0j_1\dots j_{p-1}} x_{i_1}^0 \dots x_{i_{p-1}}^0 x_{j_1}^0 \dots x_{j_{p-1}}^0 \right] \end{aligned}$$

and the second term can be simplified as

$$\begin{aligned} \mathbb{E} \left[\frac{(p-1)!}{T_p(t)T_p(t')N^{p-1}} \sum_{(0,i_1,\dots,i_{p-1})\setminus 0} \sum_{(0,j_1,\dots,j_{p-1})\setminus 0} \tilde{\xi}_{0i_1\dots i_{p-1}} \tilde{\xi}_{0j_1\dots j_{p-1}} x_{i_1}^0 \dots x_{i_{p-1}}^0 x_{j_1}^0 \dots x_{j_{p-1}}^0 \right] = \\ \simeq \frac{(p-1)!}{N^{p-1}} \frac{1}{T_p(t)T_p(t')\Delta_p} \sum_{(0,i_1,\dots,i_{p-1})\setminus 0} \langle x_{i_1}^0(t) x_{i_1}^0(t') \dots x_{i_{p-1}}^0(t) x_{i_{p-1}}^0(t') \rangle = \frac{1}{T_p(t)T_p(t')\Delta_p} C^{p-1}(t,t'), \end{aligned}$$

where we used $\sum_{(i_1,\dots,i_k)} = \frac{1}{k!} \sum_{\substack{1 \leq i_1, \dots, i_k \leq N}}$, we neglected terms sub-leading in N , and we used the definition of the dynamical correlation function

$$C(t,t') = \frac{1}{N} \sum_{i=1}^N \langle x_i(t) x_i(t') \rangle.$$

Therefore we have

$$\mathbb{E}\langle \Xi(t) \rangle = 0; \quad (74)$$

$$\mathbb{E}\langle \Xi(t) \Xi(t') \rangle = 2\delta(t-t') + \frac{1}{T_2(t)T_2(t')} C(t,t') + \frac{1}{T_p(t)T_p(t')\Delta_p} C^{p-1}(t,t'). \quad (75)$$

Now we can focus of the deterministic term coming from the first order perturbation in (73). Consider just the integral for the p -body term, the other will be given by setting $p=2$

$$\begin{aligned} \frac{\sqrt{(p-1)!}}{T_p(t)N^{\frac{p-1}{2}}} \sum_{(0,i_1,\dots,i_{p-1})\setminus 0} \tilde{\xi}_{0i_1\dots i_{p-1}} \int_{t_o}^t dt' \frac{\delta x_{i_1}(t)}{\delta H_{i_1}(t')} \Big|_{H_{i_1}=0} H_{i_1}(t') x_{i_2}^0 \dots x_{i_{p-1}}^0 + \text{permutations} = \\ \simeq \frac{(p-1)!}{T_p(t)N^{p-1}} \sum_{(0,i_1,\dots,i_{p-1})\setminus 0} \tilde{\xi}_{0i_1\dots i_{p-1}}^2 \int_{t_o}^t dt' \frac{1}{T_p(t')} \frac{\delta x_{i_1}(t)}{\delta H_{i_1}(t')} \Big|_{H_{i_1}=0} x_{i_1}^0(t) x_{i_1}^0(t') \dots x_{i_{p-2}}^0(t) x_{i_{p-2}}^0(t') x_0(t') + \\ + \text{permutations} \simeq -\frac{p-1}{T_p(t)\Delta_p} \int_{t_o}^t dt' \frac{1}{T_p(t')} R(t,t') C^{p-2}(t,t') x_0(t') \end{aligned} \quad (76)$$

where we have used the definition of the response function

$$R(t, t') = \frac{1}{N} \sum_{i=1}^N \left\langle \frac{\delta x_i(t)}{\delta H_i(t')} \right\rangle .$$

Plugging (76) into (73) we obtain an effective dynamical equation for the new variable in terms of the correlation and response function of the system with N variables

$$\begin{aligned} \dot{x}_0(t) = & -\mu(t)x_0(t) + \Xi(t) + r_p f'_p(\bar{C}(t)) + r_2 f'_2(\bar{C}(t)) + \\ & + \frac{p-1}{T_p(t)\Delta_p} \int_{t_o}^t dt'' \frac{1}{T_p(t'')} R(t, t'') C^{p-2}(t, t'') x_0(t'') + \frac{1}{T_2(t)\Delta_2} \int_{t_o}^t dt'' \frac{1}{T_2(t'')} R(t, t'') x_0(t'') . \end{aligned} \quad (77)$$

In order to close Eq. (77) we need to give the recipe to compute the correlation and response function.

C.2 Integro-differential equations

In order to obtain the final equations for dynamical order parameters we will assume that the new variable x_0 is a typical one, namely it has the same statistical nature of all the others. Therefore we can assume that

$$\begin{aligned} C(t, t') & \doteq \mathbb{E}\langle x_0(t)x_0(t') \rangle \\ R(t, t') & \doteq \mathbb{E}\left\langle \frac{\delta x_0(t)}{\delta \Xi(t')} \right\rangle \\ \bar{C}(t) & \doteq \mathbb{E}\langle x_0(t)x_0^* \rangle . \end{aligned} \quad (78)$$

Eqs. (78) give a way to obtain the equation for all the correlation functions. Indeed we can consider Eq. (77), multiply it by $x_0(t')$, or differentiate it with respect to an external field $h_0(t')$, or multiply it by x_0^* and we can average the results over the disorder and thermal noise. Using the following identity

$$\begin{aligned} \mathbb{E}\langle \Xi(t)x_0(t') \rangle & = \int \mathcal{D}\Xi(t) \Xi(t)x_0(t') e^{-\int d\bar{t}d\tilde{t}\Xi(\bar{t})\mathbb{K}^{-1}(\bar{t}, \tilde{t})\Xi(\tilde{t})} = \\ & = - \int dt'' \int \mathcal{D}\Xi(t) x_0(t') \frac{\delta}{\delta \Xi(t'')} e^{-\int d\bar{t}d\tilde{t}\Xi(\bar{t})\mathbb{K}^{-1}(\bar{t}, \tilde{t})\Xi(\tilde{t})} \mathbb{K}(t, t'') = \\ & = \int dt'' \mathbb{E}\left\langle \frac{\delta x_0(t')}{\delta \Xi(t'')} \right\rangle \mathbb{K}(t, t'') = \int dt'' R(t', t'') \mathbb{K}(t, t'') = \\ & = 2R(t', t) + \frac{1}{T_p(t)\Delta_p} \int_{t_o}^{t'} dt'' \frac{1}{T_p(t'')} R(t', t'') C^{p-1}(t, t'') + \frac{1}{T_2(t)\Delta_2} \int_{t_o}^{t'} dt'' \frac{1}{T_2(t'')} R(t', t'') C(t, t'') \end{aligned} \quad (79)$$

we get the following Langevin State Evolution (LSE) equations

$$\begin{aligned} \frac{\partial}{\partial t} C(t, t') & = \mathbb{E}\langle \dot{x}_0(t)x_0(t') \rangle = 2R(t', t) - \mu(t)C(t, t') + r_p(t)f'_p(\bar{C}(t))\bar{C}(t') + r_2(t)f'_2(\bar{C}(t))\bar{C}(t') + \\ & + (p-1)\frac{1}{T_p(t)\Delta_p} \int_{t_o}^t dt'' \frac{1}{T_p(t'')} R(t, t'') C^{p-2}(t, t'') C(t', t'') + \\ & + \frac{1}{T_p(t)\Delta_p} \int_{t_o}^{t'} dt'' \frac{1}{T_p(t'')} R(t', t'') C^{p-1}(t, t'') + \\ & + \frac{1}{T_2(t)\Delta_2} \int_{t_o}^t dt'' \frac{1}{T_2(t'')} R(t, t'') C(t', t'') + \frac{1}{T_2(t)\Delta_2} \int_{t_o}^{t'} dt'' \frac{1}{T_2(t'')} R(t', t'') C(t, t'') ; \end{aligned} \quad (80)$$

$$\begin{aligned} \frac{\partial}{\partial t} R(t, t') & = \mathbb{E}\left\langle \frac{\delta \dot{x}_0(t)}{\delta \Xi(t')} \right\rangle = \\ & = \delta(t - t') - \mu(t)R(t, t') + (p-1)\frac{1}{T_p(t)\Delta_p} \int_{t'}^t dt'' \frac{1}{T_p(t'')} R(t, t'') R(t'', t') C^{p-2}(t, t'') + \\ & + \frac{1}{T_2(t)\Delta_2} \int_{t'}^t dt'' \frac{1}{T_2(t'')} R(t, t'') R(t'', t') ; \end{aligned} \quad (81)$$

$$\begin{aligned} \frac{\partial}{\partial t} \bar{C}(t) &= \mathbb{E}\langle \dot{x}_0(t)x_0^* \rangle = \\ &= -\mu(t)\bar{C}(t) + r_p(t)f'_p(\bar{C}(t)) + r_2(t)f'_2(\bar{C}(t)) + \end{aligned} \quad (82)$$

$$\begin{aligned} &+ (p-1)\frac{1}{T_p(t)\Delta_p} \int_{t_o}^t dt'' \frac{1}{T_p(t'')} R(t, t'') C^{p-2}(t, t'') \bar{C}(t'') + \frac{1}{T_2(t)\Delta_2} \int_{t_o}^t dt'' \frac{1}{T_2(t'')} R(t, t'') \bar{C}(t'') ; \\ \mu(t) &= 1 + r_p(t)f'_p(\bar{C}(t))\bar{C}(t) + r_2(t)f'_2(\bar{C}(t))\bar{C}(t) + \\ &+ p\frac{1}{T_p(t)\Delta_p} \int_{t_o}^t dt'' \frac{1}{T_p(t'')} R(t, t'') C^{p-1}(t, t'') + 2\frac{1}{T_2(t)\Delta_2} \int_{t_o}^t dt'' \frac{1}{T_2(t'')} R(t, t'') C(t, t'') . \end{aligned} \quad (83)$$

Note that the last equation for $\mu(t)$ is obtained by imposing the spherical constraint $C(t, t) = 1 \forall t$ using the fact that $0 = \frac{dC(t, t)}{dt} = \frac{\partial C(t, t')}{\partial t} \Big|_{t'=t} + \frac{\partial C(t', t)}{\partial t} \Big|_{t'=t}$. The boundary conditions of this equations are: $C(t, t) = 1$ the spherical constrain, $R(t, t) = 0$ which comes from causality in the Itô approach and $R(t, t' \rightarrow t^-) = 1$. The initial condition for $\bar{C}(0) = \bar{C}_0$ is the overlap with the initial configuration with the true signal. If the initial configuration is random, $\bar{C}_0 = 0$ but will have finite size fluctuations, as in the case of AMP. Therefore we can think that $\bar{C}_0 = \epsilon$ being ϵ an arbitrary small positive number.

D Numerical solution of the LSE equations

The dynamical equations (80-81-82-83) were integrated numerically using two schemes:

- fixed time-grid: the derivatives were discretized and integrated according to their causal structure. This method is suited only for short times (up to 500 time units);
- dynamic time-grid: the step size is doubled after a given number of steps and the equations are solved self-consistently for every waiting-time. This is the approach proposed in [44] and described in Appendix C of [71]. It allows integration up to very large times (up to 10^6 time units).

The results of these algorithms are concisely reported in the phase diagram shown in the main paper. In what follows we will present the algorithms and a series of investigations that we carried out to check their stability, we will explain the procedure followed to delimit the Langevin hard region, and we will discuss how we can enter into part of that region by choosing a proper annealing protocol. The codes are available online [46].

D.1 Fixed time-grid ($2 + p$)-spin

In this approach time-derivatives and integrals were discretized using $\frac{\partial}{\partial t} f(t, t') \simeq \frac{1}{\Delta t} [f(t + \Delta t, t') - f(t, t')]$, and the trapezoidal rule for integration $\int_0^t f(t) dt \simeq \frac{\Delta t}{2} \sum_{l=0}^{t/\Delta t-1} [f(l\Delta t) + f((l+1)\Delta t)]$. For instance we defined a function for computing the update in the the response function, (81) as follows

$$\begin{aligned} R(t + \Delta t, t') &= R(t, t') - \Delta t \mu(t) R(t, t') + \frac{1}{2} \frac{\Delta t^2}{\Delta_2} \sum_{l=t'/\Delta t}^{t/\Delta t-1} [R(t, l\Delta t) R(l\Delta t, t') + R(t, (l+1)\Delta t) R((l+1)\Delta t, t')] + \\ &+ (p-1) \frac{\Delta t^2}{\Delta_p} \sum_{l=t'/\Delta t}^{t/\Delta t-1} [C^{p-2}(t, l\Delta t) R(t, l\Delta t) R(l\Delta t, t') + C^{p-2}(t, (l+1)\Delta t) R(t, (l+1)\Delta t) R((l+1)\Delta t, t')] . \end{aligned}$$

Analogously we defined the other integrators. A simple causal integration scheme, being careful with the Itô prescription, gives the pseudo-code below.

```
C(0, 0) ← 1; R(0, 0) ← 0;  $\bar{C}(0) \leftarrow \bar{C}_0$ ;  
for  $t \leq t_{\max}$  do
```

```

 $C(t + \Delta t, t + \Delta t) \leftarrow 1; R(t + \Delta t, t + \Delta t) \leftarrow 0;$ 
 $\mu(t) \leftarrow \text{compute\_mu}(C, R, \bar{C}, t);$ 
 $\bar{C}(t + \Delta t) \leftarrow \text{compute\_mag}(\mu, C, R, \bar{C}, t);$ 
for  $t' \leq t$  do
   $C(t + \Delta t, t') \leftarrow \text{compute\_C}(\mu, C, R, \bar{C}, t');$ 
   $R(t + \Delta t, t') \leftarrow \text{compute\_R}(\mu, C, R, \bar{C}, t');$ 
end for
 $R(t + \Delta t, t) \leftarrow 1;$ 
end for

```

D.2 Dynamical time-grid $(2 + p)$ -spin

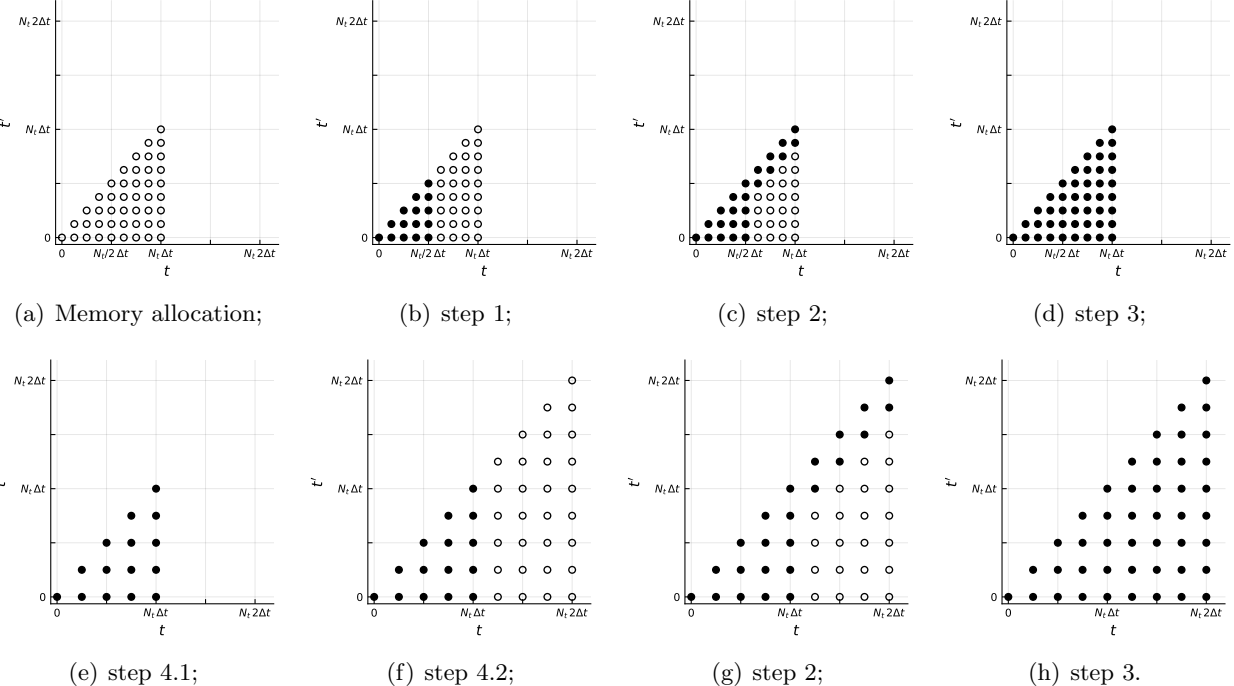


Figure 11: Representation of the initialization and the first two iterations for the evaluation of a two-times observable using the dynamic-grid algorithm. The empty circles represent slots allocated in memory but not associated to any specific value, while the full circles are memory slots already associated. For any two time function, it first allocates the memory (a), than it fills half of the grid by linear propagation (b). Still using linear propagation it fills the slots with $t - t' \ll 1$ (c), and it sets the other values by imposing self-consistency (d). Finally it halves the grid (e), doubles time step and it allocates the memory (f). Then the algorithm loops following the same scheme as in (b-c-d-e).

The numerical scheme we are going to discuss is presented in the Bayes-optimal case where $T_2(t) \equiv T_p(t) \equiv 1$. However the derivation that we propose can be easily generalized to the case where the T s assume different values, but are constants. Therefore we do not employ this algorithm to solve the LSE equations in the annealing protocol for which instead we use the fixed time-grid algorithm. It is convenient to manipulate the equations to obtain an equivalent set of equations for the functions $C(t, t')$, $Q(t, t') \doteq 1 - C(t, t') - \int_{t'}^t R(t, t'') dt''$, $\bar{C}(t)$, where $Q(t, t')$ represents the deviation from Fluctuation Dissipation Theorem (FDT) at time t starting from time t' . Indeed when the FDT theorem holds, it states that $R(t, t') = -\partial_t C(t, t')$.

We briefly anticipate the strategy that the algorithm uses to solve the equations. The algorithm discretizes the times into N_t intervals, first starting from the boundary conditions, $C(t, t) = 1$, $Q(t, t) = 0$ and $\bar{C} =$

$\bar{C}_0 \in [0; 1]$, it fills the grid for small times (or small time differences $\tau = t - t' \ll 1$) using linear propagation. Given a time t and the initial guess for the Lagrange multiplier obtained by the linear propagator, the integrals are discretized and evaluated, then the results are used to update the value of the Lagrange multiplier. This procedure is repeated iteratively until convergence. Once that the first grid is filled, it follows a coarse-graining procedure where the sizes of the time intervals are doubled and only half of the information is retained. This procedure is repeated a fixed number of doubling of the original grid. The doubling scheme allows to explore exponentially long times at the cost of losing part of the information, the direct consequence of this is the loss of stability for very large times (especially when the functions $C(t, t')$, $R(t, t')$, $\bar{C}(t)$ undergo fast changes at large times).

Dynamical equations in the algorithm. We recall the function $f_k(x) = \frac{x^k}{2}$ and its derivatives, $f'_k(x) = \frac{kx^{k-1}}{2}$ and $f''_k(x) = \frac{k(k-1)x^{k-2}}{2}$. For simplicity in the notation, we introduce also $f_k(t, t') \doteq f_k(C(t, t'))$

$$\begin{aligned}
(\partial_t + \mu(t))C(t, t') &= 2R(t', t) + r_2\bar{C}(t')f'_2(\bar{C}(t)) + r_p\bar{C}(t')f'_p(\bar{C}(t)) + \\
&+ \frac{1}{\Delta_2} \int_0^{t'} dt'' f'_2(t, t'') R(t', t'') + \frac{1}{\Delta_2} \int_0^t dt'' f''_2(t, t'') R(t, t'') C(t', t'') + \\
&+ \frac{2}{p\Delta_p} \int_0^{t'} dt'' f'_p(t, t'') R(t', t'') + \frac{2}{p\Delta_p} \int_0^t dt'' f''_p(t, t'') R(t, t'') C(t', t''), \\
(\partial_t + \mu(t))R(t, t') &= \delta(t - t') + \frac{1}{\Delta_2} \int_{t'}^t dt'' f''_2(t, t'') R(t, t'') R(t'', t') + \\
&+ \frac{2}{p\Delta_p} \int_{t'}^t dt'' f''_p(t, t'') R(t, t'') R(t'', t'), \\
(\partial_t + \mu(t))\bar{C}(t) &= r_2 f'_2(\bar{C}(t)) + r_p f'_p(\bar{C}(t)) + \\
&+ \frac{1}{\Delta_2} \int_0^t dt'' f''_2(t, t'') R(t, t'') \bar{C}(t'') + \frac{2}{p\Delta_p} \int_0^t dt'' f''_p(t, t'') R(t, t'') \bar{C}(t''), \\
\mu(t) &= 1 + r_2\bar{C}(t)f'_2(\bar{C}(t)) + r_p\bar{C}(t)f'_p(\bar{C}(t)) + \\
&+ \frac{2}{\Delta_2} \int_0^t dt'' f'_2(t, t'') R(t, t'') + \frac{2}{\Delta_p} \int_0^t dt'' f'_p(t, t'') R(t, t'').
\end{aligned}$$

Following the lines of [71], we introduce the FDT violation function, $Q(t, t')$, and after some manipulation the system becomes

$$\begin{aligned}
(\partial_t + \mu(t))C(t, t') &= \bar{C}(t') \left[r_2 f'_2(\bar{C}(t)) + r_p f'_p(\bar{C}(t)) \right] + \\
&+ \frac{1}{\Delta_2} \left\{ \int_0^{t'} dt'' \left[f'_2(t, t'') \frac{\partial Q(t', t'')}{\partial t''} + f''_2(t, t'') \frac{\partial Q(t, t'')}{\partial t''} C(t', t'') \right] + \right. \\
&- \left. \int_{t'}^t dt'' \left[f'_2(t, t'') \frac{\partial C(t'', t')}{\partial t''} - f''_2(t, t'') \frac{\partial Q(t, t'')}{\partial t''} C(t'', t') \right] + f'_2(1)C(t, t') - f'_2(t, 0)C(t', 0) \right\} + \\
&+ \frac{2}{p\Delta_p} \left\{ \int_0^{t'} dt'' \left[f'_p(t, t'') \frac{\partial Q(t', t'')}{\partial t''} + f''_p(t, t'') \frac{\partial Q(t, t'')}{\partial t''} C(t', t'') \right] + \right. \\
&- \left. \int_{t'}^t dt'' \left[f'_p(t, t'') \frac{\partial C(t'', t')}{\partial t''} - f''_p(t, t'') \frac{\partial Q(t, t'')}{\partial t''} C(t'', t') \right] + f'_p(1)C(t, t') - f'_p(t, 0)C(t', 0) \right\}, \tag{84}
\end{aligned}$$

$$\begin{aligned}
(\partial_t + \mu(t))Q(t, t') &= \mu(t) - 1 + \frac{1}{\Delta_2} \left\{ - \int_{t'}^t dt'' f'_2(t, t'') \frac{\partial Q(t'', t')}{\partial t''} + \int_{t'}^t dt'' f''_2(t, t'') \frac{\partial Q(t, t'')}{\partial t''} [Q(t'', t') - 1] + \right. \\
&+ f'_2(1)[Q(t, t') - 1] + f'_2(t, 0)C(t', 0) - \int_0^{t'} dt'' \left[f'_2(t, t'') \frac{\partial Q(t', t'')}{\partial t''} + f''_2(t, t'') \frac{\partial Q(t, t'')}{\partial t''} C(t', t'') \right] \left. \right\} + \\
&+ \frac{2}{p\Delta_p} \left\{ - \int_{t'}^t dt'' f'_p(t, t'') \frac{\partial Q(t'', t')}{\partial t''} + \int_{t'}^t dt'' f''_p(t, t'') \frac{\partial Q(t, t'')}{\partial t''} [Q(t'', t') - 1] + \right. \\
&+ f'_p(1)[Q(t, t') - 1] + f'_p(t, 0)C(t', 0) - \int_0^{t'} dt'' \left[f'_p(t, t'') \frac{\partial Q(t', t'')}{\partial t''} + f''_p(t, t'') \frac{\partial Q(t, t'')}{\partial t''} C(t', t'') \right] \left. \right\} + \\
&- \bar{C}(t') \left[r_2 f'_2(\bar{C}(t)) + r_p f'_p(\bar{C}(t)) \right], \tag{85}
\end{aligned}$$

$$\begin{aligned}
(\partial_t + \mu(t))\bar{C}(t) &= r_2 f'_2(\bar{C}(t)) + r_p f'_p(\bar{C}(t)) + \frac{1}{\Delta_2} \left\{ f'_2(1)\bar{C}(t) - f'_2(t, 0)\bar{C}(0) - \int_0^t dt'' f'_2(t, t'') \frac{d}{dt''} \bar{C}(t'') + \right. \\
&+ \int_0^t dt'' f''_2(t, t'') \frac{\partial Q(t, t'')}{\partial t''} \bar{C}(t'') \left. \right\} + \frac{2}{p\Delta_p} \left\{ f'_p(1)\bar{C}(t) - f'_p(t, 0)\bar{C}(0) - \int_0^t dt'' f'_p(t, t'') \frac{d}{dt''} \bar{C}(t'') + \right. \\
&+ \int_0^t dt'' f''_p(t, t'') \frac{\partial Q(t, t'')}{\partial t''} \bar{C}(t'') \left. \right\}, \tag{86}
\end{aligned}$$

$$\begin{aligned}
\mu(t) &= 1 + r_2 \bar{C}(t) f'_2(\bar{C}(t)) + r_p \bar{C}(t) f'_p(\bar{C}(t)) + \frac{2}{\Delta_2} [f_2(1) - f_2(t, 0)] + \frac{2}{\Delta_p} [f_p(1) - f_p(t, 0)] + \\
&+ \int_0^t dt'' \left[\frac{2}{\Delta_2} f'_2(t, t'') + \frac{2}{\Delta_p} f'_p(t, t'') \right] \frac{\partial Q(t, t'')}{\partial t''}, \tag{87}
\end{aligned}$$

further simplifications can be obtained introducing $\mu'(t) = \mu(t) - \frac{2}{\Delta_2} f_2(1) - \frac{2}{\Delta_p} f_p(1)$

$$\begin{aligned}
\mu'(t) &= 1 + r_2 \bar{C}(t) f'_2(\bar{C}(t)) + r_p \bar{C}(t) f'_p(\bar{C}(t)) - \frac{2}{\Delta_2} f_2(t, 0) - \frac{2}{\Delta_p} f_p(t, 0) + \\
&+ \int_0^t dt'' \left[\frac{2}{\Delta_2} f'_2(t, t'') + \frac{2}{\Delta_p} f'_p(t, t'') \right] \frac{\partial Q(t, t'')}{\partial t''}, \tag{88}
\end{aligned}$$

$$\begin{aligned}
(\partial_t + \mu'(t))C(t, t') &= \bar{C}(t') \left[r_2 f'_2(\bar{C}(t)) + r_p f'_p(\bar{C}(t)) \right] + \\
&+ \frac{1}{\Delta_2} \left\{ \int_0^{t'} dt'' \left[f'_2(t, t'') \frac{\partial Q(t', t'')}{\partial t''} + f''_2(t, t'') \frac{\partial Q(t, t'')}{\partial t''} C(t', t'') \right] + \right. \\
&- \int_{t'}^t dt'' \left[f'_2(t, t'') \frac{\partial C(t'', t')}{\partial t''} - f''_2(t, t'') \frac{\partial Q(t, t'')}{\partial t''} C(t'', t') \right] - f'_2(t, 0)C(t', 0) \left. \right\} + \\
&+ \frac{2}{p\Delta_p} \left\{ \int_0^{t'} dt'' \left[f'_p(t, t'') \frac{\partial Q(t', t'')}{\partial t''} + f''_p(t, t'') \frac{\partial Q(t, t'')}{\partial t''} C(t', t'') \right] + \right. \\
&- \int_{t'}^t dt'' \left[f'_p(t, t'') \frac{\partial C(t'', t')}{\partial t''} - f''_p(t, t'') \frac{\partial Q(t, t'')}{\partial t''} C(t'', t') \right] - f'_p(t, 0)C(t', 0) \left. \right\}, \tag{89}
\end{aligned}$$

$$\begin{aligned}
(\partial_t + \mu'(t))Q(t, t') &= \mu'(t) - 1 - \bar{C}(t') \left[r_2 f_2'(\bar{C}(t)) + r_p f_p'(\bar{C}(t)) \right] + \\
&+ \frac{1}{\Delta_2} \left\{ - \int_{t'}^t dt'' f_2'(t, t'') \frac{\partial Q(t'', t')}{\partial t''} + \int_{t'}^t dt'' f_2''(t, t'') \frac{\partial Q(t, t'')}{\partial t''} [Q(t'', t') - 1] + \right. \\
&+ f_2'(t, 0)C(t', 0) - \int_0^{t'} dt'' \left[f_2'(t, t'') \frac{\partial Q(t', t'')}{\partial t''} + f_2''(t, t'') \frac{\partial Q(t, t'')}{\partial t''} C(t', t'') \right] \left. \right\} + \\
&+ \frac{2}{p\Delta_p} \left\{ - \int_{t'}^t dt'' f_p'(t, t'') \frac{\partial Q(t'', t')}{\partial t''} + \int_{t'}^t dt'' f_p''(t, t'') \frac{\partial Q(t, t'')}{\partial t''} [Q(t'', t') - 1] + \right. \\
&+ f_p'(t, 0)C(t', 0) - \int_0^{t'} dt'' \left[f_p'(t, t'') \frac{\partial Q(t', t'')}{\partial t''} + f_p''(t, t'') \frac{\partial Q(t, t'')}{\partial t''} C(t', t'') \right] \left. \right\}, \tag{90}
\end{aligned}$$

$$\begin{aligned}
(\partial_t + \mu'(t))\bar{C}(t) &= r_2 f_2'(\bar{C}(t)) + r_p f_p'(\bar{C}(t)) + \frac{1}{\Delta_2} \left\{ - f_2'(t, 0)\bar{C}(0) + \right. \\
&- \int_0^t dt'' f_2'(t, t'') \frac{d}{dt''} \bar{C}(t'') + \int_0^t dt'' f_2''(t, t'') \frac{\partial Q(t, t'')}{\partial t''} \bar{C}(t'') \left. \right\} + \\
&+ \frac{2}{p\Delta_p} \left\{ - f_p'(t, 0)\bar{C}(0) + \right. \\
&- \int_0^t dt'' f_p'(t, t'') \frac{d}{dt''} \bar{C}(t'') + \int_0^t dt'' f_p''(t, t'') \frac{\partial Q(t, t'')}{\partial t''} \bar{C}(t'') \left. \right\}. \tag{91}
\end{aligned}$$

First order expansion coefficients. In the numerics we will initialize the grid by a linear propagation of the initial conditions. To determine the coefficients to use we can expand the functions up the second term for small values of τ (and in the last equation of t)

$$\begin{aligned}
C(t' + \tau, t') &= C(t', t') + C^{(1,0)}(t', t')\tau + \frac{1}{2}C^{(2,0)}(t', t') + O(\tau^3), \\
Q(t' + \tau, t') &= Q(t', t') + Q^{(1,0)}(t', t')\tau + \frac{1}{2}Q^{(2,0)}(t', t') + O(\tau^3), \\
\bar{C}(t) &= \bar{C}(0) + \bar{C}^{(1)}(0)\tau + \frac{1}{2}\bar{C}^{(2)}(0) + O(t^3). \tag{92}
\end{aligned}$$

This gives the following coefficients: $C(t, t) = 1$, $C^{(1,0)}(t, t) = -1$, $Q(t, t) = 0$, $Q^{(1,0)}(t, t) = 0$, $\bar{C}(0) = \bar{C}_0$ and $\bar{C}^{(1)}(0) = [r_2 f_2'(\bar{C}_0) + r_p f_p'(\bar{C}_0)](1 - (\bar{C}_0)^2) - \bar{C}_0$, where \bar{C}_0 is the initial value of the overlap with the signal.

Numerical integration and derivation. The set of equations derived above presents six types of integrals

$$\begin{aligned}
I_{ij}^{(1AB)} &= \int_{t_j}^{t_i} dt'' A(t_i, t'') \frac{\partial B(t'', t_j)}{\partial t''}; \\
I_{ij}^{(2ABC)} &= \int_{t_j}^{t_i} dt'' A(t_i, t'') \frac{\partial B(t_i, t'')}{\partial t''} C(t'', t_j); \\
I_{ij}^{(3AB)} &= \int_0^{t_j} dt'' A(t_i, t'') \frac{\partial B(t_i, t'')}{\partial t''}; \\
I_{ij}^{(4ABC)} &= \int_0^{t_j} dt'' A(t_i, t'') \frac{\partial B(t_i, t'')}{\partial t''} C(t_j, t''); \\
I_i^{(5AB)} &= \int_0^{t_i} dt'' A(t_i, t'') \frac{\partial B(t'')}{\partial t''}; \\
I_i^{(6ABC)} &= \int_0^{t_i} dt'' A(t_i, t'') \frac{\partial B(t_i, t'')}{\partial t''} C(t''). \tag{93}
\end{aligned}$$

The integrals can be easily discretized

$$\begin{aligned}
I_{ij}^{(2ABC)} &= \sum_{t_l=t_j+\delta t}^{t_i} \int_{t_l-\delta t}^{t_l} dt'' A(t_i, t'') \frac{\partial B(t_i, t'')}{\partial t''} C(t'', t_j) \simeq \\
&\simeq \sum_{t_l=t_j+\delta t}^{t_i} \int_{t_l-\delta t}^{t_l} dt_1 A(t_i, t_1) \int_{t_l-\delta t}^{t_l} dt_2 \frac{\partial B(t_i, t_2)}{\partial t_2} \int_{t_l-\delta t}^{t_l} dt_3 C(t_3, t_j) \simeq \\
&\simeq \sum_{t_l=t_j+\delta t}^{t_i} \frac{1}{2} [A(t_i, t_l) + A(t_i, t_l - \delta t)] [B(t_i, t_l) - B(t_i, t_l - \delta t)] \frac{1}{2} [C(t_l, t_j) + C(t_l - \delta t, t_j)].
\end{aligned}$$

In particular the 6 integrals become

$$\begin{aligned}
I_{ij}^{(1AB)} &= A_{im} B_{mj} - A_{ij} B_{jj} + \sum_{l=m+1}^i \frac{1}{2} (A_{il} + A_{i(l-1)}) (B_{lj} - B_{(l-1)j}) + \\
&\quad - \sum_{l=j+1}^m \frac{1}{2} (B_{lj} + B_{(l-1)j}) (A_{il} - A_{i(l-1)}) = \\
&= A_{im} B_{mj} - A_{ij} B_{jj} + \sum_{l=m+1}^i dA_{il}^{(v)} (B_{lj} - B_{(l-1)j}) - \sum_{l=j+1}^m (A_{il} - A_{i(l-1)}) dB_{lj}^{(h)} ;
\end{aligned} \tag{93}$$

$$\begin{aligned}
I_{ij}^{(2ABC)} &= \sum_{l=j+1}^i \frac{1}{2} (A_{il} + A_{i(l-1)}) (B_{lj} - B_{(l-1)j}) \frac{1}{2} (C_{lj} + C_{(l-1)j}) = \\
&= \sum_{l=m+1}^i dA_{il}^{(h)} (B_{il} - B_{i(l-1)}) \frac{1}{2} (C_{lj} + C_{(l-1)j}) + \sum_{l=j+1}^m \frac{1}{2} (A_{il} + A_{i(l-1)}) (B_{il} - B_{i(l-1)}) dC_{lj}^{(v)} ;
\end{aligned} \tag{94}$$

$$I_{ij}^{(3AB)} = A_{ij} B_{jj} - A_{i0} B_{j0} - \sum_{l=1}^j (A_{il} - A_{i(l-1)}) dB_{jl}^{(v)} ; \tag{95}$$

$$I_{ij}^{(4ABC)} = \sum_{l=1}^j \frac{1}{2} (A_{il} + A_{i(l-1)}) (B_{il} - B_{i(l-1)}) dC_{jl}^{(v)} ; \tag{96}$$

$$I_i^{(5AB)} = \sum_{l=1}^i dA_{il}^{(v)} (B_l - B_{l-1}) ; \tag{97}$$

$$I_i^{(6ABC)} = \sum_{l=1}^i \frac{1}{2} (A_{il} + A_{i(l-1)}) (B_{il} - B_{i(l-1)}) dC_l , \tag{98}$$

where the superscript (v) and (h) represent the vertical (t') and horizontal (t) derivatives in the discretized times, see Fig. 11 for an intuitive understanding.

We also discretized the derivative using the last two time steps

$$\frac{d}{dt} g(t) = \frac{3}{2\delta t} g(t) - \frac{2}{\delta t} g(t - \delta t) + \frac{1}{2\delta t} g(t - 2\delta t) + O(\delta t^3) . \tag{99}$$

Given the time indices i and j , we will define and evaluate the following quantities

$$\begin{aligned}
&\{C_{ij}, Q_{ij}, M2_{ij}, N2_{ij}, Mp_{ij}, Np_{ij}, \text{Cbar}_i, P2_i, Pp_i, mu_i\} = \\
&= \{C(t_i, t_j), Q(t_i, t_j), f'_2(C(t_i, t_j)), f''_2(C(t_i, t_j)), f'_p(C(t_i, t_j)), f''_p(C(t_i, t_j)), \overline{C}(t_i), f'_2(\overline{C}(t_i)), f'_p(\overline{C}(t_i)), \mu(t_i)\}
\end{aligned}$$

plus the respective vertical and horizontal derivatives.

Calling $D_i = \frac{3}{2dt} + \mu'_i - \frac{1}{\Delta_2} M2_{ii} - \frac{2}{p\Delta_p} Mp_{ii}$, the original dynamical equations are integrated as follow

$$\begin{aligned} C_{ij}D_i &= \frac{2}{dt}C_{(i-1)j} - \frac{1}{2dt}C_{(i-2)j} + \text{Cbar}_j(r_2P2_i + r_pPp_i) + \\ &+ \frac{1}{\Delta_2} \left(-\dot{I}_{ij}^{(1)f'_2C} + I_{ij}^{(2)f''_2QC} + I_{ij}^{(3)f'_2Q} + I_{ij}^{(4)f''_2QC} - M2_{i0}C_{j0} \right) + \\ &+ \frac{2}{p\Delta_p} \left(-\dot{I}_{ij}^{(1)f'_pC} + I_{ij}^{(2)f''_pQC} + I_{ij}^{(3)f'_pQ} + I_{ij}^{(4)f''_pQC} - Mp_{i0}C_{j0} \right), \end{aligned} \quad (100)$$

$$\begin{aligned} Q_{ij}D_i &= \mu'_i - 1 + \frac{2}{dt}Q_{(i-1)j} - \frac{1}{2dt}Q_{(i-2)j} + \text{Cbar}_j(r_2P2_i + r_pPp_i) + \\ &+ \frac{1}{\Delta_2} \left(-\dot{I}_{ij}^{(1)f'_2Q} + I_{ij}^{(2)f''_2Q(Q-1)} - I_{ij}^{(3)f'_2Q} - I_{ij}^{(4)f''_2QC} - M2_{i0}C_{i0} \right) + \\ &+ \frac{2}{p\Delta_p} \left(-\dot{I}_{ij}^{(1)f'_pQ} + I_{ij}^{(2)f''_pQ(Q-1)} - I_{ij}^{(3)f'_pQ} - I_{ij}^{(4)f''_pQC} - Mp_{i0}C_{i0} \right), \end{aligned} \quad (101)$$

$$\begin{aligned} \text{Cbar}_iD_i &= \frac{2}{dt}\text{Cbar}_{i-1} - \frac{1}{2dt}\text{Cbar}_{i-2} + r_2P2_i + r_pPp_i + \\ &+ \frac{1}{\Delta_2} \left(-\dot{I}_i^{(5)f'_2\text{Cbar}} + I_i^{(6)f''_2QC\text{bar}} - M2_{i0}\text{Cbar}_0 \right) + \\ &+ \frac{2}{p\Delta_p} \left(-\dot{I}_i^{(5)f'_p\text{Cbar}} + I_i^{(6)f''_pQC\text{bar}} - Mp_{i0}\text{Cbar}_0 \right). \end{aligned} \quad (102)$$

In the systems we used \dot{I} to characterize the integrals where we remove from the sum the term present in the left-hand side (e.g. for C_{ij} eq. 100). Using Simpson's integration formula we define the increments

$$\begin{aligned} \Delta_{il} &= \frac{1}{12}(Q_{il} - Q_{i(l-1)})\{W_2^2[-(M2_{i(l+1)} + N2_{i(l+1)}C_{i(l+1)}) + 8(M2_{il} + N2_{il}C_{il}) + 5(M2_{i(l-1)} + N2_{i(l-1)}C_{i(l-1)})] + \\ &+ W_p^2[-(Mp_{i(l+1)} + Np_{i(l+1)}C_{i(l+1)}) + 8(Mp_{il} + Np_{il}C_{il}) + 5(Mp_{i(l-1)} + Np_{i(l-1)}C_{i(l-1)})]\} \end{aligned}$$

and we determine μ' as

$$\mu' = 1 + r_2P2_i + r_pPp_i + \delta\mu' + \sum_{l=1}^{i-N_t/4} \Delta_{il} - (W_2^2M2_{i0} + W_p^2Mp_{i0})C_{i0}, \quad (103)$$

with $\delta\mu'$ initially set to 0.

Algorithm: Here we describe the main steps of the algorithm, pictorially represented Fig. 11.

Discretize the time (t, t') in N_t (even) intervals, the results shown use $N_t = 1024$.

1. **Initialization.** Fill the first $N_t/2$ times by linear propagation of the value obtained from the perturbative analysis

$$C_{ij} = 1 - (i - j)dt; \quad (104)$$

$$Q_{ij} = 0; \quad (105)$$

$$\text{Cbar}_i = \bar{C}_0 + \left\{ \left[r_2f'_2(\bar{C}_0) + r_pf'_p(\bar{C}_0) \right] (1 + (\bar{C}_0)^2) - \bar{C}_0 \right\} dt; \quad (106)$$

$$M2_{ij} = f'_2(C_{ij}); \quad (107)$$

$$N2_{ij} = f''_2(C_{ij}); \quad (108)$$

$$Mp_{ij} = f'_p(C_{ij}); \quad (109)$$

$$Np_{ij} = f''_p(C_{ij}). \quad (110)$$

2. **Fill the grid (small τ).** Continue to propagate the values for small time differences $\tau = t - t' \ll 1$. In terms of the algorithm it means that we have some elements of the grid, N_c of them, close to the diagonal that will be updated by linear propagation because the approximation of small τ is still valid. In our simulation the first Δt is of the order 10^{-7} and $N_c = 2$.
3. **Fill the grid (larger τ).** The rest of the values will be copied from the previous t ($A_{t+\Delta t, t'} = A_{t, t'}$). These values are the initial guess for solving the self-consistent equations (100-101-102) and (103), in this procedure the derivatives are updated using the 2nd order discretization.
4. **Half the grid and expand.** The grid is decimated which means that each observable is contracted $A_{i,j} \leftarrow A_{2i,2j}$ and the derivate are updated as follows $dA_{i,j}^{(h)} \leftarrow \frac{1}{2}(dA_{2i,2j}^{(h)} + dA_{2i-1,2j}^{(h)})$, $dA_{i,j}^{(v)} \leftarrow \frac{1}{2}(dA_{2i,2j}^{(v)} + dA_{2i,2j-1}^{(v)})$. The new time step is now: $\Delta t \leftarrow 2\Delta t$.
5. **Start over from step 2.**

D.3 Numerical checks on the dynamical algorithm

The dynamic-grid algorithm has been checked in a variety of ways.

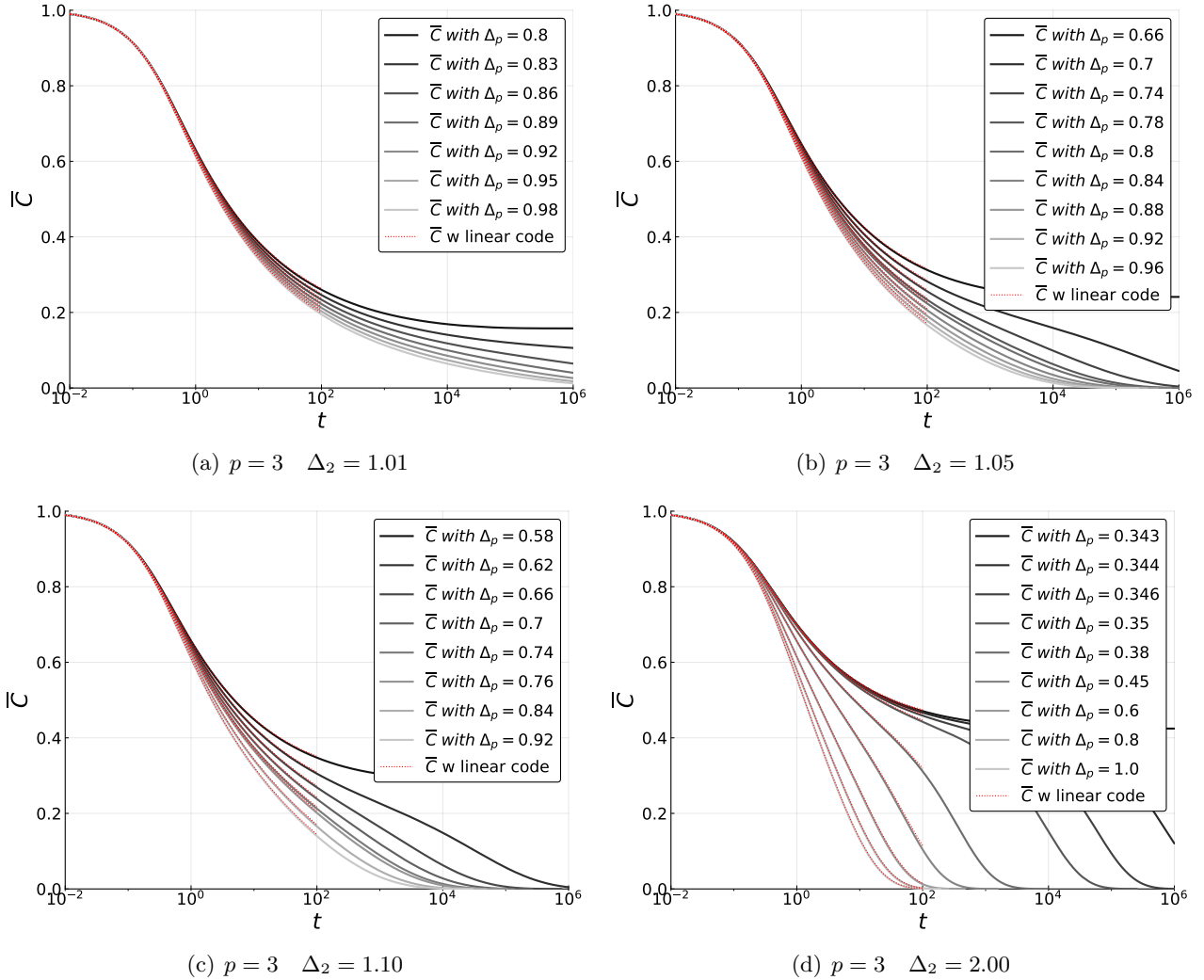


Figure 12: Evolution of the correlation with the signal starting from the solution, $\bar{C}_0 = 1.0$ at fixed Δ_2 for different Δ_p . The dotted red line overlapping with other lines, is the same quantity evaluated using the fixed grid algorithm up to time 100. We have started the LSE from an informative initial condition.

Cross-checking using the fixed-grid algorithm. For short times the dynamical equations were solved using the fixed-grid algorithm and compared with the outcome of the dynamic-grid algorithm, obtaining the same results, see Fig. 12. In the figure we used the fixed-grid with $t_{\max} = 100$ and the $\Delta t = 6.25 * 10^{-3}$.

Same magnetization in the easy region. In the impossible and easy regions, the overlap with the signal of both AMP and dynamic-grid integration, converges to the same value. In Fig. 13 we show the overlap obtained with AMP, black dashed line, and the overlap achieved by the integration scheme at a given time. We can see that the overlap with the signal as obtained solving the LSE equations converges to the same value of the fixed point of AMP. Given a fixed Δ_2 we can observe that the time to convergence increase very rapidly as we decrease Δ_p . We fitted this increase of the *relaxation time* to get the boundary of the Langevin hard region.

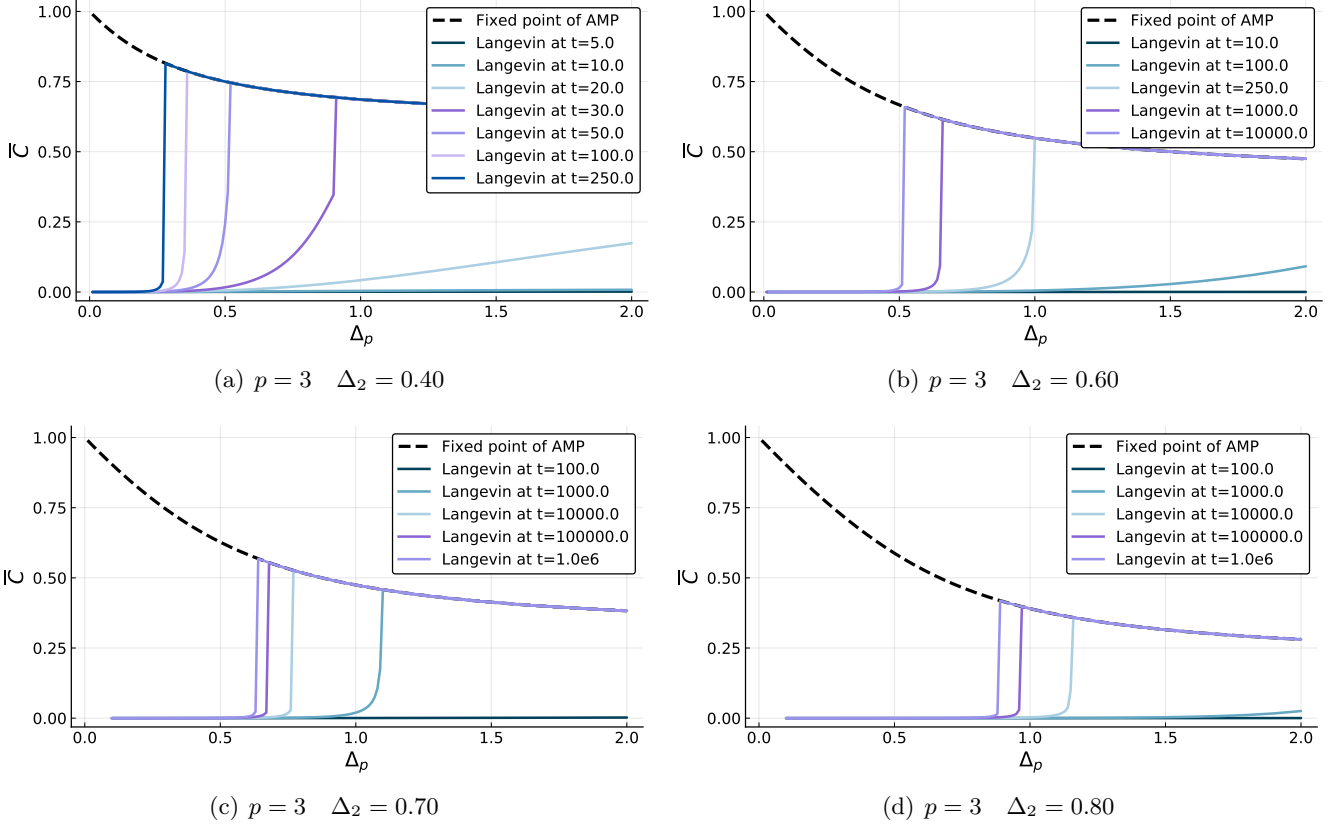


Figure 13: Correlation with the signal of AMP (dotted lines) and Langevin (solid lines) at k th iteration and t time respectively starting in both cases with an initial overlap of 10^{-4} . The black dashed line is the asymptotic value predicted with AMP. In the easy region, provided enough running time, Langevin dynamics finds the same alignment as AMP. The figures show qualitatively the same behaviour for different values of Δ_2 .

Dynamical transition. The dynamical transition where the finite magnetization fixed point disappears can be regarded as a clustering or dynamical glass transition. Indeed coming from the impossible phase, going towards the hard phase, at the dynamical transition the free energy landscape changes and the unique ergodic paramagnetic minimum of the impossible phase gets clustered into an exponential number of metastable glassy states (see Sec. E). Correspondingly the relaxation time of the Langevin algorithm diverges. Fitting this divergence with a power law we obtain an alternative estimation of the dynamical line. In the right panel of Fig. 14 we plot with yellow points the dynamical transition line as extracted from the fit of the relaxation time of the Langevin algorithm extracted coming from the impossible phase and entering in the hard phase.

D.4 Extrapolation procedure

In order to determine the Langevin Hard region, given a fixed value of Δ_p (Δ_2), we measure the relaxation time that it takes to relax to equilibrium. On approaching the Langevin hard region, this relaxation time increases and we extrapolate the growth to obtain the critical Δ_p^* (Δ_2^* respectively) where the relaxation time appears to diverge. The extrapolation is done starting from $\bar{C}_0 = 10^{-40}$ and assuming a power law divergence. Fig. 14 shows the results of this procedure for the cases 2 + 3 and 2 + 4. We remark that the divergence times increase as p increases. Therefor in reason of the instability of the code for large times it becomes difficult to extrapolate the threshold accurately. In particular in the right panel of Fig. 14 when estimating the threshold for 2 + 4, we consider horizontal sections and the points extrapolated for Δ_2 close to the threshold $\Delta_2 = 1.0$ are very hard to estimate because of these instabilities.

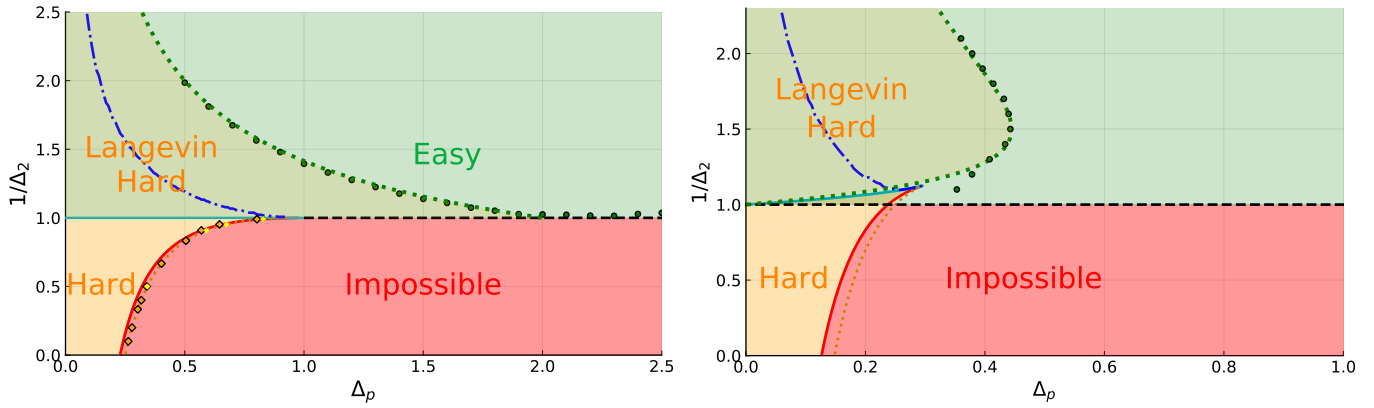


Figure 14: On the left: phase diagram of the spiked matrix-tensor model for $p = 3$ as presented in the left panel of Fig. 7 with the additional boundary of the Langevin hard phase (green circles and dotted green line). The data points (circles) have been obtained numerically by fitting the relaxation time at fixed Δ_p and increasing Δ_2 . The green dotted line are fixed points of expression (15). The blue dashed-dotted line marks a region above which we do not observe anymore a stable positive 1RSB complexity. Finally we plot with orange and yellow dots the dynamical transition line as extracted from the relaxation time of the Langevin algorithm coming from respectively the hard and impossible phase. On the right: phase diagram of the spiked matrix-tensor model for $p = 4$ as presented in the right panel of Fig. 7 with the additional Langevin hard phase boundary. The data points are obtained fixing Δ_2 and decreasing Δ_p . Also in this case we observe that Langevin hard phase extends in the AMP easy phase. Interestingly the Langevin hard phase here folds and presents a re-entrant behaviour, investigating the precise character of this reentrance is hampered by vicinity of the critical point and is left for future work. The blue dashed line marks a region above which we do not observe anymore a stable positive 1RSB complexity.

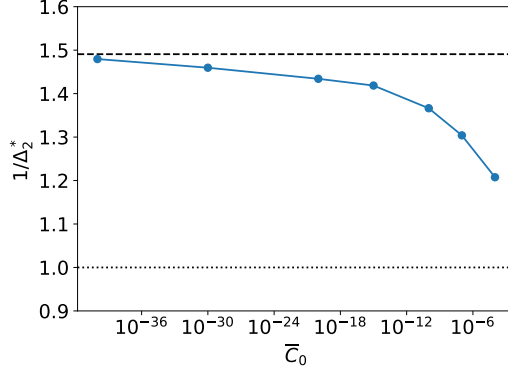


Figure 15: Estimated divergence point Δ_2^* at fixed $\Delta_p = 0.9$ with $p = 3$ as a function of the initial condition \bar{C} , ranging from 10^{-40} to 10^{-6} . The vertical axis is in linear scale while the horizontal axis is in log-scale. We observe that the dependence of estimated divergence points on the initial condition is consistent with the asymptotic value $1/\Delta_2^* = \sqrt{2/\Delta_p} \approx 1.491$ following from eq. (15), and depicted by the dashed line. The dotted line instead represents the AMP threshold for comparison.

Numerical checks on the extrapolation procedure. To test the quality of the fits we use a similar numerical procedure to locate the spinodal of the informative solution, which is given by the points where the informative solution ceases to exist. This spinodal must be the same for both the AMP and the Langevin algorithm [6].

Since we aim at studying the spinodal of the informative solution, we initialize the LSE with $\bar{C}_0 = 1$ and let it relax, measuring the time it takes to equilibrate at the value of \bar{C} given by the informative fixed point of AMP. We do this fixing Δ_2 and changing Δ_p . As we approach the critical $\Delta_{p,\text{dyn}}$, the relaxation time will diverge and we can fit this divergence with a power law. The dynamic threshold extracted in this way is finally compared with the one obtained from AMP. In Fig. 17 we show how this scheme has been applied for $\Delta_2 \in \{1.01, 1.05, 1.10, 2.00\}$. As we get closer to the critical line $\Delta_2 = 1$ the relaxation time increases (and the height of the plateau decreases), making the fit harder. All in all, we observe a very good agreement between the points found with these extrapolation procedures and the prediction obtained with AMP, as shown in Fig. 14.

D.5 Initial conditions

The LSE equations show a rather strong dependence on the initial condition \bar{C}_0 . A low initial magnetization will give a low initial momentum in the direction of the signal, as it can be observed in the linear expansion of \bar{C} Eq. (92), and consequently the system will not be able to cross even very small barriers. The direct consequence is that reducing the initial magnetization the estimated threshold will get worse, in the sense that a larger signal-to-noise ratio will be required to find the solution. This finding can be observed in Fig. 15, where different initial conditions are compared on the section $\Delta_p = 0.9$.

Finally we remark how the different initial conditions affect the phase diagram. In Fig. 16 we compare the Langevin hard-easy threshold evaluated starting from different initial condition, showing that the region gets larger as the initial condition decrease up to convergence.

D.6 Annealing protocol

In this section we show that using specific protocols that separate the matrix and tensor part of the cost function (something we do not allow in the main part of this paper for the purpose of having a model as generic as possible) we are able to enter in the Langevin hard region. A generic annealing scheme would lower the noises of both the channels simultaneously, which will not be able to avoid the Langevin hard region. Instead

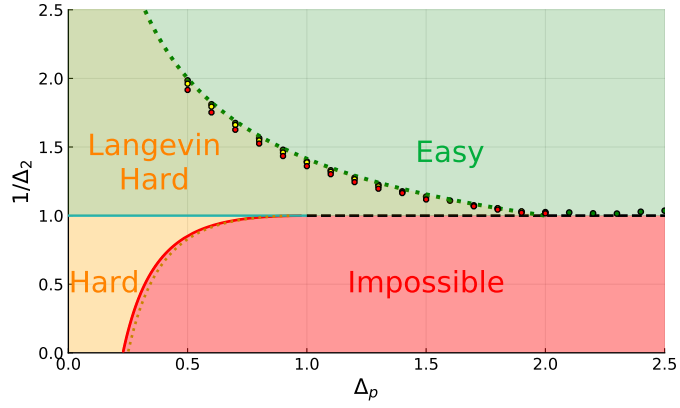


Figure 16: Phase diagram of the $p = 3$ model where we compare the threshold of the Langevin hard region using different values of the initial conditions, respectively: green circles $\bar{C}_0 = 10^{-40}$, yellow circles $\bar{C}_0 = 10^{-30}$, red circles $\bar{C}_0 = 10^{-20}$.

we can use the following protocol

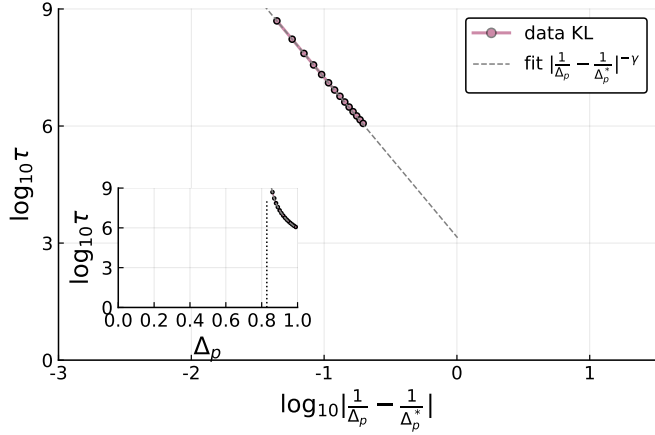
$$T_2 \equiv 1, \quad T_p \equiv T_p(t) = 1 + \frac{C}{\Delta_p} e^{-\frac{t}{\tau_{\text{ann}}}}. \quad (111)$$

The constant C allows to select at the initial time the desired effective $\Delta_{p,\text{eff}} = \Delta_p + C e^{-\frac{t}{\tau_{\text{ann}}}}$ far from (and much larger than) the original one. Instead τ_{ann} chooses the speed of the annealing protocol. Fig. 18 shows that using this protocol we are able to enter in Langevin Hard region even with Δ_2 close to the AMP threshold. To this purpose we initiated the effective $\Delta_{p,\text{eff}}$ close to 100 (i.e. $C = 100$), very far from the Langevin hard region, and we used different speeds for the annealing of Δ_p (different colors in the figures). In the figures we can observe that approaching the $\Delta_2 = 1$ we need slower and slower protocols (larger and larger τ_{ann}). The reason for this behavior is due to the fact that approaching $\Delta_2 = 1$ with $\Delta_p = 100$ a longer time is required to gain a non trivial overlap with the solution. Evidence of this growing timescale at $\Delta_p = 100$ is given in Fig. 19 where we show the relaxation time for magnetizing to the solution varying Δ_2 . In particular, we can observe that at $\Delta_2 = 0.70$ the relaxation time is of the order of 100 time units.

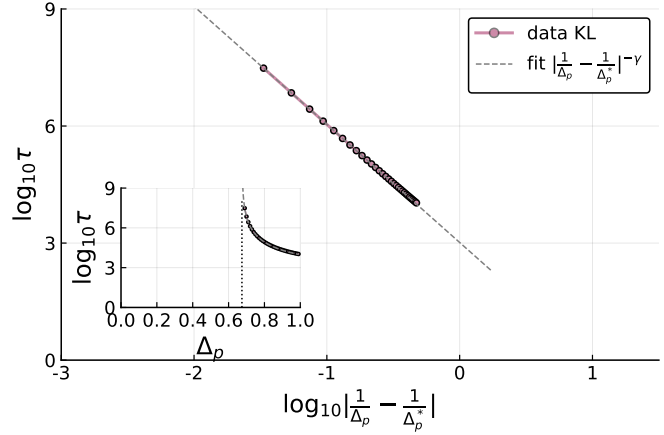
For the protocol to be successful it is therefore crucial that the annealing time τ_{ann} is large enough to give the possibility of magnetizing the solution before $\Delta_{p,\text{eff}}$ has significantly decreased towards Δ_p . According to this analysis, it is not surprising that in Fig. 18 for $\Delta_2 = 0.90$ the proposed protocol seems not to be successful. For this value of the parameter Δ_2 , the time to find a solution even with $\Delta_p = 100$ should be larger than 1000 time units, which is much larger than the used τ_{ann} and anyway out of the time window of our numerical solution. However, with an annealing time large enough it would be in principle possible to recover exactly the same boundaries of the AMP easy region.

E Glassy nature of the Langevin hard phase: the replica approach

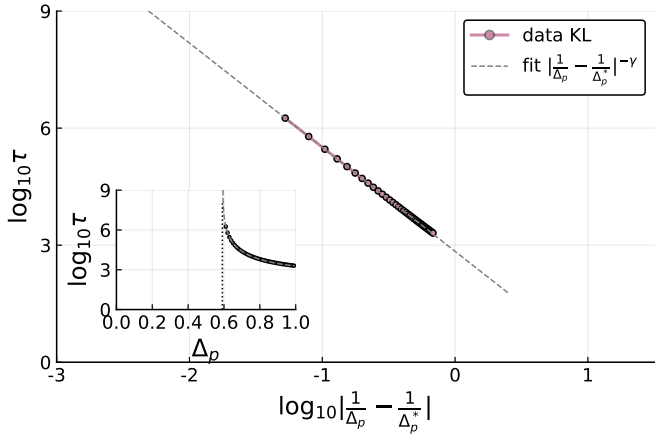
In this section we study the landscape of the spiked matrix-tensor problem following the approach of [25]. We underline here that we are interested in studying the free energy landscape problem rather than the energy landscape since the former is the relevant quantity for finite temperatures ($\beta = 1$ in our case, as discussed in Sec. A). The results of [25] suggest that the AMP-hard phase and part of the AMP-easy phase are glassy. Therefore we could expect that low magnetization glassy states trap the Langevin algorithm and forbid the relaxation to the equilibrium configurations that surrounds the signal. This may happen also in a region where AMP instead is perfectly fine in producing configurations strongly correlated with the signal. In order to check



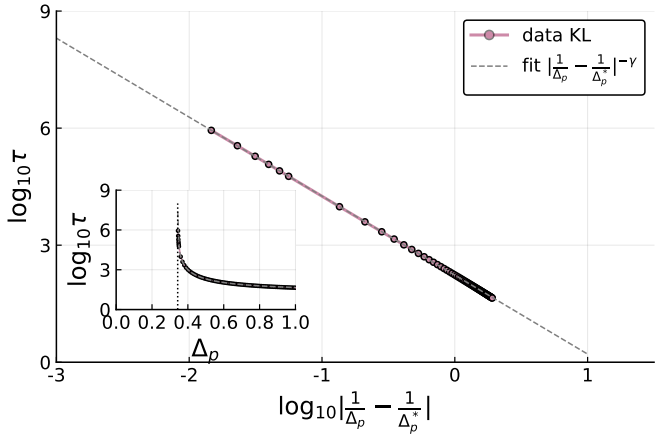
(a) $\Delta_2 = 1.01$: estimation 0.82857 (AMP 0.82719)



(b) $\Delta_2 = 1.05$: estimation 0.67447 (AMP 0.67382)

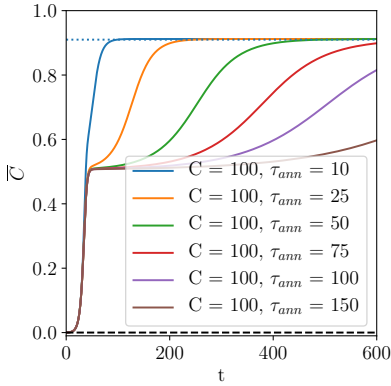


(c) $\Delta_2 = 1.10$: estimation 0.59104 (AMP 0.59034)

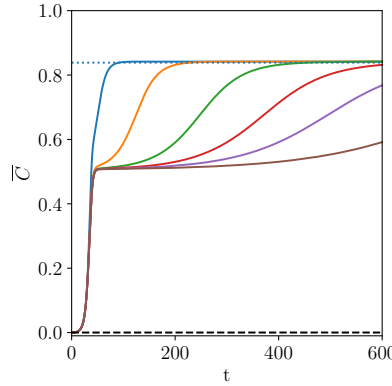


(d) $\Delta_2 = 2.00$: estimation 0.34326 (AMP 0.34314)

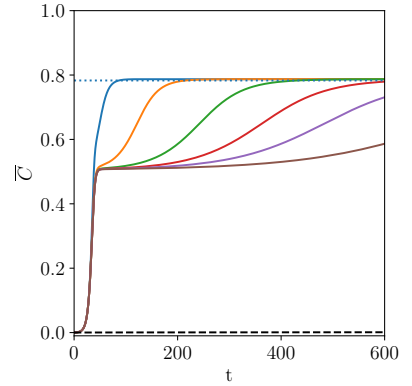
Figure 17: Relaxation time obtained from the LSE starting from an informative initial condition $\bar{C}_0 = 1$. The four cases refers to the $2 + 3$ model and are fitted with a power law and the relaxation time appears to diverge very close to point predicted by AMP (the AMP prediction is given in the captions).



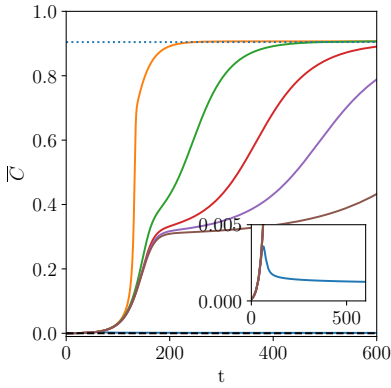
(a) $\Delta_2 = 0.50$, $\Delta_p = 0.10$



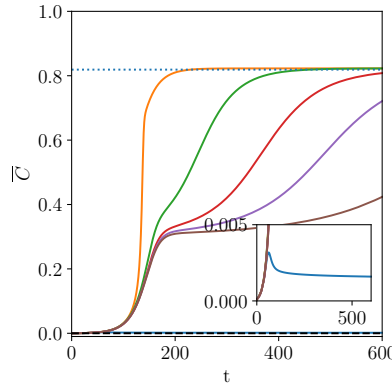
(b) $\Delta_2 = 0.50$, $\Delta_p = 0.20$



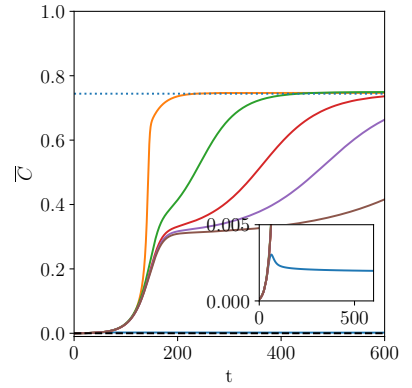
(c) $\Delta_2 = 0.50$, $\Delta_p = 0.30$



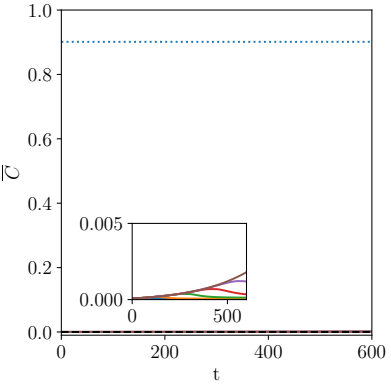
(d) $\Delta_2 = 0.70$, $\Delta_p = 0.10$



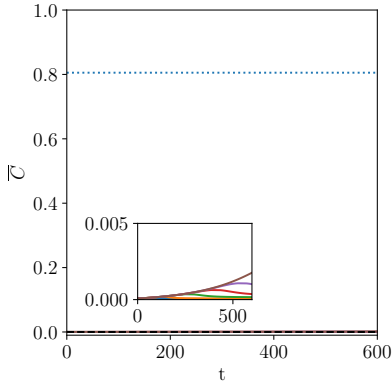
(e) $\Delta_2 = 0.70$, $\Delta_p = 0.20$



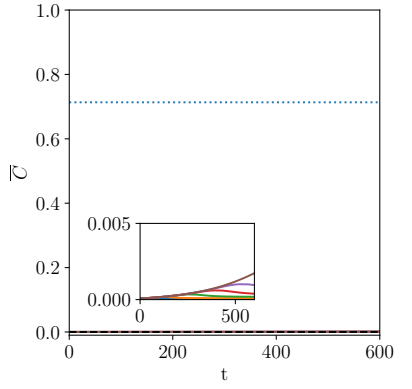
(f) $\Delta_2 = 0.70$, $\Delta_p = 0.30$



(g) $\Delta_2 = 0.90$, $\Delta_p = 0.10$



(h) $\Delta_2 = 0.90$, $\Delta_p = 0.20$



(i) $\Delta_2 = 0.90$, $\Delta_p = 0.30$

Figure 18: The figures show the correlation with the signal in time obtained using different annealing protocols, whose details are reported in the legend of the first figure. All the protocols have $C = 100$ which means that all the dynamics start with close effective $\Delta_p \sim 100$, $T_p(0)\Delta_p \simeq 100$ and start with an initial overlap $\bar{C}_0 = 10^{-4}$. What changes among the different lines is the relaxation speed, from the fastest, drawn in blue, to the slowest, drawn in brown. They are compared with the asymptotic value of AMP, dotted line, and the Langevin dynamics without tensor-annealing, dashed line.

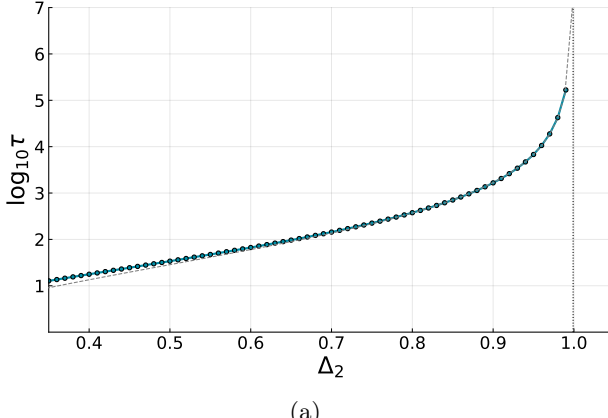


Figure 19: Relaxation times of Langevin dynamics at $\Delta_p = 100$ without using protocols starting from $\bar{C}_0 = 10^{-4}$.

this hypothesis we compute the logarithm of the number of glassy states, called the complexity by using the replica method [72, 25]. The goal of this analysis is to trace an additional line in the phase diagram that delimits the region where stable one step replica symmetry breaking (1RSB) metastable states exist. We conjecture that this provides a physical lower bound to the Langevin hard phase in the $(\Delta_p, 1/\Delta_2)$ phase diagram.

E.1 Computation of the complexity through the replica method

The replica trick is based on the simple identity: $\mathbb{E} \log x = \lim_{n \rightarrow 0} \frac{\partial}{\partial n} \mathbb{E} x^n$. Using this observation we can compute the expected value of the free energy, $\Phi = -(\log Z)/N$, averaging the Z^n and taking the limit $n \rightarrow 0$. This is in general as difficult as the initial problem, however, if we consider only integer n and extrapolate to 0, the computation becomes much less involved due to the fact that for integer n the average $\mathbb{E} x^n$ can be sometimes performed analytically. Indeed in this case the replicated partition function Z^n can be regarded as the partition function of n identical uncoupled systems or replicas. Averaging over the disorder we obtain a clean system of interacting replicas. The Hamiltonian of this system displays an emerging *replica symmetry* since it is left unchanged by a permutation of replicas. This symmetry can be spontaneously broken in certain disordered models where frustration is sufficiently strong [43].

In mean field models characterized by fully connected factor graphs, the resulting Hamiltonian of interacting replicas depends on the configuration of the system only through a simple order parameter, the overlap \tilde{Q} between them, which is a $n \times n$ matrix that describes the similarities of the configurations of different replicas in phase space. Furthermore the Hamiltonian is proportional to N which means that in the thermodynamic limit $N \rightarrow \infty$, the model can be solved using the saddle point method. In this case one needs to consider a simple ansatz for the saddle point structure of the matrix \tilde{Q} that allows to take the analytic continuation for $n \rightarrow 0$. The solution to this problem comes from spin glass theory and general details can be found in [43]. The saddle point solutions for \tilde{Q} can be classified according to the replica symmetry breaking level going from the replica symmetric solution where replica symmetry is not spontaneously broken to various degree of spontaneous replica symmetry breaking (including full-replica symmetry breaking). Here we will not review this subject but the interested reader can find details in [43]. The model we are analyzing can be studied in full generality at any degree of RSB (see for example [40, 41, 51] where the same models have been studied in absence of a signal). However here we will limit ourselves to consider saddle point solutions up to a 1RSB level.

The complexity of the landscape can be directly related to replica symmetry breaking. A replica symmetric solution implies an ergodic free energy landscape characterized by a single pure state. When replica symmetry is broken instead, a large number of pure states arises and the phase space gets clustered in a hierarchical way [43]. Making a 1RSB approximation means to look for a situation in which the hierarchical organization contains just one level: the phase space gets clustered into an exponential number of pure states with no further internal structure.

If we assume a 1RSB glassy landscape, we can compute the complexity of metastable states using a recipe due to Monasson [72] (see also [73] for a pedagogical introduction). The argument goes as follows.

Let us consider system with x *real* replicas infinitesimally coupled. If the free energy landscape is clustered into an exponential number of metastable states, the replicated partition function, namely the partition function of the system of x real replicas, can be written as

$$Z^x \simeq e^{N[\Sigma(f^*) - x\beta f^*]}$$

where f^* is the internal free energy of the dominant metastable states that is determined by the saddle point condition $\frac{d\Sigma}{df}(f^*) = \beta x$ and β the inverse temperature. Note that since we are interested in the Bayes optimal case, this corresponds to set $\beta = 1$. In the analysis we will consider a generic β before taking the limits in order to derive the averaged energy by taking its derivative. The function $\Sigma(f)$ is the complexity of metastable states having internal entropy f . Therefore, using the free parameter x we can reconstruct the form of $\Sigma(f)$ from the replicated free energy. In order to compute the replicated free energy we need to apply the replica trick on the replicated system, $\overline{\log Z^x} = \lim_{n \rightarrow 0} \frac{\partial}{\partial n} \overline{(Z^x)^n}$. Calling the replicated free energy $\Phi = -\frac{1}{N} \overline{\log Z^x}$, we get the complexity as $\Sigma = x \frac{\partial \Phi}{\partial x} - \Phi$.

We can now specify the computation to our case where the partition function is the normalization of the posterior measure. With simple manipulations of the equations [69], the partition function can be expressed as the integral over the overlap matrix

$$\overline{(Z^x)^n} = \overline{Z_x^n} \propto \int \prod_{ab} dQ_{ab} e^{NnxS(Q)} \simeq \limsup_Q e^{NnxS(Q)}; \quad (112)$$

where the overlap Q is a $(nx + 1) \times (nx + 1)$ matrix

$$Q = \left(\begin{array}{c|c} \frac{1}{m} & m \cdots m \\ \hline m & \tilde{Q} \\ \vdots & \\ m & \end{array} \right)$$

that contains a special row and column that encodes the overlap between different replicas with the signal and therefore the corresponding overlap is the *magnetization* m .

The 1RSB structure for the matrix \tilde{Q} can be obtained by defining the following $nx \times nx$ matrices: the identity matrix $\mathbb{I}_{ij} = \delta_{ij}$, the full matrix $\mathbb{J}_{nx,ij}^{(0)} = 1$, and $\mathbb{J}_{nx}^{(1)} = \text{diag}(J_x^{(0)}, \dots, J_x^{(0)})$ a block diagonal matrix where the diagonal blocks $J_x^{(0)}$ have size $x \times x$ and are matrices full of 1. In this case the 1RSB ansatz for \tilde{Q} reads

$$\tilde{Q} = (1 - q_M) \mathbb{I}_{nx} + (q_M - q_m) \mathbb{J}_{nx}^{(1)} + q_m \mathbb{J}_{nx}^{(0)}.$$

Using this ansatz we can compute $S(Q)$ that is given by

$$\begin{aligned} S(Q) &= \frac{1}{nx} \left[\frac{1}{2} \log \det Q + \frac{\beta^2}{2p\Delta_p} \sum_{ab} Q_{ab}^p + \frac{\beta^2}{4\Delta_2} \sum_{ab} Q_{ab}^2 \right] = \\ &= \frac{1}{2} \log(1 - q_M) + \frac{1}{2x} \log \frac{1 - q_M + x(q_M - q_m)}{1 - q_M} + \frac{1}{2} \frac{q_m - m^2}{1 - q_M + x(q_M - q_m)} + \\ &\quad + \frac{\beta^2}{2p\Delta_p} (1 - q_M^p + x(q_M^p - q_m^p) + 2m^p) + \frac{\beta^2}{4\Delta_2} (1 - q_M^2 + x(q_M^2 - q_m^2) + 2m^2). \end{aligned} \quad (113)$$

From Eq. (113) we obtain the saddle point equations

$$\begin{aligned}
0 &= 2 \frac{\partial S}{\partial q_M} = (x-1) \left[\frac{1}{x} \left(\frac{1}{1-q_M+x(q_M-q_m)} - \frac{1}{1-q_M} \right) - \frac{q_m-m^2}{[1-q_M+x(q_M-q_m)]^2} + \beta^2 \left(\frac{q_M^{p-1}}{\Delta_p} + \frac{q_M}{\Delta_2} \right) \right]; \\
0 &= 2 \frac{\partial S}{\partial q_m} = x \left[\frac{q_m-m^2}{[1-q_M+x(q_M-q_m)]^2} - \beta^2 \left(\frac{q_m^{p-1}}{\Delta_p} + \frac{q_m}{\Delta_2} \right) \right]; \\
0 &= \frac{\partial S}{\partial m} = \frac{-m}{1-q_M+x(q_M-q_m)} + \beta^2 \left(\frac{m^{p-1}}{\Delta_p} + \frac{m}{\Delta_2} \right).
\end{aligned} \tag{114}$$

The above 1RSB fixed point equations can be used to derive the de Almeida-Thouless instability of the RS solution towards 1RSB. This stability condition, sometimes called *the replicon* also determines the overlap of the marginal threshold states. The stability analysis is done by expansion of eqs. (114) in a small parameters $q_M - q_m = \varepsilon \ll 1$ and investigating whether under iterations such a small difference grows or decreases. This leads directly to the threshold condition on the overlap

$$\frac{1}{\beta^2(1-q^{\text{th}})^2} = (p-1) \frac{(q^{\text{th}})^{(p-2)}}{\Delta_p} + \frac{1}{\Delta_2}. \tag{115}$$

This condition is then used in the derivation of the Langevin threshold (15) in the main text.

From Eq. (113) we obtain also the averaged energy

$$E = \frac{\partial \overline{\log Z^x}}{\partial \beta} \Big|_{\beta=1} = \frac{1-q_M^p + x(q_M^p - q_m^p) + 2m^p}{p\Delta_p} + \frac{1-q_M^2 + x(q_M^2 - q_m^2) + 2m^2}{2\Delta_2}. \tag{116}$$

In particular the threshold states are characterized by $q_M = q^{\text{th}}$, fixed by Eq. (115), $q_m = 0$ and $m = 0$. Imposing these values, we can use the saddle point equation for q_M , Eq. 114, to fix the Parisi parameters x ,

$$x(q^{\text{th}}) = \frac{1}{(1-q^{\text{th}}) \left[\frac{(q^{\text{th}})^{p-1}}{\Delta_p} + \frac{q^{\text{th}}}{\Delta_2} \right]} - \frac{1}{q^{\text{th}}} + 1. \tag{117}$$

These pieces together give Eq. (12) showed in the main text.

Having obtained the energy we can consider $\beta = 1$ fixed for the rest of the analysis. We can observe that starting from this expression we can derive the RS free energy, (40), $q_M = q_m$ or equivalently in the limit $x \rightarrow 1$. The low magnetization solution to these equations gives the complexity of the metastable branch of the posterior measure which is given by

$$\begin{aligned}
-\Sigma(x; Q^*) &= -\frac{1}{2} \log \frac{1-q_M+x(q_M-q_m)}{1-q_M} + \frac{x}{2} \frac{q_M-q_m}{1-q_M+x(q_M-q_m)} - \frac{x^2}{2} \frac{(q_m-m^2)(q_M-q_m)}{[1-q_M+x(q_M-q_m)]^2} + \frac{x^2}{2} \frac{q_M^p-q_m^p}{p\Delta_p} + \\
&+ \frac{x^2}{2} \frac{q_M^2-q_m^2}{2\Delta_2}.
\end{aligned} \tag{118}$$

The free parameter x allows us to tune the free energy of the states of which we compute the complexity. Thus we can characterize the part of the phase diagram where an exponential number of states is present.

To complete the 1RSB analysis we compute the stability of the 1RSB saddle point solution for Q . This is done analogously to the derivation of the *replicon* condition (115), analyzing stability of the 1RSB towards further replica symmetry breaking. Following [74, 51] we obtain two replicon eigenvalues given by

$$\lambda_I = 1 - (1-q_M+x(q_M-q_m))^2 \left[(p-1) \frac{q_m^{p-2}}{\Delta_p} + \frac{1}{\Delta_2} \right], \tag{119}$$

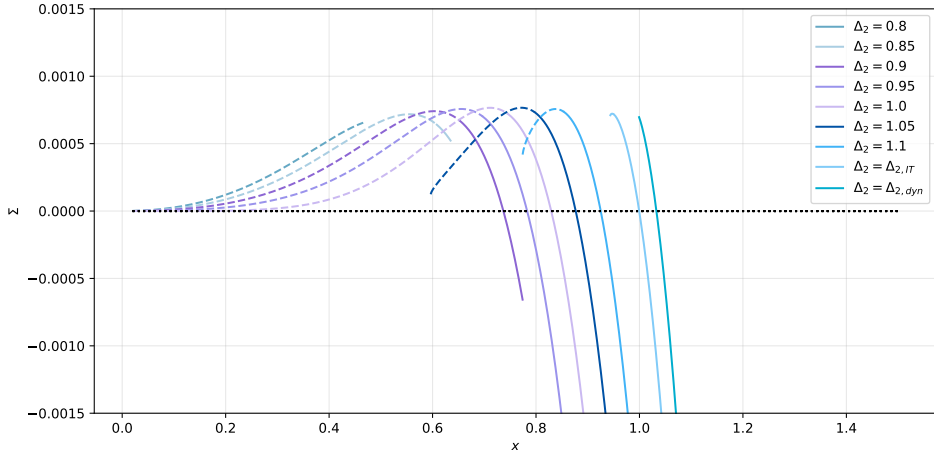


Figure 20: Complexity with as a function of the Parisi parameter x for $p = 3$ on the line $\Delta_p = 0.5$. The solid line characterizes the stable part of the complexity while the dashed line the unstable one.

$$\lambda_{II} = 1 - (1 - q_M)^2 \left[(p-1) \frac{q_M^{p-2}}{\Delta_p} + \frac{1}{\Delta_2} \right]. \quad (120)$$

We can analyze what happens to the landscape when we fix $\Delta_p < 1$ and we start from a large value of $\Delta_2 < \Delta_{2,\text{dyn}}(\Delta_p)$ and we decrease Δ_2 . In this case for sufficiently high Δ_2 and large enough Δ_p the system is in a paramagnetic phase and no glassy states are present. At the dynamical transition line instead we find a positive complexity as plotted in Fig. 20. At this point the equilibrium states that dominate the posterior measure are the so called *threshold* states for which the complexity is maximal. For those states the eigenvalue $\lambda_{II} = 0$ which confirms that these states are marginally stable [27]. Decreasing Δ_2 one crosses the information theoretic phase transition where the relevant metastable states that dominate the posterior measure have zero complexity. This corresponds to a freezing/condensation/Kauzmann transition. Below the information theoretic phase transition the thermodynamics of the posterior measure is dominated by the state containing the signal. However one can neglect the high magnetization solution of the 1RSB equations to get the properties of the metastable branch and computing the complexity of states that have zero overlap with the signal. The complexity curves as a function of the Parisi parameter x for decreasing values of Δ_2 are plotted in Fig. 20 for fixed $\Delta_p = 0.5$ and several Δ_2 . The curves contain a stable 1RSB part and an unstable one where λ_{II} is negative. The 1RSB line shown in Figs. 14 is obtained by looking at when the states with positive complexity and $\lambda_{II} = 0$ disappear. This means that it gives the point where the 1RSB marginally stable states disappear and therefore it is expected to be a lower bound for the disappearance of glassiness in the phase diagram. The important outcome of this analysis is that for $\Delta_2 < 1$ but not sufficiently small, namely in part of the AMP-easy phase, the replica analysis predicts the existence of 1RSB marginally stable glassy states that may trap the Langevin algorithm from relaxing towards the signal [25] and therefore supports the existence of the Langevin hard phase.

Finally in Fig. 21 we plot the complexity as a function of the internal free energy of the metastable states for some values of Δ_2 and Δ_p .

E.2 Breakdown of the fluctuation-dissipation theorem in the Langevin hard phase

When the Langevin algorithm is able to reach equilibrium, being it the signal or the paramagnetic state, it should satisfy the Fluctuation-Dissipation Theorem (FDT) according to which the response function is related to the correlation function through $R(t, t') = -\frac{\partial C(t, t')}{\partial t}$. Furthermore, time translational invariance (TTI) should arise implying that both correlation and response functions should be functions of only the time difference meaning that $R(t, t') = R(t - t')$ and $C(t, t') = C(t - t')$, note that all one time quantities are constant in

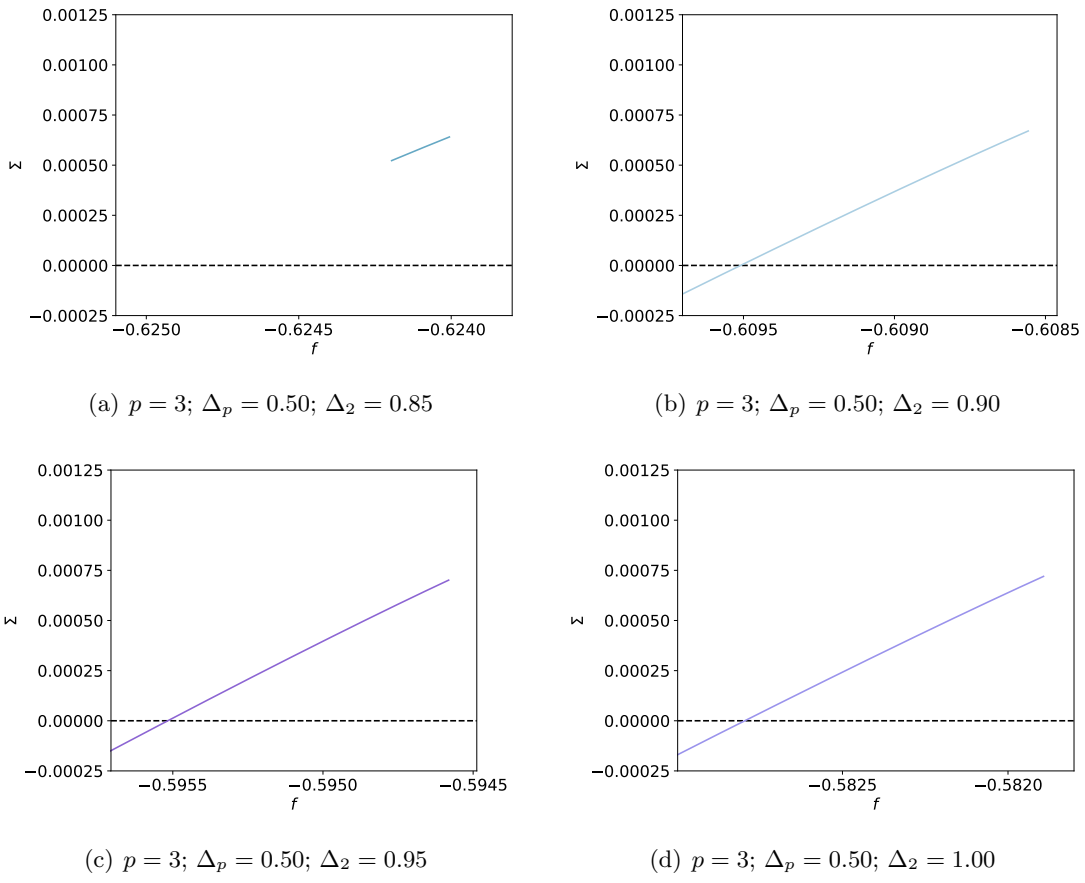


Figure 21: The stable part of the 1RSB complexity as a function of the free energy for $p = 3$ and $\Delta_p = 0.5$.

equilibrium. When the dynamics is run in the glass phase, metastable states may forbid equilibration. In this case time translational invariance is never reached at long times, it is supposed to be reached only on exponential timescales in the system size, and the dynamics displays aging violating at the same time the FDT relation. The analysis of the asymptotic aging dynamics has been cracked by Cugliandolo and Kurchan in [27, 47] (see also [68] for a pedagogical review) in the simplest spin glass model (see also [75] for a much more complex situation) where no signal is present. The outcome of this work is that when the dynamics started from a random initial conditions is run in the glass phase, it drives the system to surf on the *threshold* states. In the model analyzed in [27] these states correspond to the 1RSB marginally stable glassy states that maximize the complexity. In this section we analyze the Cugliandolo-Kurchan scenario by contrasting the numerical solution of the dynamical equations with the replica analysis of the complexity. According to [27], the long time Langevin dynamics, but still for times that are not exponentially large in the system size N , can be characterized by two time regimes. For short times differences $t - t' \sim \mathcal{O}(1)$ and $t' \rightarrow \infty$, the system obeys the FDT theorem and TTI; this regime can be understood as a first fast local equilibration in the nearest metastable state available. On a longer timescale $t - t' \rightarrow \infty$ and $t/t' < \infty$, the dynamics surfs on threshold states and FDT and TTI are both violated. In this time window, both the response and correlation functions become functions of $\lambda = h(t)/h(t')$ being $h(t)$ an arbitrary reparametrization of the time variable. The function $h(t)$ must be a monotonously increasing function. The asymptotic reparametrization invariance is a key property of the dynamical equations [27]. By defining $\mathcal{C}(\lambda) = C(t, t')$ and $\mathcal{R}(\lambda) = tR(t, t')$ the Cugliandolo-Kurchan solution implies that in this aging regime the FDT relation can be generalized to

$$\mathcal{R}(\lambda) = x \mathcal{C}'(\lambda) \quad (121)$$

with x an *effective* FDT ratio that controls how much the FDT is violated. In the scenario of [27], the value of x coincides with the 1RSB Parisi parameter that corresponds to threshold states computed within the replica approach. In order to test this picture we follow Cugliandolo and Kurchan [76] and we plot the integrated response $\mathcal{F}(t, t') = - \int_{t'}^t R(t, t'') dt''$ as a function of $C(t, t')$ in a parametric way. This is done in Fig. 22.

If FDT holds at all timescales, one should see a straight line with slope -1 . Instead what we see in the Langevin hard phase is that for large values of t' the curves approach asymptotically for $t' \gg 1$ two straight lines. For high values of \mathcal{C} , meaning for short time differences $t - t' \sim \mathcal{O}(1)$, the slope of the straight line is -1 which means that $\mathcal{F} = 1 - \mathcal{C}$ as implied by the short time FDT relation. On longer timescales FDT is violated, confirming the glassiness of the Langevin hard phase. By doing a linear fit we can use the data plotted in Fig. 22 to estimate the FDT ratio x appearing in Eq. (121). This can be compared with the Parisi parameter x for which we have marginally stable 1RSB states. We find an overall very good agreement (data coming from the fit is reported in the caption of Fig. 22). The small discrepancy between the two values of x can be either due to the numerical accuracy in solving the dynamical equations as well as the possibility that the 1RSB threshold is not exactly the one that characterizes the long time dynamics. Further investigations are needed to clarify this point. Finally, according to [27] the value of \mathcal{C} at which the two straight line cross should coincide with the value of q_M computed for the threshold states within the 1RSB solution. Again we find a very good agreement.

F Free-energy Hessian, BBP transition and Langevin threshold

In the following we present the derivation and the analysis of the Langevin threshold based on the study of the free energy Hessian. The starting point of the analysis is the so-called TAP free energy, i.e. the free energy as a function of the local magnetizations. The TAP free-energy was introduced in the early days of spin-glass theory [77, 43] and is now receiving a lot of attention in the mathematical community, see e.g. [78]. A straightforward generalization of the results of [79] allows one to obtain the TAP free energy for the model considered in this work, i.e. for the Hamiltonian (4):

$$F(\{m_i\}) = -\frac{\sqrt{(p-1)!}}{\Delta_p N^{(p-1)/2}} \sum_{i_1 < \dots < i_p} T_{i_1 \dots i_p} m_{i_1} \dots m_{i_p} - \frac{1}{\Delta_2 \sqrt{N}} \sum_{i < j} Y_{ij} m_i m_j + f(q)N.$$

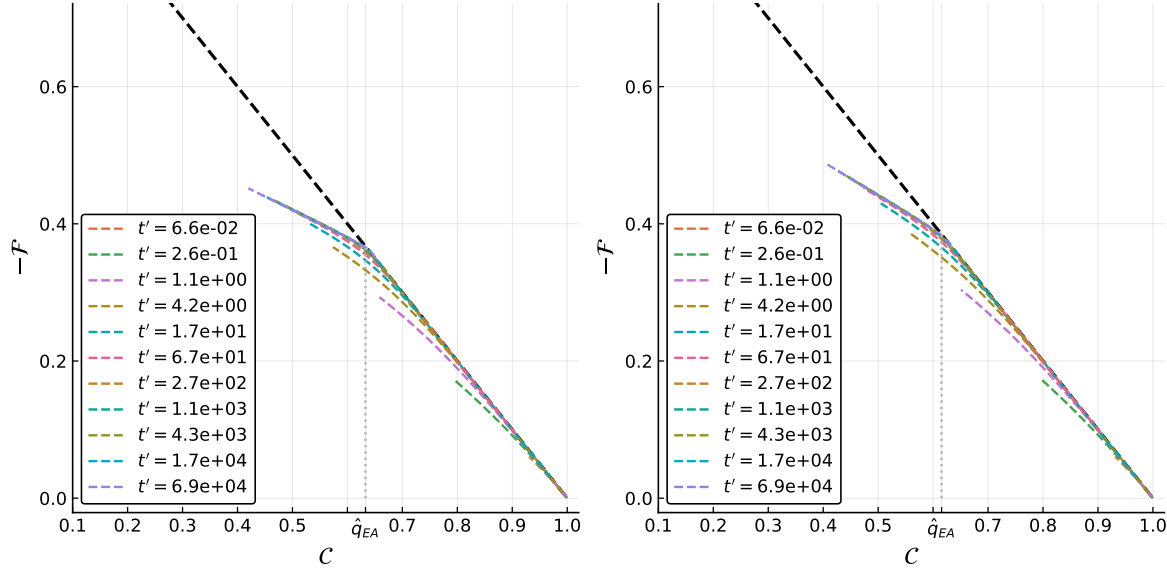


Figure 22: Left panel: parametric plot of integrate response function with respect to correlation function for $p = 3$, $\Delta_2 = 0.8$ and $\Delta_p = 0.2$. The different lines represent different waiting time, t' . The black dashed line correspond to the FDT prediction $x = 1$. The vertical dotted line is the point where we observe a kink, which we denote by $C = \hat{q}_{EA}$ and should be equal to the saddle point value of q_M as extracted from the 1RSB threshold states in the replica computation [27]: $\hat{q}_{EA} = 0.633$ and $q_M = 0.638$. For C smaller than q_{EA} the FDT is violated and is replaced by a generalized version as in Eq. (121). We can obtain the value of the FDT ratio from a fit of the slope of the asymptotic curves for $C < \hat{q}_{EA}$. We obtain $\hat{x} = 0.397$ which should be compared with the Parisi parameter that corresponds to 1RSB marginally stable states obtained from the replica computation that is $x = 0.408$. Right panel: parametric plot of the integrated response as a function of the correlation for $p = 3$ and $\Delta_2 = 1.4$ and $\Delta_p = 0.2$. In this case the value of the FDT ratio extracted from fitting the data is $\hat{x} = 0.397$ to be compared with the value of the Parisi parameter for the 1RSB threshold states that is $x = 0.408$. At the same time data gives $\hat{q}_{EA} = 0.633$ while the replica computation gives $q_M = 0.638$.

where we have set the temperature to one, $q = \sum_i m_i^2/N$ and $f(q)$ reads:

$$f(q) = -\frac{1}{2} \log(1 - q) - \frac{1}{2p\Delta_p} \left[1 + (p-1)q^p - pq^{p-1} \right] - \frac{1}{4\Delta_2} \left[1 + q^2 - 2q \right].$$

The so-called TAP states are local minima of $F(\{m_i\})$. We are interested in the free energy Hessian evaluated at the TAP states having zero overlap with the signal:

$$\frac{\partial^2 F}{\partial m_i \partial m_j} = G_{ij} + \delta_{ij} f'(q) - \frac{1}{\Delta_2} \frac{x_i^* x_j^*}{N} + f''(q) \frac{m_i m_j}{N}, \quad (122)$$

where the matrix G_{ij} is defined as

$$G_{ij} = -\frac{1}{\Delta_2 \sqrt{N}} \xi_{ij} - \frac{\sqrt{(p-1)!}}{\Delta_p N^{(p-1)/2} (p-2)!} \sum_{i_1, \dots, i_{p-2}} \xi_{iji_1 \dots i_{p-2}} m_{i_1} \dots m_{i_{p-2}}.$$

As shown originally in the spin-glass literature [49], and recently put on a firmer basis by the Kac-Rice method [32, 21], the matrix G_{ij} is statistically equivalent to a random matrix belonging to the Gaussian Orthogonal Ensemble (GOE). In our case, the corresponding GOE matrix has elements which are i.i.d. Gaussian random variables with mean zero and variance σ_F^2/N , where

$$\sigma_F^2(q) = \frac{(p-1)q^{p-2}}{\Delta_p} + \frac{1}{\Delta_2}.$$

Neglecting for the moment the last two terms in eq. (122), one finds that the free-energy Hessian is the sum of a GOE matrix and the identity multiplied by $f'(q)$. The corresponding density of eigenvalues is therefore the Wigner semicircle with support $[-2\sigma_F(q) + f'(q), 2\sigma_F(q) + f'(q)]$. This result is valid for any TAP state. The threshold states, which are the ones trapping the Langevin dynamics, are characterized by a vanishing fraction of zero modes, i.e. the left edge of the support of the Wigner semi-circle is zero. Their overlap is therefore fixed by the equation:

$$2\sigma_F(q_{\text{th}}) = f'(q_{\text{th}}) \quad \rightarrow \quad \frac{1}{1 - q_{\text{th}}} = \sqrt{\frac{(p-1)q_{\text{th}}^{p-2}}{\Delta_p} + \frac{1}{\Delta_2}}. \quad (123)$$

Let's consider now the role of the last two terms in eq. (122). Both are rank-one perturbations and hence can lead to a BBP transition [15], i.e. an eigenvalue that pops out of the Wigner semi-circle with an eigenvector having a finite overlap in the direction of the perturbation. It can be easily checked that $f''(q_{\text{th}}) \geq 0$; therefore the last term cannot lead to any negative eigenvalue and does not play any role in determining the stability of the threshold states. It is the other term which is responsible for the instability in the direction of the signal. In fact, it is the contribution due to the spike; it becomes larger when the signal to noise ratio, $1/\Delta_2$, increases.

The condition for the BBP transition for a GOE matrix having elements with variance σ_F^2/N and which is perturbed by a rank one perturbation of strength $1/\Delta_2$ is $\frac{1}{\Delta_2} = \sigma_F$. This is the equation for the Langevin threshold:

$$\frac{1}{\Delta_2} = \sqrt{\frac{(p-1)q_{\text{th}}^{p-2}}{\Delta_p} + \frac{1}{\Delta_2}},$$

Together with (123), this leads to the equation (15) presented in the main text and implies $q_{\text{th}} = 1 - \Delta_2^*$ at the Langevin threshold.